A MULTIMODAL LENS INTO VASCULAR RECOVERY IN A PRECLINICAL MODEL OF PERIPHERAL ARTERIAL DISEASE

BY

JAMILA HEDHLI

DISSERTATION

Submitted in partial fulfillment of the requirements
for the degree of Doctor of Philosophy in Bioengineering
in the Graduate College of the
University of Illinois at Urbana-Champaign, 2018

Urbana, Illinois

Doctoral Committee:

Assistant Professor Wawrzyniec Lawrence Dobrucki, Chair
Professor Michael F. Insana,
Associate Professor Kris Kilian
Professor Marni Boppart

Abstract

In the week of February 2nd (21 days into gestation) my parents Ali, and Aicha heard my first heart beat. This shouldn't be a surprise as the heart is the first organ to form and function during the developmental stages of the fetus. In the embryo, newly formed blood vessels provide the growing organs with the vital oxygen and nutrients required for them to flourish. During adulthood, angiogenesis—the process by which new blood vessels form—remains largely quiescent until the delicate balance between pro- and anti-angiogenic factors is disrupted, either through injury or disease.

Cardiovascular complications are among the leading causes of morbidity and mortality in diabetic patients, and account for over 80% of diabetes-associated deaths. One of the most serious is peripheral arterial disease (PAD), which is defined as a narowing of the peripheral vasculature. In this thesis, I will employ a range of imaging modalities to study PAD, investigating methods that may one day enable earlier detection of the disease, and exploring the therapeutic potential of stem cells to treat vascular complications associated with diabetes.

This document is divided into four main chapters. The first chapter describes the biological characterization of two different imaging probes targeted, respectively, at hypoxia and $\alpha_V\beta_3$ activity, as well as a new power Doppler ultrasound imaging technique capable of detecting small spatiotemporal changes in blood perfusion within muscle. The second chapters applies the ^{64}Cu-NOTA-PEG$_4$-cRGD$_2$ peptide targeted at $\alpha_V\beta_3$, to establish an optimal preclinical model of PAD. The third chapter builds on the first and second, by developing a multimodal approach for vascular imaging that enables simultaneous evaluation

of molecular and physiological changes during angiogenesis. Finally, the fourth chapter turns its attention toward the mitigation of diabetes-associated PAD. In it, we show that a targeted stem cell-based therapy can exert far reaching effects on the ischemic tissue microenvironment, and may provide clinical improvement for PAD patients in the future.

This thesis is warmly dedicated to Dr. John Andrew Cole, my parents Ali and Aicha, siblings Dr. Nadia, Sana, Amjed, Noura, and my UIUC family (Dr. Wawrzyniec Lawrence Dobrucki, and Dr. Iwona Dobrucka).

Acknowledgements

After my preliminary exam, I remember being told that graduate school will break you down and build you back up. I am a firm believer that no one achieves success without the help of others, and my rebuilding has been with the support of a number of incredible mentours and peers. I am deeply indebted to my advisor Dr. Wawrzyniec Lawrence Dobrucki, my dissertation committee, Dr. Michael Insana, Dr. Marni Boppart, Dr. Kris Kilian, our collaborators, Dr. Jeff Chan, Dr. Andrzej Czerwinski, Dr. Rohit Bhargava, and to my friends and colleagues at UIUC, especially Dr. Heather Hunstman, Dr. Junmin Lee, Dr. Kim Minwoo, Dr. Li Yanfen, Dr. Agata Polska, Christian Konopka and of course, to Dr. John Andrew Cole. I truly believe everything I have accomplished as a graduate student would not have been possible without their help, support, guidance, and most importantly, faith in me. Thank you all for teaching me the true meaning of collaboration. I also would like to thank a number of funding agencies that have supported me during my journey, including the Beckman predoctoral fellowship, and the National Institute of Biomedical Imaging and Bioengineering of the NIH.

Table of Contents

List of Tables

List of Figures

Chapter 1

Introduction

I joined the Dobrucki lab in the Fall of 2013, and over the course of the following five years I have co-authored some seventeen articles, of which seven are published [1–7], four are in revisions, and six are still in preparation. The research spans multiple areas microbiology, cancer biology, chemistry, biochemistry, molecular biology, and bioengineering. I have had the opportunity to collaborate with many talented scientists, and have learned so much from them. My work has earned me a number of accolades and recognitions, including my selection as an Illinois Innovation Prize Finalist, and a Jay D. Coffman Early Career Investigator Award Finalist (AHA), as well as several awards including a T32 NIH Tissue Microenvironment Training Program Fellowship, a Summer Research Trainee Program - Massachusetts General Hospital fellowship, a PVD Travel Award (AHA), a Britta L. and Charles J. Wolfe Award for Diabetes Research, a Beckman Institute Graduate Fellowship, and a Beckman-Brown Post-Doctoral Fellowship. But as I reflect back on my time as a graduate student, there are only a few works that stand out to me as milestones in my growth as a scientist. This document includes four of them, each in their entirety, as Chapters 2–5.

1.1 Problem statement and objectives

Diabetes represents a major world-wide health concern. Hung *et al.* projects that between 2009 and 2034 the number of people with diabetes will increase from 23.7 million to 44.1 million, resulting in a significant strain to the global health care system with a projected increase in relative cost of almost 4-fold [8]. The Centers for Disease Control (CDC) in a 2014 diabetes report card estimated that about 1.7 million new cases of diabetes are diagnosed

each year, and predicted a sharp rise in the next couple of years, during which an estimated 1 in 3 adults will be diagnosed [9].

Cardiovascular complications are among the leading causes of morbidity and mortality in diabetic patients, and account for over 80% of diabetes-associated deaths. One of the most serious is peripheral arterial disease (PAD), which involves the gradual narrowing of the arteries to the extremities. Very often patients with PAD can be asymptomatic, making the condition difficult to recognize and treat. As a result, the blood flow can become progressively impaired, and ischemia can occur. When ineffectively treated, peripheral ischemia can result in debilitating injury; in the United States alone roughly 50,000 cases each year lead to amputation [8]. The deleterious nature of PAD coupled with its often underdiagnosed and undertreated status necessitates a reexamination of the existing methodologies used to diagnose and manage the disease.

Understanding both the progression of PAD, and the bodily response to the disease, requires the simultaneous evaluation of several interrelated molecular, anatomical, and functional parameters, all within a living subject. The overarching goal of this disseration is to provide a better understanding of the progression of PAD, and to develop new methods to help detect it earlier and treat it more effectively. My efforts will bring to bear a number of leading-edge imaging modalities, and will ultimately lead to an exciting new stem cell-based therapy with the potential for clinical translation.

1.2 Peripheral Arterial Disease (PAD)

1.2.1 Historical perspective

It is difficult to pinpoint exactly when cardiovascular diseases were first discovered. Somewhere between 1504 and 1506 Leonardo da Vinci met an elderly man who describing experiencing weakness with no bodily ailment, and who died shortly thereafter. Without any medical training, Leonard performed an autopsy on the man in an attempt to understand the reason

of his "peaceful death" [10]. What resulted was the first drawings and description of what would come to be known as coronary artery disease. This achievement however, is often overlooked in the history of medicine due to Leonardo's notoriously fragmented notes and lack of publications. It would take almost 100 years for the circulatory system to begin to be properly described with a 72 page book written by William Harvey in 1628 [11]. Harvey, through experimentation, correctly distinguished between arteries and veins, and provided the first evidence of blood circulation.

This achievement would be followed by many milestones. In 1893 Holland Willem Einthoven constructed the first electrocardiograph and recorded one of the first ECGs ever via a 1.5 km telephone cable connecting the hospital to his laboratory [12]. He was awarded the noble prize in physiology and medicine in 1924. Many other discoveries followed; the X-ray by Wilhem Konrad Roentgen in 1895 [13], the first defibrillation of a human heart during cardiac surgery by Claude Beck (1947) [14], and the first battery-powered external pacemaker in 1957 [15].

PAD, described as the narrowing and eventual blockage of arteries that supply blood to the lower extremities, has a long history and remains highly prevalent, with an estimated 200 million people afflicted worldwide despite a steady decline in overall morbidity and mortality from cardiovascular diseases.

Histological evaluation of the Egyptian mummies gastrocnemius and soleus muscles indicate changes indistinguishable from the effects of PAD [16]. The first manifestation of the disease to be recognized in modern times was gangrene (tissue death caused by lack of blood supply) in 1771 by the french physician Quesnay [16]. He further associated the obstruction of distal arteries to be the cause of distal gangrene. Before World War II, the syndrome of intermittent claudication in the periphery was well characterized but the mechanism underlying the disease remained poorly understood.

One of the earliest methods to diagnose PAD was tonoscillography, which detects the amplitudes of the pressure waves in the arteries at different levels in the leg. Developed

in 1940, the instrument allowed Ejrup Börje, through experimentation, to confirm that arterial pulsation diminished after exercise in patients with PAD [17]. A more invasive technique emerged from the work of Kety Seymour in 1948, who measured blood flow in the gastrocnemius by way of the clearance rates of injected radioactive isotopes [18].

Various forms of plethysmography were developed—gravimetric, capacitance, and strain gauge—and while they provide quantitative measures, they did not lead to any actionable information regarding the occlusion site. For the Last 90 years the method of choice for the anatomical determination of PAD has been arteriography. In 1929 Dos Santos performed the first translumbar aortogram by the direct injection of contrast medium percutaneously into the aorta. This marks a major milestone in the imaging of PAD [19]. Indeed, arteriography remains an important diagnostic tool and has even come to be used during reconstructive surgery.

The second major milestone in PAD imaging involved Doppler Ultrasound. In 1959 Shigeo Satomura was the first to describe the application of Doppler ultrasound to investigate PAD [20]. Even today, the pocket Doppler probe remains one of the most widely used pieces of equipment among vascular surgeons. Duplex scanning, a more recent innovation, combines real time ultrasonic imaging with Doppler flow measurements that have undergone sound spectrum analysis for visual display.

1.2.2 Molecular physiology of PAD

Angiogenesis, the formation of new blood vessels from pre-existing microvasculature, represents an important and complex biological process. Blood vessels are the first organ to form in the embryo, and constitute the largest network in our body [21–23]. When the delicate balance between pro- and anti-angiogenic factors is disrupted, numerous physiological and pathological processes, including PAD and cancer, can be affected [24,25]. The most influential stimulator of angiogenesis is hypoxia-inducible factor-1 (HIF-1), the expression of which is normally enhanced under hypoxic conditions. HIF-1 in turn regulates the expression of

many key angiogenic factors, including vascular endothelial growth factor (VEGF), and platelet-derived growth factor (PDGF) [25]. VEGF binds its receptor VEGFR which, through a cascade of biochemical interactions, elicits cellular responses that include endothelial cell proliferation, migration, and survival. Activated endothelial cells upregulate transmembrane cell adhesion molecules such as the integrins that assist in cell-cell signaling. In particular, $\alpha_V\beta_3$ facilitates interactions between endothelial cells and the extracellular matrix (ECM), which ic critical during migration. Under normal circumstances, all of this biochemistry results in the formation and elongation of new vascular networks that increase blood flow to the hypoxic tissue. Unfortunately, a number of conditions are known to dysregulate these pathways, which can lead to chronic hypoxia, and ultimately debilitating injury or death. Among the most prevalent world-wide is diabetes mellitus (DM), which when poorly treated results in hyperglycemia that inhibits HIF-1 transcription [26], and in turn, the entire angiogenic response. This is particularly problematic in the extremities, which gives rise to a strong association between DM and PAD.

1.2.3 Current state-of-the-art methods to diagnose PAD

Current clinical options for the preoperative assessment of PAD patients include two main methodologies: the ankle-brachial pluse index (ABI); and contrast angiography. The measurement of ABI is widely used by surgeons in assessing the disease state, but is highly unreliable in individuals with long-standing diabetes who develop noncompressible arteries due to medial calcification [27]. Contrast angiography, the "gold standard", on the other hand, is an invasive imaging technique often employed during reconstructive surgery in PAD patients [28]. It carries the inherent risks of bleeding, infection, and vessel disruption, with rates of major complications ranging from 1.9 to 2.9% [29].

Recent advances in non-invasive angiography, including magnetic resonance angiography (MRA), can enable the diagnosis of the location and degree of stenosis in PAD patients. However, MRA tends to overestimate the degree of stenosis because of turbulence. Moreover,

it cannot be used to scan patients with pacemakers or defibrillators [30].

1.3 Research overview

The recent history of PAD research has been punctuated by milestones in visualizing the disease. This remains true even today. But slowly, researchers are starting to expand their focus to include the effects of vascular occlusion on the tissue microenvironment, and ways to modulate the web of chemical and cellular interactions that underlie vascular healing. The main focus of this thesis comes in two parts: first, I will study the ischemic microenvironment of PAD by integrating a range of non-invasive imaging modalities; and second, I will demonstrate the use of muscle-derived mesenchymal stem cells as a promising approach to speed vascular recovery following arterial occlusion Figure 4.1.

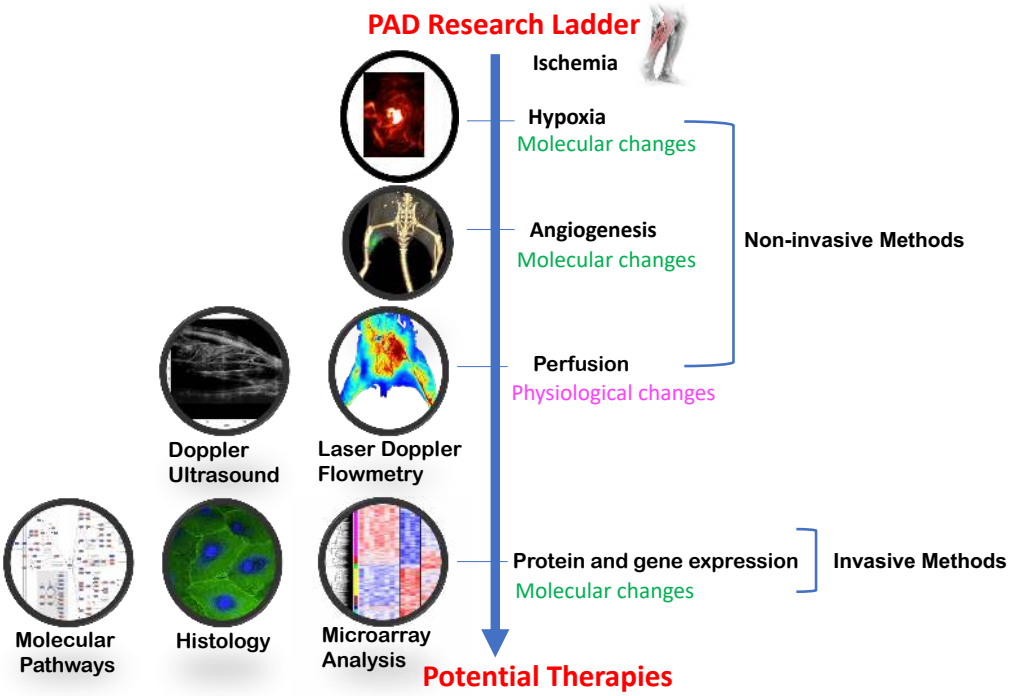

Figure 1.1: Schematic Diagram of the proposed research plan.

Chapter 2 focuses on the development of two novel probes designed to image key biomarkers associated with angiogenesis. It begins with Hypoxia Probe 1 (HyP-1), a hypoxia-responsive imaging agent designed for photoacoustic imaging, which we demonstrate its

applicability in a murine model of hindlimb ischemia [4]. We then move on to develop a Dimeric-cRGD probe targeted at $\alpha_V\beta_3$. This probe, radiolabeled for PET imaging, will be characterized across multiple scales—receptor, cell, and whole body—in order to describe its binding kinetics, specificity, and clearance route. $\alpha_V\beta_3$ is a key player in angiogenisis, and by targeting its activated form, we can image where and when the body in actively growing new blood vessels.

While targeted radio-labeled probes like ours are becoming increasingly important in diagnostics and prognostication, they come with some inherent drawbacks. First, the short lives of the isotopes commonly used necessitate that they be manufactured, delivered, and chelated to the probes shortly before administration. Second, both PET and SPECT devices are relatively expensive in and of themselves. These issues render nuclear imaging technologies less attractive as tools for prescreening large numbers of patients who may or may not suffer from a disease. In the third part of Chapter 2, we introduce a new Power Doppler ultrasound (US) technology that, without any exogenous contrast enhancement or specialized equipment, is sensitive enough to detect spatiotemporal changes in blood perfusion within muscle. Developed by the Insana lab, this new US methodology uses conventional instrumentation, but samples and filters echo signals in new ways. This can enable general practitioners, who are usually the first point of contact with a patient, to recognize and diagnose the disease early, and at a low cost, ultimately leading to more effective treatment and better patient outcomes [3].

Chapter 3, "Evaluation of a dimeric-cRGD peptide for targeted PET-CT imaging of peripheral angiogenesis in diabetic mice," [1] picks up where Chapter 2 leaves off. With our imaging technologies already in hand, this next chapter seeks to establish a suitable animal model of PAD. The major risk factors for PAD include smoking, diabetes, high blood pressure, and obesity [31]—factors whose effects can build up over years or decades in humans, and whose full impact can be difficult to reproduce in weeks-old laboratory mice. Focusing on diabetes, we developed protocols for inducing DM in mice via streptozotocin injection,

and then surgically ligating the right femoral arteries of the mice in order to model PAD. Subsequent imaging using our PET-CT probe showed a significant reduction in the $\alpha_V\beta_3$ activation in DM mice when compared to non-DM control mice. This was confirmed by immunofluorescence staining of excised ischemic tissues, which showed a three-fold reduction in CD31 (endothelium cell marker) and a four-fold reduction in the $\alpha_V\beta_3$ expression in DM *vs.* non-DM animals.

Much of the work described thusfar has focused on imaging a single observable in ischemic tissue (*e.g.* hypoxia, $\alpha_V\beta_3$ activation, or blood perfusion), but the biological processes involved in vascular recovery involve complex signalling cascades and the interplay of multiple different cell types within a shared microenvironment. **Chapter 4**, which reproduces "A Multimodal Lens into Vascular Recovery in a Preclinical Model of Peripheral Arterial Disease," expands our view by serially evaluating a number of different biochemical and physiological indicators of angiogenic process. Specifically, we employ an integrated multimodal approach to study PAD using: 1) SPECT imaging of probes targeted at HIF-1α and $\alpha_V\beta_3$—the former being one of the originators of the hypoxia-induced proangiogenic signalling cascade, and the later being one of its many downstream products; 2) high resolution Power Doppler US to directly detect tissue perfusion; 3) photoacoustic imaging (PA) designed to detect tissue oxygenation; and 4) laser speckle contrast imaging (LSCI) for label-free perfusion and blood oxygenation imaging in the shallow tissue. When viewed together, this multimodal imaging approach paints a holistic picture of the peripheral limb response to vascular occlusion at the anatomical, functional, and molecular levels. We observe that the effects of ligation are almost immediate, with perfusion and oxygenation levels dropping substantially just minutes after the operation. From there, we noticed that in the deep tissue, the angiogenic response can take approximately three days or more to be fully elicited, beginning with a rapid rise in HIF-1α expression followed by a slower rise in $\alpha_V\beta_3$ expression. The effects of angiogenesis, *viv-a-vis* blood perfusion, do not manifest until approximately a week after ligation. We also see that the surface tissue undergoes a very different mode of recovery than does the deep

tissue, beginning to reestablish normal blood perfusion within just two days, likely through arteriogenesis rather than angiogenesis. It is hoped that this type of multimodal imaging approach will help to better understand a number of complex biological systems, and aid in the development and evaluation of new therapies for human disease.

Chapter 5, the final chapter of this document, reproduces "Multimodal Assessment of Mesenchymal Stem Cell Therapy for Diabetic Vascular Complications" [2]. Building on what we have learned about the different microenvironmental cues that support angiogenesis, this project brings to bear both imaging and gene expression profiling technologies in order to investigate the use of mesenchymal stem cells as a therapy for diabetic patients with PAD. I enjoyed this project immensely, and remain extremely proud of it. Current clinical management of PAD focuses largely on surgical interventions and lifestyle changes including exercise. Unfortunately, over 30% patients are not considered suitable for surgery [32], and exercise can be difficult and painful for diabetic patients who are already experiencing noticeable symptoms of lower limb ischemia. A new generation of therapies intended to promote angiogenesis and arteriogenesis is sorely needed. Here, we consider the use of muscle-derived mesenchymal stem cells (mMSCs) injected into the ischemic tissue of our diabetic mice as a method of altering the microenviroment and rendering it more conducive for angiogenesis. We employed several minimally invasive *in vivo* imaging and diagnostic approaches (nuclear, laser Doppler perfusion, muscle function and microarray transcriptomics) in order to construct an accurate picture of the effects of our transplanted mMSCs, as well as the response of our mice to treatment, and their long-term prognosis. We find that mMSCs lead to greatly enhanced neovascularization roughly one week after treatment. We also find that at the two-week timepoint, the transcriptional profile of our stem-cell treated mice resembles that of healthy mice while a control group treated with saline continue to express anti-angiogenic factors, indicating a relative lack of healing. The translational nature and timeliness of this work is significant, and our results have potentially important clinical implications for the evaluation and management of diabetic patients with PAD.

Chapter 2

Development of the methodology for non-invasive multimodal assessment of PAD †

2.1 Hypoxia detection using a Bioreducible N-oxide-based Probe

2.1.1 Introduction

Hypoxia refers to a physiological state in which tissue oxy-gen supply is restricted. Diminished oxygen levels can be in-duced by a variety of diseased states; including coronary artery disease peripheral arterial disease and gastrointestinal inflammatory conditions [33, 34]. With respect to cancer, an estimated 50-60% of solid tumors contain hypoxic regions, which is noteworthy considering that hypoxic tumors are commonly associated with high metastatic potential, aggressive phenotypes and treatment resistance [35]. Detection of hypoxia in vivo is therefore an area of significant research interest because of the potential to predict treatment responses and provide patient-specific therapies [36, 37]. The current gold standard of hypoxia detection involves the use of oxygen-sensitive electrodes, which must be inserted into the tissue of interest. Although this technique provides a direct measurement of oxygen partial pressure (pO2) it is highly invasive and only applicable when tissue is accessible, such as in superficial tumors of the head and neck [38]. As such, significant effort has been put forth to develop alternative methods for non-invasive hypoxia detection. For instance, optical imaging with

†Work includes previously published material incorporating contributions from Hedhli Jamila, Czerwinski Andrzej, MinWoo Kim, Hailey J. Knox and others [3–5].

hypoxia-responsive fluorescent probes has enabled visualization of hypoxia in living cells with excellent subcellular resolution. However, due to high scattering and limited penetra-tion of light in biological tissue, fluorescent probes afford poor resolution beyond an imaging depth of 1 mm in animal models [39]. In contrast, positron emission tomography (PET) is not constrained by depth, and has been utilized for hypoxia detection *in vivo* using various fluorine-18 ^{18}F-labeled radio-tracers [40]. However, imaging hypoxia using this modality also faces major obstacles including high background due to non-specific uptake of radiotracers in tissue and limited spatial resolution, hampering its ability to accurately discern specific hypoxic regions. Moreover, owing to the relatively short half-life of ^{18}F (110 mins), imaging sessions must be performed immediately following probe synthesis. Photoacoustic (PA) imaging is an emerging imaging modality that enables ultrasonic detection of absorbed light in deep tissue. PA imaging is based on the phenomenon known as the PA effect, first described by Bell in 1880 [41, 42]. Excitation of chromophores in tissue with near-infrared (NIR) light results in vibrational relaxation, which stimulates a local temperature increase. The heat produced causes thermoelastic expansion of the surrounding tissue, stimulating a change in pressure. Because imaging is performed using a pulsed laser sequence, expansion and contraction cycles are induced, creating repeated pressure fluctuations and thereby propagating ultrasound waves through the tissue. These ultrasound waves are detected by transducers, and the signal can be reconstructed to produce a 3D image of the area of interest. The limited scattering of sound in tissue enables PA imaging to produce high resolution images at depths in the centimeter range [41]. Moreover, the non-ionizing radiation used for PA imaging is a potentially safer alternative to high-energy radiation used for other imaging modalities [43]. Herein, I present the development of Hypoxia Probe 1 (HyP-1), a hypoxia-responsive acoustogenic probe designed for PA imaging. HyP-1 utilizes a novel bioreducibile N-oxide trigger that is selectively reduced by CYP450 enzymes in the absence of oxygen. This design was inspired by AQ4N, a hypoxia-responsive cancer prodrug containing two N-oxide moieties that mask its cytotoxic effects prior to reduction in hypoxic tissue. Of

note, N-oxides have also been employed for fluorescence sensing of Fe(II) and biorthogonal conjugation reactions; however,This work represents the first application of this functionality for selective hypoxia detection [44]. The PA response of HyP-1 is based on the ability of the N-oxide to modulate its optical properties. Specifically, conversion of the N-oxide to the corresponding aniline (red-HyP-1) elicits a dramatic bathochromic shift in the absorbance from 670 to 760 nm (Figure 2.1). Because HyP-1 does not absorb at this wavelength, the PA signal produced upon excitation at 760 nm corresponds exclusively to red-HyP-1. Therefore, hypoxia detection is made possible by determining the signal enhancement observed at this wavelength. Additionally, because HyP-1 and red-HyP-1 are highly fluorescent, HyP-1 can be used for ratiometric quantification. To demonstrate the imaging capabilities of HyP-1, I first evaluated its hypoxia-mediated response and selectivity in vitro. I then moved to verify that HyP-1 shows a selective response in cancer cells cultured under hypoxic conditions. Finally, I demonstrated the rapid response of HyP-1 in a hindlimb ischemia model of peripheral arterial disease (PAD).

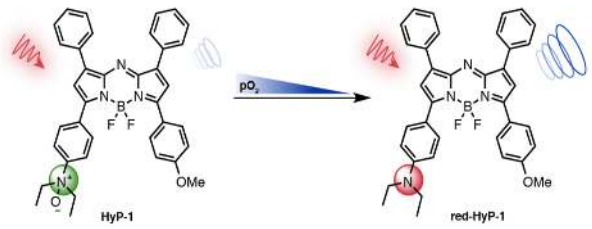

Figure 2.1: Chemical structure of HyP-1 and red-HyP-1. HyP-1 undergoes hypoxia-selective reduction by CYP450 enzymes

2.1.2 Methods

A detailed description of the chemical and the *in vitro* characterization of HyP-1 is highlighted in [4]. But briefly, HyP-1 features an N-oxide-based trigger that can undergo facile bioreduction in the absence of oxygen. This design was inspired by AQ4N, a hypoxia-responsive cancer prodrug containing two N- oxide moieties that mask its cytotoxic effects prior to reduction

in hypoxic tissue. The responsiveness of HyP-1 to hypoxia was first evaluated in vitro via fluorescence by incubating HyP-1 with CYP450-rich rat liver microsomes under atmospheric (normoxic) and oxygen-deprived (hypoxic) conditions. After establishing excellent selectivity and responsiveness to hypoxic conditions in vitro, I sought to evaluate the performance of HyP-1 in living cells before moving to *in vivo* studies. 4T1 murine mammary carcinoma cells were treated with a 5 μM solution of HyP-1 and incubated at 37 °C either in a standard atmosphere containing 20% oxygen (normoxic conditions), or in an airtight chamber containing <0.1% oxygen (hypoxic conditions). Imaging was performed at 2, 4, and 6 h using an epi-fluorescence microscope equipped with Cy5 and Cy7 filter sets to visualize HyP-1 and red-HyP-1, respectively.

Murine ischemia model

All *in vivo* imaging experiments were performed with the approval of the Institutional Animal Care and Use Committee of the University of Illinois at Urbana-Champaign, following the principles outlined by the American Physiological Society on research animal use. Female mice (5–6 weeks old) were acquired from The Jackson Laboratory. Mice were anesthetized with isoflurane, and unilateral hindlimb ischemia was surgically induced by femoral artery ligation following previously published approaches. Animals that underwent unsuccessful surgery as determined by laser Doppler perfusion imaging were excluded from analysis.

Fluorescence imaging In vivo Images were obtained using epi-fluorescence with excitation filters of 675 and 745 and corresponding emission filters of 720 and 800, respectively. Data was processed using Living Image software (Version 4.1). ROIs of equal area were drawn around signals, and the total radiant efficiency in each ROI was determined. Ratiometric signal was calculated by determining the ratio of radiant efficiency corresponding to 800 and 720 nm emissions.

PA imaging In vivo. Prior to imaging, hair was removed from the lower body half by shaving and treating with a topical hair removal cream. Mice were positioned on their sides such that the area to be imaged was directly above the light source. Images were acquired using the Step and Shoot mode with 120 angles and 30 pulses per angle. Data were analyzed using OsiriX software. Thick slab processing was used to visualize accumulated signal over 12 mm. ROIs of equal area were drawn to include all visible signal in the image, and mean PA signal in each ROI was recorded. Change in PA signal was calculated by subtracting signal from images taken prior to injection from those at given time points.

2.1.3 Results and Discussion

In vivo imaging of hypoxia in a murine model of peripheral arterial disease

Due to the rapid oxygen depletion that results from PAD model, I envisioned it could be used to demonstrate the response of HyP-1 to hypoxic conditions *in vivo* independent of changes in gene and protein expression levels that can result from other models (i.e. cancer). In these studies, ischemia was induced in the right hindlimb of BALB/c mice via ligation of the femoral artery. To confirm that the ligation had successfully limited blood perfusion through the limb, laser Doppler perfusion imaging was performed immediately following the surgery, and a drastic decrease in blood flow was observed in the right hindlimb (Figure 2.2).

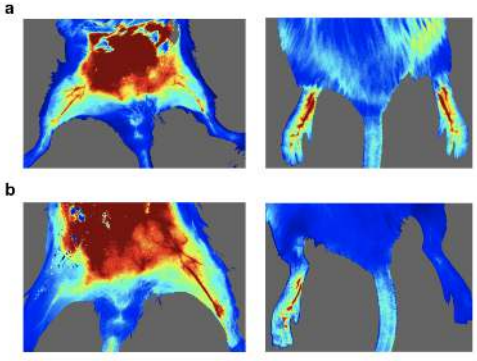

Figure 2.2: Laser Doppler perfusion images acquired (a) before and (b) 15 minutes after surgical ligation of the femoral artery in the right hindlimb

After a 1 hour recovery period, HyP-1 (50 μL, 50 μM) was administered via intramuscular injection into both hindlimbs of the mouse. To visualize the time-dependent response of HyP-1 in the ischemic and non-ischemic tissue, ratiometric fluorescence imaging was performed over the course of 1 hour immediately following injection. A rapid increase in the ratiometric fluorescence intensity corresponding to conversion of HyP-1 to red-HyP-1 was observed in the ischemic tissue. Overall, the average ratiometric signal increase was 1.7-fold greater in the ischemic tissue compared to the control, indicating oxygen-dependent inhibition of HyP-1 activation (Figure 2.3a,b).

Moreover, I confirmed that the activation of HyP-1 under ischemic conditions does not involve Fe(II) by co-administering HyP-1 with BIPY (5 mM) to chelate free Fe(II). The ratiometric fluorescence enhancement was statistically indistinguishable from that of when HyP-1 was administered alone Figure 2.4.

After observing the hypoxia-mediated response of HyP-1 in the hindlimb ischemia model, I turned my attention to detecting this response using PA imaging. As described above, ligation of the surgical ligation was employed to induce ischemia, and HyP-1 (50 μL, 50 μM) was administered via intramuscular injection. PA images were acquired 1h following injection, and a robust signal enhancement 3.1-fold greater on average than that of the control leg was observed in the ischemic tissue see (Figure 2.3b,d). These results demonstrate that HyP-1 can be applied to hypoxia detection in multiple disease models. In addition, the limited time frame between induction of ischemia and imaging suggests that HyP-1 does not rely significantly on upregulation of heme-based redox proteins, but rather can undergo rapid conversion to red-HyP-1 under hypoxic conditions at constitutive enzyme expression levels.

2.1.4 Conclusion

PAD is characterized by restricted arterial circulation to the limbs, most commonly the legs, resulting from plaque deposition and arterial hardening. The murine hindlimb ischemia model is widely accepted for the study of PAD and has been used in the evaluation of

potential treatment options. In the following study, I have demonstrated that HyP-1 exhibits a rapid turn-on response in murine hindlimb ischemia just 1h following surgical ligation of the femoral artery. These results show the excellent sensitivity of HyP-1 to oxygen-deficient conditions resulting from ischemia. Thus, detection of hypoxia can guide treatment planning and serve as a predictor of PAD patient prognosis. Prior to this work, hypoxia detection using optical methods has relied extensively on fluorogenic probes that provide minimal resolution and depth penetration. Through the development of HyP-1, I have established criteria for employing optical-based probe designs for translation into powerful PA imaging agents. Probes, such as HyP-1, that undergo reaction-based activation to elicit a PA turn-on response can provide a target-specific readout in deep tissue, a direction that was previously exploited only for cell-based fluorescence imaging. While impressive, the advances in PA techniques and instrumentation have been constrained by a shortage of PA probes that can demonstrate target-specific detection. As such, the importance of HyP-1 extends beyond hypoxia detection; rather, I anticipate this work will stimulate further investigations in this rapidly growing arena.

2.2 Perfusion imaging using Ultrasonic Power Doppler

2.2.1 Introduction

The goal of ultrasonic Power Doppler (PD) imaging is to display the magnitude of blood perfusion in tissue at each point in a scan plane. PD methods are sensitive to red-blood-cell (RBC) movements, making them useful for assessing ischemia and flow in tortuous vessels. Nonetheless, quantifying slow and weakly-scattering intrinsic perfusion signals remains a formidable challenge. The principal challenge is to increase the signal-to-noise+clutter ratio (SNCR), which is addressed by either suppressing noise and clutter components [45–47] or

augmenting the blood-flow component with contrast agents [48–50]. The work focuses on non-contrast-enhanced approaches to improving PD imaging.

I provide an initial demonstration of a simple echo-acquisition and data filtering strategy that appears to substantially improve SNCR and Doppler-frequency resolution. With some tuning of the filters, I clearly see regions of slower perfusion that are not visible using established PD techniques. The acquired data at each spatial location are arranged to have two temporal dimensions: slow-time sampled on the order of kHz and frame time sampled on the order of Hz. Temporal sampling is adjusted to increase the density of independent samples in the low-frequency Doppler spectrum where the weak perfusion signal is strongest. I then increase the dimension of the clutter filter to fully exploit the expanded dimensionality of the data, and employ high-frequency pulses to further increase SNCR.

The recorded data array initially has two spatial dimensions (axial and lateral) and two temporal dimensions (slow-time and frame-time). These data are reordered to combine the two spatial axes into one, resulting in a 3-D data array with one spatial and two temporal axes. I describe the information contained within this 3-D data array and a 3-D clutter filter that separates blood components from clutter and noise.

Traditional filters have been employed in the slow-time domain to reduce power at low temporal frequencies where clutter dominates [51]. The resulting perfusion estimates are often averaged over a few spatial locations and/or multiple frames to reduce variance in the estimates. However, under conditions of slow flow, a significant portion of the perfusion signal may fall into the attenuated frequency channels of the clutter filter. This issue is also present for more general eigenfilters that operate on slow-time echo signals [52, 53].

An alternative to 1-D slow-time filters has been to expand the filter dimension to use information from both space and time to isolate the blood signal [45]. Two-dimensional filters are derived from the echo data using singular-value decomposition (SVD). They exploit the spatial coherence of clutter echoes as distinct from the more incoherent flow patterns of perfusion when separating clutter and blood signals. Today, estimation of SVD-filtered

data often takes place along the spatial and slow-time axes. If frame-time data are recorded, they are averaged to stabilize the SVD filter. Higher sampling rates along the slow-time axis can be achieved with plane-wave imaging techniques [47] that facilitate noise averaging when forming SVD filters from the data.

We propose here to extend SVD filters to 3-D data arrays described above using a higher-order SVD (HOSVD) technique [54, 55]. I will show data that suggests this filter facilitates isolation of echo power from slowly-moving and spatially disorganized RBC movement. HOSVD filter construction yields one set of basis vectors for each of the three data dimensions within a region of interest. Retaining all three data dimensions enables the adaptive HOSVD filter to effectively separately signal components. I hypothesize that by analyzing data along the frame-time axis, I can enhance the sensitivity of PD imaging to blood perfusion echo signals. The challenge for users is to find a subspace in the HOSVD core array that isolates perfusing blood signals. Projecting the recorded echo data onto that subspace before computing the signal power at each pixel dramatically increases PD sensitivity to perfusion. The process of filter formation includes signal averaging that improves filter stability. However, I must take care to select spatial regions that include only wide-sense stationary echo data.

To test the feasibility of the approach, these measurement methods are applied to muscle-perfusion imaging of healthy and ischemic mouse hindlimbs. Perfusion in this model of surgically-induced ischemia generates spatial patterns of perfusion/ischemia [56] that I track to observe and compare with alternative approaches.

2.2.2 Methods

Implementation

A detailed description of the PD methodology is presented in [3]. Briefly, three eigenanalyses are performed on $\boldsymbol{\mathcal{X}}$ via Eq. (2.1).

$$\mathbf{R}_N = [\boldsymbol{\mathcal{X}}]_1[\boldsymbol{\mathcal{X}}]_1^\dagger = \mathbf{U}\boldsymbol{\Lambda}_N\mathbf{U}^\dagger \in \mathbb{C}^{N\times N}$$

$$\mathbf{R}_S = [\boldsymbol{\mathcal{X}}]_2[\boldsymbol{\mathcal{X}}]_2^\dagger = \mathbf{V}\boldsymbol{\Lambda}_S\mathbf{V}^\dagger \in \mathbb{C}^{S\times S} \tag{2.1}$$
$$\mathbf{R}_K = [\boldsymbol{\mathcal{X}}]_3[\boldsymbol{\mathcal{X}}]_3^\dagger = \mathbf{W}\boldsymbol{\Lambda}_K\mathbf{W}^\dagger \in \mathbb{C}^{K\times K} \ .$$

From the three sets of eigenvectors generated, the core tensor is formed via Eq. (2.2).

$$\boldsymbol{\mathcal{G}} = \boldsymbol{\mathcal{X}} \times_1 \mathbf{U}^\dagger \times_2 \mathbf{V}^\dagger \times_3 \mathbf{W}^\dagger \ . \tag{2.2}$$

Components of $\boldsymbol{\mathcal{G}}$ are orthogonal in that the dot product between planes in the array,

$$< \boldsymbol{\mathcal{G}}_{i_n=\alpha}, \boldsymbol{\mathcal{G}}_{i_n=\beta} >= 0, \quad \alpha \neq \beta, \forall n, \forall\alpha, \forall\beta \ , \tag{2.3}$$

We then select a region within the core tensor that contains information about perfusion and zero the other elements via Eq. (2.5). This process yields the perfusion subspace whose elements are squared and summed in Eq. (2.4) to estimate the signal power mapped into PD images.

$$\mathbf{p}_j[i_2] = \frac{1}{N\dot{K}} \sum_{i_1=1}^{N} \sum_{i_3=1}^{\dot{K}} |\tilde{\boldsymbol{\mathcal{B}}}_j[i_1, i_2, i_3]|^2 \ , \tag{2.4}$$

where $\mathbf{p}_j \in \mathbb{R}^{\dot{S}}$. In vivo experiments below show that the perfusion subspace is confined to a small region within $\boldsymbol{\mathcal{G}}$. Therefore I find it is fast and easy to exhaustively search for values of c_n and b_n in Eq. (2.5) that yield the "best" perfusion maps shown in the results below.

$$\begin{aligned} \hat{\boldsymbol{\mathcal{B}}} &= \sum_{i_1=c_1+1}^{c_1+b_1} \sum_{i_2=c_2+1}^{c_2+b_2} \sum_{i_3=c_3+1}^{c_3+b_3} g_{i_1,i_2,i_3}\mathbf{u}_{i_1} \times \mathbf{v}_{i_2} \times \mathbf{w}_{i_3} \\ &= \sum_{i_1=c_1+1}^{c_1+b_1} \sum_{i_2=c_2+1}^{c_2+b_2} \sum_{i_3=c_3+1}^{c_3+b_3} \boldsymbol{\mathcal{X}} \times_1 \mathbf{u}_{i_1}{\mathbf{u}_{i_1}}^\dagger \\ &\qquad \times_2 \mathbf{v}_{i_2}{\mathbf{v}_{i_2}}^\dagger \times_3 \mathbf{w}_{i_3}{\mathbf{w}_{i_3}}^\dagger \ . \end{aligned} \tag{2.5}$$

Echo data were recorded using a Vevo® 2100 system and a MS400 linear array (FUJIFILM VisualSonics Inc. Toronto, Ontario, Canada). The transducer transmits 2-cycle pulses with a

24 MHz center frequency. All processing was implemented in MATLAB 2013b on an Intel processor i5-4300U CPU, 2.50 GHz. The highest computational burden is filter construction, which was performed using a truncation technique [57] to minimize running time. The average time to compute the 1600 windows for one PD image frame is 19.1 s.

In Vivo Perfusion Imaging

A murine model of partial hindlimb ischemia was used [58] to study the feasibility of the methods for in vivo perfusion imaging (Fig. 2.5). Each mouse was anesthetized with 1.5% isofluorane vaporized in O_2 at a rate of 1 L/min via nose cone. Each animal underwent hindlimb occlusion of the right femoral artery, following the procedure described previously in [56, 58] without disturbing non-femoral peripheral flow to the right leg or any blood flow to the left leg. Briefly, the anesthetized mouse was placed on a 37°C heating pad, a small incision was made on the right leg to expose the femoral vasculature, and dual ligation of the femoral artery was performed distal to the profundus branch to induce unilateral hindlimb ischemia. To confirm the occlusion and the reduction of blood flow in ischemic hindlimb, animals were imaged with a Laser Doppler Imager (moorLDI, Moor Instruments, UK) before, and immediately after ligation. For US scanning at 24 hrs post-surgery, the anesthetized animal was placed in a supine position with hindlimbs extended, and the transducer scanned the shaved inner hindlimb along a longitudinal cross section that included muscle, bone and, vasculature. Fig. 2.5b displays a B-mode view of the anatomy. Although measurements were made on three mice, I will show results of scanning contralateral limbs of two mice specifically to compare methods. All experiments were performed with the approval of the Institutional Animal Care and Use Committee of the University of Illinois at Urbana-Champaign following the principles outlined by the American Physiological Society on research animal use.

2.2.3 Results

n order filter

In Fig. 2.6, I compare results of first, second, and third-order clutter filters for displaying the slow-time arterial flow (first three rows of images) and frame-time perfusion (last three rows of images). All results are obtained from the same echo-data array, viz., $\boldsymbol{\mathcal{X}} \in \mathbb{C}^{17\times 200\cdot 240\times 17}$. For the first and second-order filters, 17 post-filtered images are averaged over either the slow-time or the frame-time axes to take full advantage of all echo data. The third-order filter first decomposes the entire data array before projecting onto the appropriate subspace. The entire echo-data array influences each image displayed in Fig. 2.6. In each case, I selected filter parameters that provided the clearest visualization of RBC movement. From one set of recorded echo data, I can see the effects of filter order and data-array axis (eigen-basis) on the ability to visualize fast or slow-flow patterns in normal and ischemic hindlimbs. In particular, compare the noise levels in the third-order filter results with first and second-order results. A noticeable contrast improvement is observed.

The full impact of using 3-D data may be appreciated when I threshold and color code the power signals before overlaying them on the B-mode image (Fig. 2.7) as is traditionally displayed for clinical applications. I use a blue color map to display the slow-time-axis power (arterial flows) seen in Figs. 2.6 (E) and (F) and a red color map to display the frame-time-axis power (blood perfusion) from Figs. 2.6 (K) and (L). Colored PD images are displayed in the third row of Fig. 2.7. The inset shows 160 μm-dia vessels are clearly resolved.

The first and second rows of Fig. 2.7 display FIR-filtered PD images, and the third row shows HOSVD-filtered images. All are computed from the same echo-data array. I applied a fixed 25 Hz high-pass FIR filter in (A) and (B) and a 150 Hz high-pass FIR filter in (C) and (D). While surface vessels and bone artifacts can be seen in the 25 Hz FIR-filtered and the HOSVD images of Fig. 2.7, only HOSVD images show slow flow within interior vessels of the ischemic hindlimb and uniformly perfused muscle in proximal regions of healthy controls.

Sensitivity is reduced in distal muscle regions of all images as sound attenuation reduces SNCR.

2.2.4 Discussion

These preliminary data suggest the proposed changes in acquisition and filtering can greatly increase the sensitivity of ultrasonic power-Doppler perfusion imaging without contrast enhancement. The HOSVD filter allows us to separate fast and slow flows that I indicate with blue and red color maps in Fig. 2.7 (arrows in top row of Fig. 2.8 also indicate arterial flows). I was fortunate to capture a portion of the femoral artery in the ischemic image. This ligated vessel appears prominently in the perfusion image because it is weakly fed from collateral vessels. Also, at 24 MHz, the ischemic hindlimb perfusion image inset in Fig. 2.7 (E) clearly displays vessels with diameter smaller than 200 μm. These small vessels are less visible in the control hindlimb (F) where surrounding capillary perfusion reduces small-vessel contrast (not shown).

Baseline perfusion, which is 17 ml/min/100g in the normal hindlimb [59], falls to 60-70% of that value following femoral ligation [58]. Consequently, a 5-10 g hindlimb muscle has normal capillary flow in the range of 1-3 ml/min. A key element of successful HOSVD filtering is selection of the clutter and blood subspaces within core tensor, $\boldsymbol{\mathcal{G}}$. The standard selection method is based on eigenvalue information and echogenic properties of the sources as mentioned in Section **??**. Since there are only a few prominent elements in $\boldsymbol{\mathcal{G}}$, I now just try various filter ranges and inspect the resulting PD images to determine the "best" filter parameters. The following techniques using eigenvector information could guide a more objective and automated partitioning of $\boldsymbol{\mathcal{G}}$.

The top left PD image in Fig. 2.8 represents a different normal mouse hindlimb. Here I see two segments of arterial flow as indicated by arrows and the blue-green color. On the right, I reproduce the ischemic hindlimb image from Fig. 2.7 that displays no fast blood flow patterns. In both images, I box a region of interest that includes directed vascular flows away

from the transducer; on the left, flow velocity is in the range 2-15 mm/s and on the right the flow velocity is in the range ±0.2 mm/s.

In the second row of Fig. 2.8, I display the first nine odd spatial eigenvectors as gray scale images. These are taken from data in the boxed regions in the figures above. The absolute values of elements in each spatial eigenvector are reshaped back into the shapes of the 2-D image patches. Looking closely, I see the linear shape of the vessel within each eigenvector that is similar to that in the boxed image region above, except for the first eigenvector. The uniformity of spatial eigenvector 1 suggests it is dominated by clutter, while the appearance of a vessel-like structure in the other eigenvectors suggest they are influenced by directional blood flow in the vessel. For this reason, I eliminate at least the first spatial eigenmode through HOSVD filtering.

Images of the slow-time eigenvector spectra (third row in Fig. 2.8) and frame-time eigenvector spectra (fourth row) further reveal information about blood flow. In the first eigenvector spectrum (left-most column of the spectral images) the only nonzero value is at zero-frequency; consequently the first eigenvector offers no information about movement and should be discarded. The linear spectral pattern in the normal hindlimb slow-time spectral image between eigenvectors 5-10 (third row, left in Fig. 2.8) suggests a strong signal is present for fast directed blood flow. Because this flow is away from the transducer, the linear pattern appears along the negative-frequency axis, which shows there is directional flow information available. Notice the spectrum shows evidence of aliasing as the linear structure wraps from negative to positive frequencies at eigenvector 13. There is no linear spectral pattern for the normal hindlimb image in the corresponding frame-time spectrum (fourth row, left in Fig. 2.8) as expected for the slow, disorganized RBC movement associated with capillary perfusion. The red arrows along the abscissa indicate the upper and lower bounds on the eigenvector pass band set for HOSVD filtering.

There is also an asymmetric linear spectral pattern in the ischemic hindlimb image between eigenvectors 3-9 in the frame-time spectrum (fourth row, right in Fig. 2.8). This corresponds

to the relatively-slow but downward-directed flow within the large vessel in the ischemic tissue. I know it is slow flow because it is found in the frame-time spectrum and the linear pattern indicates the flow is directed. Conversely, the slow-time eigenvector spectrum for the ischemic leg (third row, right in Fig. 2.8) is symmetric and diffuse, indicating no directed fast flow in this region.

Future work includes imaging at lower transmission frequencies and higher frame-time rates to assess clinical utility in human subjects. The low frame rate used for the murine model is unlikely to span the wider range of perfusion velocities found in human tissue.

2.2.5 Conclusion

In this preliminary study, I found that expanding the dimension of the acquired echo-data array and then strategically reducing the data dimension using adaptive HOSVD filters leads to images that suggest improved perfusion sensitivity. At this point in development, the method offers images of signal power that describes relative flow and perfusion patterns.

HOSVD filtering appears to enhance the distinct information provided by each axis of the 3-D data array, enabling visualization of blood components of the echo signal while effectively suppressing clutter and noise components. The addition of frame-time data as a separate array dimension appears to allow increased sensitivity to slower flows through a longer acquisition period without discarding fast blood flow echoes offered by the slow-time array axis. One 3-D acquisition processed via HOSVD effectively displays both blood components.

Although I apply power-Doppler processing here, I note that the eigenvector spectra seen in Fig. 2.8 contain information about the direction and spatial coherence of RBC movement. In principle, color-flow imaging is possible. I applied 24 MHz ultrasonic pulses to couple the method to the small mouse model which enabled sub-millimeter vessel diameter flows to be imaged with 5-mm tissue penetration.

The price paid for adding the frame-time axis in the echo-power estimator is that each PD frame requires more than 1 s worth of data acquisition. Since perfusion is normally steady or

slowly varying, the long acquisition could be inconsequential depending on the application. The added sensitivity and lower noise justify the extra time and effort, especially when imaging stationary echo data that describe steady RBC movements, as for the application described in this report. Little effort has been made thus far to minimize the time required to compute one PD image frame, which now stands at 19.1 s.

2.3 Molecular imaging of $\alpha_V\beta_3$ integrin with dimeric cRGD probes

2.3.1 Introduction

The development of capillaries from preexisting vessels to form new vasculature, termed as angiogenesis, is tightly controlled by a delicate balance of pro- and anti-angiogenic factors. The main stimulators of blood vessel formation are vascular endothelial growth factor (VEGF) and basic fibroblast growth factor (bFGF), while endogenous inhibitors include thrombospondin, and angiostatin [25]. The process of creating new blood vessels is necessary for physiological function, but is also a hallmark of many pathological disorders such as inflammation, ischemic heart disease, and cancer. Over the last two decades, significant research efforts have been directed at developing novel targeted imaging techniques for the non-invasive assessment of angiogenesis as a tool for early diagnosis, prognostication, and monitoring of novel individualized therapeutic interventions focused on the modulation of the angiogenic process [60]. These efforts resulted in the discovery of numerous potential imaging targets including integrins, which play an important role in the regulation of angiogenesis [23]. Found in species ranging from sponges to mammals, integrins are heterodimer transmembrane glycoproteins consisting of α (150-180kD) and β (90kD) subunits. The cell surface receptor is composed of three parts: a large ectodomain, a single transmembrane domain, and a short cytoplasmic tail. Integrins, when activated by an intracellular ligand (*e.g.* talin or kindlin),

become capable of binding specific extracellular molecules in a unique combination of "inside-out" and "outside-in" signaling. In response, the integrins elicit a cascade of biochemical events that modulate gene expression, and regulate cytoskeleton organization [61–63].

Significant effort has been expended exploring the clinical utility of imaging $\alpha_V\beta_3$ [64, 65] expression associated with tumor angiogenesis and metastatic dissemination [66, 67]. For example, radiolabeled integrin peptide ligands with a pentapeptide motif Arg-Gly-Asp-Phe-Lys (RGDfK) have been used as tools in research aimed at developing radiotracers for clinical applications [68, 69]. Numerous linear and cyclic RGD peptides based (to a greater or lesser extent) on the RGDfK motif, in combination with a variety of pharmacokinetic modifiers, prosthetic groups or bifunctional chelators and radionuclides have been reported and used as diagnostic probes in animal studies and clinical investigations in the areas of oncology [70–80] and cardiology [81–84].

Multivalent interactions have been shown to play a key role in many biological processes [85]. This phenomenon was behind the rationale for the design of multimeric cRGD ligands. A series of such peptides labeled with ^{18}F, ^{64}Cu and ^{68}Ga for PET or ^{99m}Tc for SPECT imaging have been reported [86–90]. They demonstrated higher receptor binding affinity *in vitro* and better tumor retention *in vivo* when compared to their corresponding monomeric counterparts. PEG and other types of linkers have been employed as pharmacokinetic modifiers, resulting in significantly increased tumor uptake and enhanced clearance from noncancerous organs [91–95].

Comparisons of different RGD-based tracers have demonstrated that increasing the peptide multiplicity can greatly improve affinity, but above a certain threshold, highly multimeric compounds exhibit non-specific organ uptake that can limit their applicability as imaging agents. This led to the conclusion that the dimeric subclass of the RGD peptides is an optimal choice for the development of imaging agents for clinical applications [72, 80, 96]. The SPECT tracer ^{99m}Tc-3PRGD$_2$ [91, 97–100] as well as several RGD-based PET radiotracers [101–105], have already entered the clinical investigation stage [69]. In the design of the new $\alpha_V\beta_3$

targeted probe related to the previously reported $3PRGD_2$, I integrated several structural elements known for their positive impact on pharmacokinetic properties including PEG moieties and 1,2,3-triazole residues [106].

Here I report the synthesis and chemical characterization of $\alpha_V\beta_3$ integrin targeted ^{64}Cu-labeled dimeric-cRGD probe (designed for *in vivo* PET imaging) and its FITC-labeled fluorescent analogue (designed for *in vitro* imaging with single-cell resolution). Using established *in vitro* and *in vivo* models I evaluated its efficacy as an imaging agent at the receptor, single cell, organ, and whole-body levels with the emphasis on quantitative assessment of $\alpha_V\beta_3$ integrin expression in diabetic and non-diabetic rats following myocardial infarction (MI).

2.3.2 Methods

Synthesis and Chemical Characterization

The chemical characterization (NMR and HR-MS) of both ^{64}Cu-NOTA-PEG_4-$cRGD_2$ and FITC-PEG_4-$cRGD_2$ have been described in Supporting Information (Figures 2.9 - 2.23).

Reagents Diphenylphosphoryl azide (DPPA), N-(3-dimethylaminopropyl)-N'-ethylcarbodiimide hydrochloride (EDC), N,N-diisopropylethylamine (DIPEA), triethylamine (TEA), copper(II) sulfate pentahydrate ($CuSO_4 \times 5H_2O$), sodium L-ascorbate, triisopropylsilane (TIPS) were purchased from Aldrich (St. Louis, MO). Boc-PEG_4-OH and isothiocyanatobenzyl-1,4,7-triazacyclononane- 1,4,7-triacetic acid (p-SCN-Bn-NOTA) were obtained from Quanta BioDesign (Plain City, OH) and Macrocyclics (Dallas, TX), respectively. Fluorescein isothiocyanate (5-FITC) was obtained from AnaSpec (Fremont, CA). 8-Azido-3,6-dioxaoctanoic acid (N_3-PEG_2-OH) and Boc-L-glutamic acid bis-propargyl amide were the products of Peptides International (Louisville, KY). Cyclo [Arg(Pbf)-Gly-Asp(OtBu)-D-Phe-Lys] was prepared according to the literature method [107].

Synthesis The synthesis of both ^{64}Cu-NOTA-PEG$_4$-cRGD$_2$ and FITC-PEG$_4$-cRGD$_2$ has been described in detail below:

(1) cyclo[Arg(Pbf)-Gly-Asp(OtBu)-D-Phe-Lys(PEG$_2$-N$_3$)

To a solution of cyclo[Arg(Pbf)-Gly-Asp(OtBu)-D-Phe-Lys] hydrochloride (1.71 g, 1.80 mmol) and N$_3$-PEG$_2$-OH (0.43 g, 2.27 mmol) in DMF (10 mL) was added DPPA (0.59 mL, 2.72 mmol), followed by the addition of Et$_3$N (0.50 mL, 3.59 mmol). The reaction mixture was kept at 0 °C for 5 h, with occasional adjustments of the pH value (7-8) with Et$_3$N. Then, the mixture was diluted with THF (100 mL), EtOAc (300 mL), and 0.4 N HCl (100 mL). The organic layer was washed with saturated NaHCO$_3$ (2 × 100 mL), brine (100 mL), dried over Na$_2$SO$_4$, and evaporated. The residue was triturated with isopropyl ether, and the product was collected by filtration, washed with the ether and dried under vacuum to afford 1.80 g of **(1)** in 92.3% yield as a colorless solid. ESI-MS: m/z = 1105.56 $[M+Na]^+$; 1083.51 $[M+H]^+$.

(2) Boc-Glucyclo[Arg(Pbf)-Gly-Asp(OtBu)-D-Phe-Lys(PEG$_2$-(1,2,3-triazole) -1-yl-4-methylamide)]$_2$

To a stirred solution of **(1)** (1.765 g, 1.63 mmol) and Boc-L-glutamic acid bis-propargyl amide (0.253 g, 0.79 mmol) in a mixture of DMF (20 mL), t-BuOH (32 mL), and H$_2$O (11 mL) were added 0.2 M CuSO$_4$ x 5H$_2$O (2.6 mL) and 0.5 M sodium ascorbate solution (1 mL) at room temperature. After 1 h the reaction mixture was diluted with 1-BuOH (300 mL) and H$_2$O (200 mL). The organic layer was washed with H$_2$O (2 × 100 mL), and concentrated under reduced pressure. Addition of Et$_2$O resulted in a precipitate, which was collected by filtration, washed with Et$_2$O, and dried to give 1.95 g of **(2)** (99.6%).

(3) H-Glucyclo[Arg-Gly-Asp-D-Phe-Lys(PEG$_2$-(1,2,3-triazole)-1-yl-4 -methylamide)]$_2$ × 3 TFA

The protected peptide **(2)** (1.94 g, 0.78 mmol) was dissolved in 20 mL of a solution TFA/TIPS/H$_2$O (95/2.5/2.5, v/v/v) at room temperature. After 2 h, the reaction mixture was concentrated under reduced pressure and the deprotected crude product was precipitated

with cold Et_2O. It was collected by filtration, washed with Et_2O, and dried to give **(3)** in quantitative yield. ESI-MS: m/z = 591.07 $[M+3H]^{3+}$.

(4) Boc-PEG$_4$-Glucyclo[Arg-Gly-Asp-D-Phe-Lys(PEG$_2$-(1,2,3-triazole)-1-yl-4 -methylamide)]$_2$

A solution of Boc-PEG$_4$-OH (0.38 g, 1.04 mmol), N-hydroxysuccinimide (0.13 g, 1.13 mmol), and EDC hydrochloride (0.21 g, 1.10 mmol) in DMF (2 mL) was stirred at 0 °C. After 1 h, the ice bath was removed, and the reaction was allowed to proceed for 20 h at room temperature. The reaction mixture was then added to a stirred solution of **(3)** (1.65 g, 0.78 mmol) and DIPEA (0.73 mL, to adjust pH to 6) in DMF (15 mL). The reaction was allowed to proceed at room temperature for 6 h, with occasional adjustments of the pH value (7-8) with DIPEA. The reaction mixture was evaporated and the residue triturated with a mixture of acetonitrile and Et_2O. Precipitated peptide was collected by filtration, washed with Et_2O, and dried to yield **(4)** (1.85 g) as a crude product.

(5) H-PEG$_4$-Glucyclo[Arg-Gly-Asp-D-Phe-Lys(PEG$_2$-(1,2,3-triazole)-1-yl-4 -methylamide)]$_2$ × 3 TFA

Boc-protected peptide **(4)** (1.85 g) was dissolved in 20 mL of TFA/H_2O (90/10, v/v) solution, and the mixture was stirred at room temperature for 30 min. After evaporation of solvent, the residue was triturated with EtOAc and cold Et_2O. The crude product (1.50 g) was purified using preparative RP-HPLC to yield 735 mg of **(5)** as a white powder. The identity of the peptide was confirmed using HR-MS, monoisotopic mass calculated for $C_{88}H_{136}N_{28}O_{27}$: 2017.0128 m/z, $[M+H]^+$: 2018.0202; found: $[M+3H]^{+3}$ 673.3440 m/z, corresponding to molecular mass 2017.0079, accuracy 2.4 ppm.

(6) NOTA-PEG$_4$-cRGD$_2$ × 2TFA

Compound **(6)** was prepared in the reaction of peptide **(5)** (200 mg, 0.085 mmol) with p-SCN-Bn-NOTA × 3 HCl (50 mg, 0.089 mmol) in DMF (5.7 mL) in a presence of DIPEA used for adjustment of pH to 8 (room temperature, 20 h). The product was precipitated with EtOAc

and purified using preparative RP-HPLC to yield the title compound as a trifluoroacetate salt (57 mg, 24.9%) with a purity of 95.5% (Figure 2.9). The peptide was characterized by NMR (Tables 2.3 and 2.4) and HR-MS, m/z calculated for $C_{108}H_{162}N_{32}O_{33}S$ average mass: 2468.7361, monoisotopic mass: 2467.1702, $[M+H]^+$ 2468.1775; found: $[M+4H]^{+4}$ 617.7966 m/z, and monoisotopic $[M+3H]^{+3}$ 823.4048 m/z, which corresponds to molecular mass 2467.1724, accuracy 0.9 ppm.

(7) ^{64}Cu-NOTA-PEG$_4$-cRGD$_2$

Compound **(6)** was dissolved in 0.5 mL ammonium acetate buffer (100 mmol, pH 5.5) at room temperature. To the solution, about 37 MBq of Copper-64 (^{64}Cu) acetate in 0.02 mL ammonium acetate buffer (100 mmol, pH 5.5) was added. Radiolabeling was completed at room temperature after 30 min incubation and was confirmed by RP-HPLC (Agilent C18 column, flow 1 ml/min, CH_3OH/H_2O, 5/95, v/v) and thin-layer chromatography (Scan-RAM, LabLogic). For all experiments, radiochemical purity (% RCP) was at least 95%.

(8) Synthesis of FITC-PEG$_4$-cRGD$_2$

Compound **(8)** was prepared in the reaction of peptide **(5)** (300 mg, 0.127 mmol) with fluorescein-5-isothiocyanate (54.4 mg, 0.140 mmol) in DMF (4 mL) in a presence of DIPEA used for adjustment of pH to 8 (room temperature, 4 h). The peptide was precipitated with Et_2O and purified using preparative RP-HPLC to give 241 mg (71.9%) of the desired product as a trifluoroacetate salt with a purity of 97.7%. The structure of the peptide FITC derivative was verified using HR-MS, m/z calculated for $C_{109}H_{147}N_{29}O_{32}S$ average mass: 2407.6084, monoisotopic mass: 2406.0486, $[M+H]^+$: 2407.0559; found: $[M+4H]^{+4}$ 602.5226 m/z, and monoisotopic $[M+3H]^{+3}$ 803.0215 m/z, which corresponds to molecular mass 2406.0495, accuracy 0.4 ppm.

Ligand-Receptor Binding Kinetics Studies

All surface plasmon resonance (SPR) studies were performed with the BIAcore 3000 instrument (Biacore International AB, Uppsala, Sweden) at 25 °C on dextran-coated gold sensor chips (CM5, Research grade, GE Healthcare Bio-sciences AB, Uppsala) divided into four separate flow cells (three containing immobilized $\alpha_V\beta_3$ integrin receptor and one control). HBS-EP pH 7.4 (10 mmol HEPES, 3 mmol EDTA, 150 mmol NaCl, 0.002% TWEEN-20) was used as a running buffer.

Pre-concentration studies were performed to determine optimal pH conditions for receptor immobilization (see, Table 2.1).

Protein	pI	Optimal pH
Anti-hCD34	8.7	6.0
$\alpha_V\beta_3$	5.6	4.0

Table 2.1: Isoelectric points (pI) and optimal immobilization pHs for immobilized proteins.

Protein immobilization Pre-concentration studies were performed to determine optimal pH conditions for protein immobilization. This helped to ensure that the target levels of immobilized protein could be achieved precisely while also enabling us to conserve materials. Receptor solutions were prepared at 20 μg/mL with acetate buffer (10 mmol, pH ranging from 0.5 to 3.5, at -1.0 below the protein's isoelectric point, Table 2.1). Each receptor solution (20 μL) was injected at a flow rate of 5 μL/min, followed by a 5 μL injection of ethanolamine-HCL (GE Healthcare AB, Uppsala, Sweden) to clear out the binding surface of the receptor. The optimal pH of acetate buffer for each protein was selected according to the maximum level of protein immobilization reached in the pre-concentration study sensograms.

Integrin $\alpha_V\beta_3$ receptor (R&D Systems, USA) was irreversibly immobilized to a single flow cell via amine coupling with the dextran matrix. A recombinant human CD-34 (R&D Systems, USA), a protein with no known interaction with peptides based on cRGD structure, was

immobilized to a flow cell as a reference signal protein to account for non-specific interactions. Briefly, the surface was activated by injecting 35 μL of 50 mM N-hydroxysuccinimide (NHS, GE Healthcare AB) and 200 mM EDC (GE Healthcare AB) at 1:1 ratio (v/v) and a flow rate of 5 μL/min. Integrin $\alpha_V\beta_3$ receptor was dissolved at 20 μg/mL in 10 mM acetate buffer at its optimal pH and injected at 5 μL/min until the target surface immobilization level was reached (approximately 200-500 R.U. of immobilized receptor). After sufficient amount of protein was coupled, the surface was deactivated by injecting 35 μL ethanolamine. Kinetic studies with dimeric and monomeric cRGD ligands were performed on the target flow cell containing the immobilized integrin $\alpha_V\beta_3$ receptor and the reference flow cell simultaneously. 120 μL of each ligand (10, 20, and 40 nmol in HBP-EP running buffer) was injected at 30 μL/min through both flow cells, followed by a 10 minute running buffer injection to observe ligand-receptor dissociation. After recording SPR sensograms, a series of 5 μL HCl (5 mM) and 5 μL NaOH (10 mM) at 5 μL/min was injected to remove any remaining bound ligand residues. This cycle was repeated twice for each concentration of the ligand. The kinetic rate constants (association k_{on} and dissociation k_{off} constants), the goodness-of-fit parameter (χ^2) and the peak magnitude of the signal response (R_{max}) were determined by performing global kinetic analysis on the binding curves for each ligand-receptor pair (Supporting Information) [108–110].

Ligand-receptor kinetics measurements The kinetic rate constants were determined by performing global kinetic analysis on the binding curves for each ligand-receptor pair with the BIAevaluation software (Version 4.1.1, GE Healthcare). In global kinetic analysis, nonlinear least squares was used to determine the association and dissociation constants that produced the best fit for multiple response curves, simultaneously. Global analysis is considered to produce the most accurate results in comparison to fitting of a single response curve [111]. Raw sensogram were processed for a given ligand-receptor pair. Briefly, each raw response curve was aligned and subtracted from the reference cell signal of each receptor

signal to remove the effects of non-specific interactions. Once processed, a 1:1 Langmuir binding model (Equation 2.6) was fit to the data, and the association (k_{on}) and dissociation (k_{off}) kinetic constants, as well as the goodness-of-fit parameter (χ^2) and the peak magnitude of the signal response (R_{max}) were determined. This analysis was applied to each set of kinetic studies, except where the subtracted association phase was negative. A negative association curve occurs when the non-specific binding events on the reference cell exceed the binding events observed for the actual ligand-receptor pair; hence, it is indicative of a non-interaction.

$$L + R \underset{k_{off}}{\overset{k_{on}}{\rightleftharpoons}} LR \tag{2.6}$$

Next, the χ^2-to-R_{max} ratios were calculated which provide a well-established heuristic to determine the validity of obtained parameters for each ligand-receptor kinetic study. Previous studies have suggested that (χ^2) value obtained by fitting kinetic constants globally should be at least 10% of, or lower than, the signal's R_{max} (the change in signal from the highest level to the baseline) [108, 112].

Cell Culture

Human Umbilical Vein Endothelial Cells (HUVEC) were acquired from American Type Culture Collection (ATCC, USA) and grown to confluence in K-12 medium containing 10% heat-inactivated FBS (Invitrogen), 100 U/mL penicillin G, 100 μg/mL streptomycin, 0.25 μg/mL amphotericin B (HyClone) and were maintained in a humidified incubator at 37 °C with 5% CO_2.

Cellular Binding Studies

To investigate various cellular binding characteristics of radiolabeled ^{64}Cu-NOTA-PEG$_4$-cRGD$_2$ and its FITC-analogue, both gamma well counting and flow cytometry/fluorescence microscopy were used, respectively. HUVEC were incubated with ^{64}Cu-NOTA-PEG$_4$-cRGD$_2$

(0-100 nM) for 1 h at room temperature, filtered with 0.22 μm centrifuge filters (Corning Incorporated, USA), washed twice with PBS (pH 7.4) and radioactivity measured with gamma well counter (Wizard2, Perkin-Elmer, USA). HUVEC were also incubated in FITC-PEG_4-$cRGD_2$ (0-200 nM) for 1 h at room temperature. Cells were centrifuged, washed twice, and analyzed with a BD LSR II flow cytometer (BD Biosciences, USA) using gates set for FITC and corrected for auto-fluorescence. All experiments were performed in technical triplicates.

Integrin activation and deactivation To study the effect of $\alpha_V\beta_3$ integrin activation/deactivation on cellular binding, HUVEC were pretreated with of Mn^{2+} or EDTA (20 μM) for 10 min, washed with ice-cold PBS, and incubated with ^{64}Cu-NOTA-PEG_4-$cRGD_2$ (0-100 nM) or FITC-PEG_4-$cRGD_2$ (0-200 nM) for 1 h at room temperature. Cells were centrifuged, washed twice with PBS (pH 7.4), and analyzed with gamma well counter or flow cytometry using gates set for FITC and corrected for auto-fluorescence.

Competitive binding HUVEC were pretreated with 50 μM of unlabeled H-PEG_4-$cRGD_2$ for 30 min, and then incubated with ^{64}Cu-NOTA-PEG_4-$cRGD_2$ (0-100 nM) or FITC-PEG_4-$cRGD_2$ (0-200 nM) for 1 h at room temperature. Cells were centrifuged, filtered with 0.22 μm centrifuge filters (Corning incorporated, USA), washed twice with PBS (pH 7.4), and analyzed with gamma well counter or flow cytometry using gates set for FITC and corrected for auto-fluorescence.

Competitive inhibition (IC_{50} determination) HUVEC were incubated with 50 nM of ^{64}Cu-NOTA-PEG_4-$cRGD_2$ and increasing concentrations of H-PEG_4-$cRGD_2$ (0-1 μM) for 1 h at room temperature, filtered, and washed twice with PBS (pH 7.4), and transferred to counting tubes for gamma well counting.

Specificity In order to determine the specificity to $\alpha_V\beta_3$ integrin, HUVEC were incubated with FITC-PEG_4-$cRGD_2$ (0.34 μM) and co-incubated with phycoerythrin (PE) conjugated

anti-$\alpha_V\beta_3$ integrin antibody PE-LM609 (11.12 μg/ml) (R&D Systems, USA) for 1 h at room temperature. Cells were centrifuged at 5000 rpm for 10 min and washed twice with ice-cold PBS (pH 7.4). Gates were set for PE, FITC, and corrected for auto-fluorescence and potential overlap between the PE and FITC channels.

Dual-fluorescence staining HUVEC were grown to confluence on coverslips and fixed with 4% paraformaldehyde for dual-fluorescence staining with FITC-PEG_4-$cRGD_2$ (1 μM) and anti-$\alpha_V\beta_3$ PE-LM609 antibody (1:100, R&D Systems, USA). The coverslips were incubated with each stain separately for 1 h at room temperature, with washing buffer (PBS, pH 7.4) rinses before and after each incubation for a duration of 5 min. Coverslips were mounted to slides with DAPI Fluoromount (Southern Biotech, USA), imaged with a confocal fluorescence inverted microscope (Zeiss LSM 700 Confocal, Germany) equipped with 63x oil objective, preprocessed with commercial software package (ZEN 2012, Zeiss, USA), and colocalization analyzed with Fiji software [113].

In vivo Evaluation

Animal preparation All *in vivo* imaging experiments were performed with the approval of the Institutional Animal Care and Use Committee of the University of Illinois at Urbana-Champaign, following the principles outlined by the American Physiological Society on research animal use.

Blood clearance, metabolism and biodistribution To assess blood clearance and organ uptake dynamic *in vivo* PET-CT imaging was performed followed by image processing and analysis. Lewis rats (n = 6, Harlan Inc.) were anesthetized with 2% isoflurane, the neck area was shaved and a jugular vein cut-down procedure was performed to insert a PE-50 polyurethane catheter for radiotracer injection. Animals were then placed in supine position on the polyacrylic imaging bed of a small animal dedicated PET-CT scanner (Inveon, Siemens Healthcare, USA). At the time of PET acquisition, animals were injected with ∼22.2

MBq of ^{64}Cu-NOTA-PEG$_4$-cRGD$_2$ via the jugular vein catheter over 30 s followed by bolus infusion of 0.2 mL sterile saline. Animals underwent 60 min dynamic PET imaging (15% energy window centered at 511 keV) followed by anatomical X-ray CT imaging (80 keV, 500 μA, 100 μm spatial resolution). Following dynamic PET-CT imaging, both urine and feces samples were collected to assess radiotracer's metabolism and excretion route. The urine samples were collected at 90 min post injection by manual void, mixed at 1:1 ratio (v/v) with 50% CH_3CN and centrifuged at 5000 rpm. The supernatant was collected, analyzed by HPLC (C18 column, flow 1 mL/min, CH_3OH/H_2O, 5/95, v/v), and chromatograms compared to reference samples of ^{64}Cu-NOTA-PEG$_4$-cRGD$_2$ and ^{64}Cu-acetate. Feces samples were collected at 90 min post injection, suspended in 50% CH_3CN, homogenized and centrifuged at 5000 rpm. The supernatant was filtered and analyzed by RP-HPLC. For biodistribution studies, all animals were euthanized at 90 min post-injection and selected organ samples were collected for gamma well counting analysis. All collected sections were weighed and the tissue radioactivity was measured with Wizard^2 gamma well counter (Perkin-Elmer, USA). Measured ^{64}Cu activity was corrected for background, decay time, and tissue weight.

In vivo **imaging of myocardial angiogenesis** To evaluate the feasibility of ^{64}Cu-NOTA-PEG$_4$-cRGD$_2$ imaging in rodent model of myocardial ischemia, male diabetic and non-diabetic Lewis rats (n = 5 in each group) were subjected to surgical permanent ligation of left anterior descending (LAD) artery to induce anteriolateral myocardial infarction (MI) resulting in angiogenic response [114]. Type-1 diabetes was induced by bolus injection of 50 mg/kg streptozotocin (STZ), which resulted in hyperglycemia (> 200mg/dl glucose) and glucosuria at 6 weeks post STZ injection. To induce MI, animals were anesthetized with 1-3% isoflurane, and the respiration was controlled using an animal ventilator (Kent Scientific, USA) for a thoracotomy incision. Myocardial infarction was induced by ligating the proximal LAD coronary artery with 8-0 silk suture. One week after the surgery, all animals were anesthetized with 1-3% isoflurane, neck area shaved, and the left jugular vein was isolated for placement

of a PE-50 polyurethane catheter to facilitate injection of the radiotracer. All animals were injected with ∼29.6 MBq of ^{64}Cu-NOTA-PEG$_4$-cRGD$_2$. Imaging was performed using hybrid small animal microPET-CT scanner (Inveon, Siemens Healthcare, USA). Animals were placed on animal bed and ∼60 min after radiotracer injection, a 15 min microPET imaging was performed. This was followed by a high-resolution anatomical microCT imaging (360 projections, 80 keV/500 μA energy) during continuous (0.8 mL/min) intravenous infusion of an X-ray CT contrast agent (Omnipaque, GE Healthcare, USA) using programmable syringe pump (Kent Scientific, USA).

Image analysis and tissue processing The microPET and microCT images were reconstructed using OSEM/3D iterative algorithm (Siemens Healthcare, USA) and cone-beam technique (Cobra Exim), respectively. Both microPET and microCT images were fused, reoriented and visualized as short (SA), vertical- (VLA) and horizontal-long (HLA) axis slices using Inveon Research Workplace (Siemens Healthcare, USA). Immediately after last imaging session, all animals were euthanized with intravenous injection of KCl (1 mol/L), hearts excised and washed in ice-cold buffered saline. Both right and left ventricles were filled with dental molding material to facilitate uniform cutting into 2 mm slices. All slices were then divided into four sections; anterior, lateral, posterior and septal. Collected sections were weighed and tissue radioactivity was measured with Wizard^2 gamma well counter (Perkin-Elmer, USA). Measured ^{64}Cu activity was corrected for background, decay time, and tissue weight, and expressed as percent injected dose per gram tissue (%I.D./g).

2.3.3 Results

Synthesis and Chemical Characterization

The synthesis (Figure 2.9) began with coupling of N_3-PEG$_2$-OH to a selectively protected cyclopentapeptide, yielding azidopegylated protected peptide (**1**). An important aspect of the design was related to the dimerization method. Dimeric peptides have usually been prepared

by an acylation reaction using cRGD monomers and N-protected glutamic acid active esters, e.g. Boc-Glu(OSu)$_2$ as the substrates [87, 88, 115, 116]. In this case, the dimerization was achieved by employing Boc-glutamic acid bis-propargyl amide as an alkyne substrate to bridge two RGD pegylated cyclopentapeptides via the copper (I)-catalyzed 1,3-dipolar Huisgen cycloaddition, yielding the protected product (**2**). This is only the second synthesis of the cRGD dimer, after galacto-RGD$_2$, based on the aforementioned click reaction protocol [95]. Total deprotection of (**2**), followed by the PEGylation reaction using Boc-PEG$_4$-OSu, and Boc-group removal yielded compound (**5**). After RP-HPLC preparative purification, product (**5**) was used as the substrate for the synthesis of both tracers, ^{64}Cu-NOTA-PEG$_4$-cRGD$_2$ (**7**) and fluorescent analogue FITC-PEG$_4$-cRGD$_2$ (**8**). Briefly, product (**7**) was prepared in the reaction of (**5**) with p-SCN-Bn-NOTA, followed by the radiolabeling of NOTA-chelated compound (**6**). Reaction of (**5**) with fluorescein-5- isothiocyanate yielded the fluorescent product (**8**). Based on the ^{1}H, ^{13}C, DQF-COSY, TOCSY, NOESY NMR and H/C correlation spectra (gHSQC and gHMBC, Supporting Information, Figures 2.17-2.23), a full structural analysis of NOTA-PEG$_4$-cRGD$_2$ (**6**) was performed, including assignment of all proton and carbon resonances (Supporting Information, Table 2.3 and 2.4). To confirm the successful synthesis and measure masses of NOTA-PEG$_4$-cRGD$_2$ (**6**) and FITC-PEG$_4$-cRGD$_2$ (**8**), high-resolution MS spectra for pure products were registered in direct infusion mode. For product (**6**) the three- and four-fold charged molecular ions were identified on ESI spectrum (Supporting Information, Figure 2.23).

Dimeric cRGD Probe Binds Preferentially to the $\alpha_V\beta_3$ Integrin Receptor

Receptor binding kinetics We investigated the receptor binding kinetics of both the FITC- and ^{64}Cu-labeled tracers using surface plasmon resonance (SPR). As described in Methods and Supporting Information sections, initial pre-concentration studies were focused on adjusting the pH to optimize protein immobilization. I then evaluated the association and dissociation rates of the probes to the immobilized $\alpha_V\beta_3$ receptors and compared these

values with those of a commercially available monomeric probe, cRGDyK.

The SPR sensograms associated with each probe demonstrated significant accumulation upon initial injection (Figure 2.11). Their association phases were characterized by a sharp signal increase at the start of the injection, followed by a slow decrease following the injection. I observed that unlabeled dimeric probe bound $\alpha_V\beta_3$ with an affinity (K_d) approximately 50 times greater than the monomeric cRGD (Table 2.2), which was paralleled by a larger magnitude response $R_{max} = 10$ R.U. (Figure 2.11B) compared to ~ 5 R.U. (Figure 2.11A). Both labeled versions of the probe showed only marginally reduced binding affinity for $\alpha_V\beta_3$ relative to the unlabeled version, but they both outperformed the monomeric cRGD-based probe.

Probe	K_{on} (M^{-1} s^{-1})	K_{off} (s^{-1})	χ^2/R_{max}
NOTA-cRGD	2.7×10^5	2.6×10^{-6}	0.26
NOTA-PEG_4-$cRGD_2$	1.1×10^7	2.1×10^{-6}	0.22
FITC-PEG_4-$cRGD_2$	7.6×10^5	6.6×10^{-6}	0.19
^{64}Cu-NOTA-PEG_4-$cRGD_2$	7.1×10^5	1.1×10^{-6}	0.14

Table 2.2: Summary of binding affinity and kinetic rates measured between cRGD-based monomeric and dimeric probes and immobilized integrin $\alpha_V\beta_3$ receptor using a surface plasmon resonance-based approach. Kinetic constants were obtained by performing global kinetic analysis using the BIAevaluation software across several kinetic binding sensograms for each ligand-receptor pair.

Interestingly, although both labeled versions of the probe (Cu^{2+} and FITC) showed superior binding affinities for $\alpha_V\beta_3$ relative to the monomeric cRGD probe, neither performed as well as the the unlabeled version (Table 3). The diminished affinities were found to be mainly due to decreased association rates.

Binding affinity in HUVECs We next studied the cellular binding properties of both FITC-PEG_4-$cRGD_2$ and ^{64}Cu-NOTA-PEG_4-$cRGD_2$. HUVECs were first treated with FITC-PEG_4-$cRGD_2$ and co-incubated with the anti-$\alpha_V\beta_3$ antibody. Subsequent two-channel confocal fluorescent microscopic images (Figure 2.12 A-C) demonstrated a significant degree

of overlap between the fluorescein and phycoerythrin signals (Pearson's coefficient $\rho = 0.87$), which indicates a strong co-localization of FITC-PEG_4-$cRGD_2$ with $\alpha_V\beta_3$ integrin receptor. The specificity of FITC-PEG_4-$cRGD_2$ was further assessed on a single cell level using flow cytometry. Figure 2.12D shows a quadrant plot of HUVECs treated with FITC-PEG_4-$cRGD_2$ and co-incubated with the anti-$\alpha_V\beta_3$ antibody, which showed that FITC-PEG_4-$cRGD_2$ successfully bound over 99% of HUVECs expressing $\alpha_V\beta_3$ integrin.

To quantitatively evaluate binding parameters, cultured HUVECs were incubated with various concentrations of ^{64}Cu-NOTA-PEG_4-$cRGD_2$ and FITC-PEG_4-$cRGD_2$ followed by cellular binding assay with gamma well counting and flow cytometry. The observed radioactivity and fluorescence intensity was found to increase with probe concentration and fit well to a Hill-type function (Figure 2.13A and 2.13B). This allowed us to estimate the dissociation constant (K_d) at 38.27 nM and 33.85 nM for the FITC-PEG_4-$cRGD_2$ and ^{64}Cu-NOTA-PEG_4-$cRGD_2$, respectively. Both ^{64}Cu-NOTA-PEG_4-$cRGD_2$ and FITC-PEG_4-$cRGD_2$ also showed strong correlation ($R^2 = 0.95$) over the range of concentrations used in the cellular binding experiments (Figure 2.13C).

Binding affinity in the presence of metal ions We incubated HUVECs with either 20 μM of Mn^{2+} or EDTA and measured the B_{max} and K_d with flow cytometry and gamma well counting. The maximum fraction of bound receptors was found to decrease in the presence of EDTA (Figure 2.13) for both probes. Interestingly, the ^{64}Cu-labeled probe showed a significantly more pronounced decrease in B_{max}, which I attribute to the scavenging of ^{64}Cu by EDTA. The dissociation constants for both the ^{64}Cu- and FITC-labeled probes in the presence of EDTA were measured to be approximately 55 nM, indicating a similar effect on the binding kinetics.

In the presence of Mn^{2+} the probes' binding was found to increase by 78% when compared to HUVECs incubated without Mn^{2+} (Figure 2.13D). Likewise, the dissociation constant in the presence of Mn^{2+} was considerably lower reaching 13.8 nM.

Competitive binding Finally, I studied competitive $\alpha_V\beta_3$ integrin binding properties for the dimeric-cRGD probes. HUVECs were pre-treated with an excess of unlabeled NOTA-PEG_4-$cRGD_2$ (50 μM) followed by incubation with various concentrations of ^{64}Cu-NOTA-PEG_4-$cRGD_2$ or FITC-PEG_4-$cRGD_2$. This resulted in a noticeable decrease in B_{max} and an increase in the K_d (188 nM) compared to untreated cells (Figure 2.13AB). To determine IC_{50} values, HUVEC were treated with a fixed concentration of the probe (50 nM) and incubated with a range of unlabeled NOTA-PEG_4-$cRGD_2$ concentrations. The results of these experiments were fit to a model of homologous inhibition and yielded an approximate IC_{50} of 5.1 nM (Figure 2.13E) [117].

Pharmacokinetics, Biodistribution, and PET Imaging

Dynamic *in vivo* PET-CT imaging of $\alpha_V\beta_3$ integrin activity (Figure 2.14A) demonstrated favorable initial biodistribution and clearance kinetics for ^{64}Cu-NOTA-PEG_4-$cRGD_2$. Clearance kinetics from critical organs during the first 60 min after injection was quantified by placing volumes of interest (VOIs) on the dynamic co-registered PET-CT image sets. The radioactivity within these VOIs was expressed as percent injected dose per gram tissue (%I.D./g). The representative blood and tissue activity curves are shown in (Figures 2.14B and 2.14C). After intravascular injection, ^{64}Cu-NOTA-PEG_4-$cRGD_2$ cleared rapidly from the blood, accumulated primarily in the kidneys, and was excreted in the urine, which was retained in the bladder as early as 15 min after injection.

Figure 2.14D shows the biodistribution data of ^{64}Cu-NOTA-PEG_4-$cRGD_2$ at 90 min after intravascular injection into control rats and animals subjected to the LAD ligation. As expected, the highest uptake was observed in the kidneys due to renal filtration being the dominate excretion route (11.08 ± 2.20 and 3.66 ± 0.40 %I.D./g for cortex and medulla, respectively). Relatively high uptake was also observed in the intestines (4.62 ± 0.24), lungs (2.95 ± 0.43), and the spleen (2.25 ± 0.33). To assess *in vivo* stability of ^{64}Cu-NOTA-PEG_4-$cRGD_2$ I performed metabolism studies at the end of the dynamic PET-CT

acquisitions. Figure 2.15AB shows representative HPLC radiochromatograms of ^{64}Cu-NOTA-PEG$_4$-cRGD$_2$ prepared immediately before injection into the animal, and non-targeted ^{64}Cu-acetate in ammonium acetate buffer, respectively. These studies allowed us to determine the retention times for ^{64}Cu-NOTA-PEG$_4$-cRGD$_2$ and unbound ^{64}Cu, which were further used to demonstrate that more than 90% of ^{64}Cu-NOTA-PEG$_4$-cRGD$_2$ remained intact in the urine (Figure 2.15C) while there was no detectable activity in the feces (Figure 2.15D).

To explore the feasibility of *in vivo* imaging and quantification of $\alpha_V\beta_3$ integrin activation in the myocardium, static *in vivo* PET-CT images were performed at 90 min after injection of ^{64}Cu-NOTA-PEG$_4$-cRGD$_2$ in both diabetic and non-diabetic control rats one week after myocardial infarction. To better define the right ventricular (RV) and left ventricular (LV) myocardium I administered the iodine-based X-ray contrast agent Omnipaque (GE Healthcare, USA) during CT acquisition. Representative co-registered PET-CT images are shown in Figure 2.16A.

PET images of ^{64}Cu-NOTA-PEG$_4$-cRGD$_2$ demonstrated strong focal uptake of the tracer in the infarcted area (dashed arrows), as well as in the chest wall at the site of the thoracotomy (solid arrows). The significant increase in ^{64}Cu-NOTA-PEG$_4$-cRGD$_2$ activity within infarcted myocardium that was observed by PET-CT imaging was confirmed by quantitative gamma well counting of myocardial sections. The retention of the radiotracer was expressed as %I.D./g tissue and graphed as circumferential Bull's eye plots for myocardial slices spanning from the apex to the base, and divided into anterior, septal, posterior and lateral sections (Figure 2.16B). LAD ligation resulted in anterior-lateral infarct, which was characterized by an increased ^{64}Cu-NOTA-PEG$_4$-cRGD$_2$ uptake. Radioactivity within the infarcted anterior sections was approximately 4-fold higher than in non-infarcted septal regions at one week after myocardial infarction (Figure 2.16C). I have also demonstrated that diabetic animals had significantly reduced ($\sim 40\%$, $^*P < 0.05$) myocardial uptake of ^{64}Cu-NOTA-PEG$_4$-cRGD$_2$ within the infarct, whereas there was no significant difference in both border and remote sections of diabetic and non-diabetic rats.

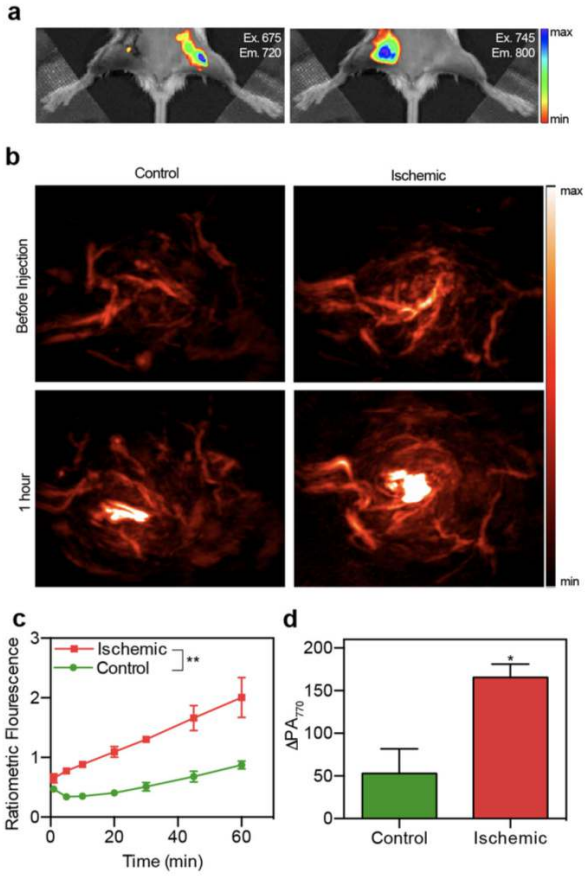

Figure 2.3: (a) IVIS Spectrum images acquired of hindlimb ischemia mouse model (right leg) 1 h following intramuscular injection (50 μL, 50 μM) of HyP-1 in both legs. Acquired using 675/720 nm (left) and 745/800 nm (right) filter sets. Mouse imaged in supine position. (b) PA images (770 nm) of the ischemic and control leg before and 1 h following injection of HyP-1 (50 μL, 50 μM). (c) Time-dependent ratiometric fluores-cence increase of ischemic and control limbs. (d) Time-dependent increase of PA signal of ischemic and control limbs. Results with error bars are represented by mean SD. *p $<$ 0.05, **p $<$0.01

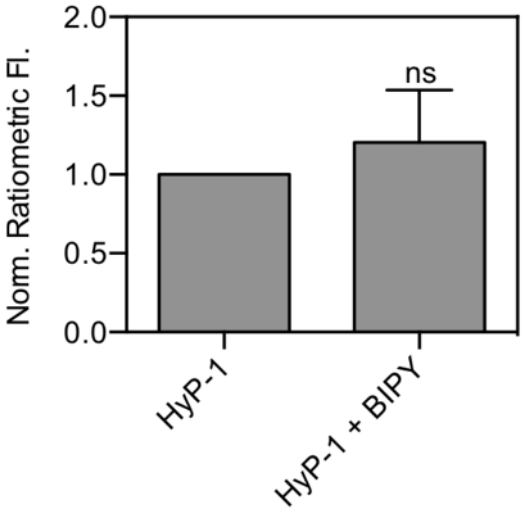

Figure 2.4: Normalized ratiometric fluorescence of ischemic hindlimbs following intramuscular injection of HyP-1 (50 μL, 50 μM) or HyP-1 + BIPY (5 mM). Surgical ligation of the femoral artery was performed on both hindlimbs of female BALB/c mice (6 weeks old). HyP-1 was injected intramuscularly into one of the hindlimbs, while a HyP-1 solution containing BIPY was injected into the other hindlimb. Images were acquired using 675/720 nm and 745/800 nm filter sets. Ratiometric fluorescence of the BIPY-treated hindlimb was normalized with respect to the control. Results are presented as mean SD (n = 3).

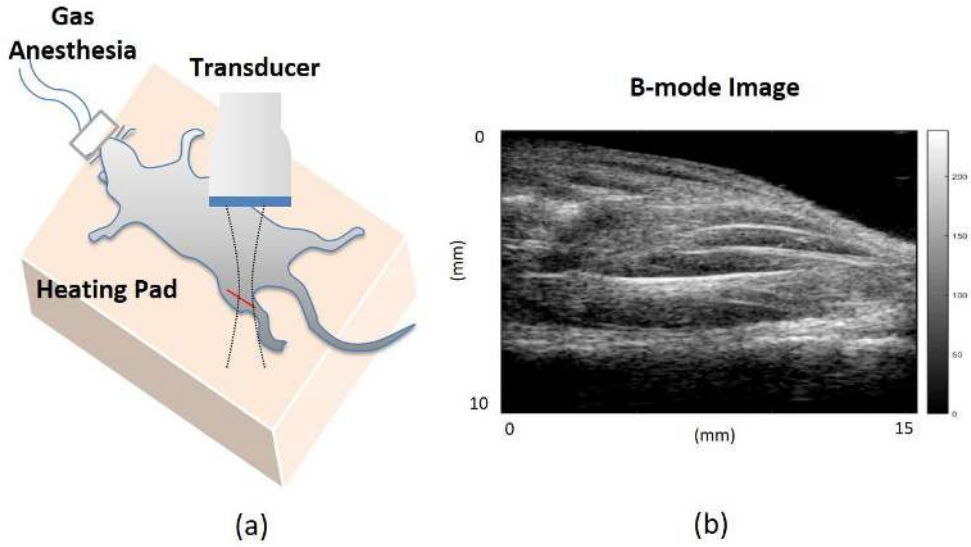

Figure 2.5: (a) An anesthetized mouse placed on a heated surface in a supine position is scanned with a linear array. (b) A longitudinal cross-section of the hindlimb is displayed as a B-mode image.

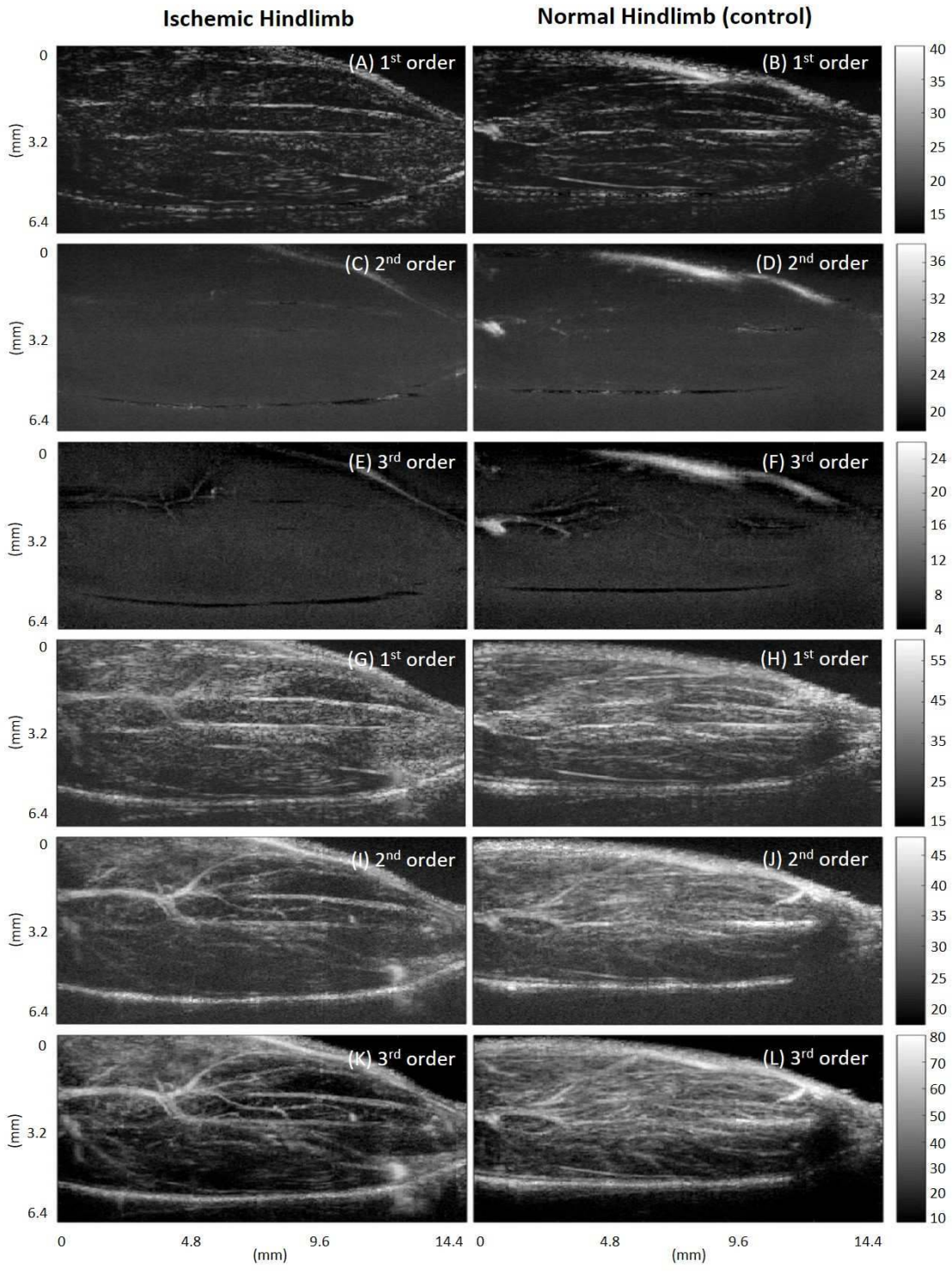

Figure 2.6: Comparisons of the visually clearest examples of first, second, and third-order filters applied to the slow-time data axis (A-F) to display arterial flow and to the frame-time data axis (G-L) to display perfusion. Each image is based on same 17 frames of echo data.

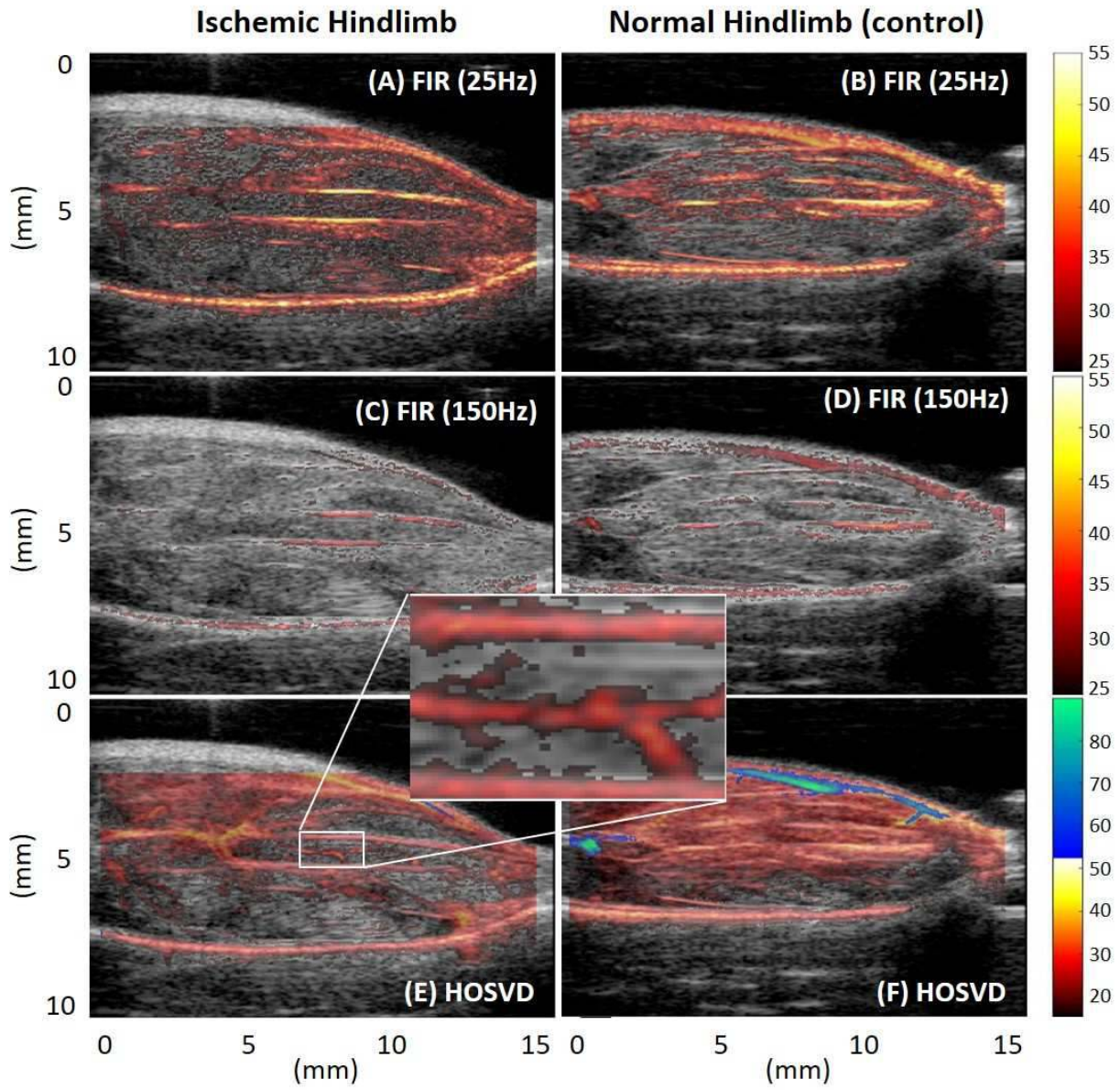

Figure 2.7: PD images are compared using standard FIR clutter filtering (first row: 25 Hz high-pass, second row: 150 Hz high-pass) and adaptive HOSVD filtering (third row) applied to the same data array. Notice that perfusion in the control limb is fairly uniform, except in distal regions where the SNCR is low. Conversely, the ischemic limb shows patchy perfusion throughout. The inset shows an enlargement of microvessels. Given that the PD pixel dimensions are 32 μm axially and 60 μm laterally, I are resolving 160 μm-dia vessels axially and 300 μm-dia vessels laterally. Axial resolution for 24 MHz pulses with 12 MHz bandwidth is $\sim$ 128 μm. The blue and red colorbars indicate, respectively, color maps related to slow-time power (dB) and frame-time power (dB).

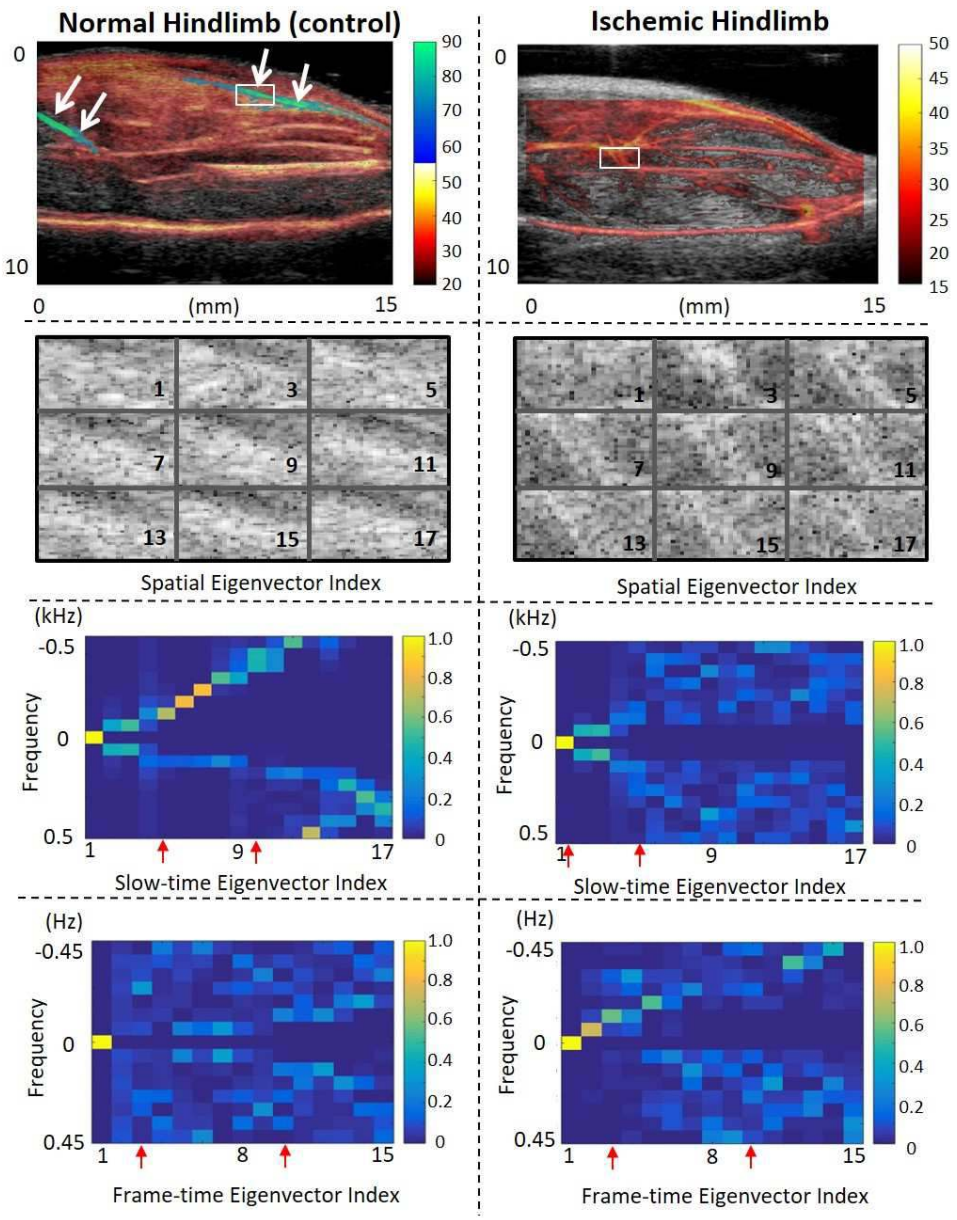

Figure 2.8: The two columns illustrate analyses of data within local regions of three images. Top row shows adaptive HOSVD images of normal and ischemic hindlimbs. White arrows indicate arterial flows, and boxes indicate analysis regions that include a vessel. The second row shows 9 of the first 18 spatial eigenvectors, some showing linear shapes similar to vessels seen in top row images. Third and fourth rows depict the power spectrum of slow-time and frame-time eigenvectors, respectively. The vertical axis is temporal frequency with the origin at the center, and the horizontal axis indicates eigenvectors along the corresponding axes, of which there are 17. Each column of the four spectral images is the absolute-square Fourier transform of the corresponding eigenvector. Eigenvectors between the red arrows were passed by the HOSVD filter for the images displayed in this report. Eigenvectors outside these ranges were removed by the filter.

Figure 2.9: Detailed synthesis of ^{64}Cu-NOTA-PEG$_4$-cRGD$_2$.

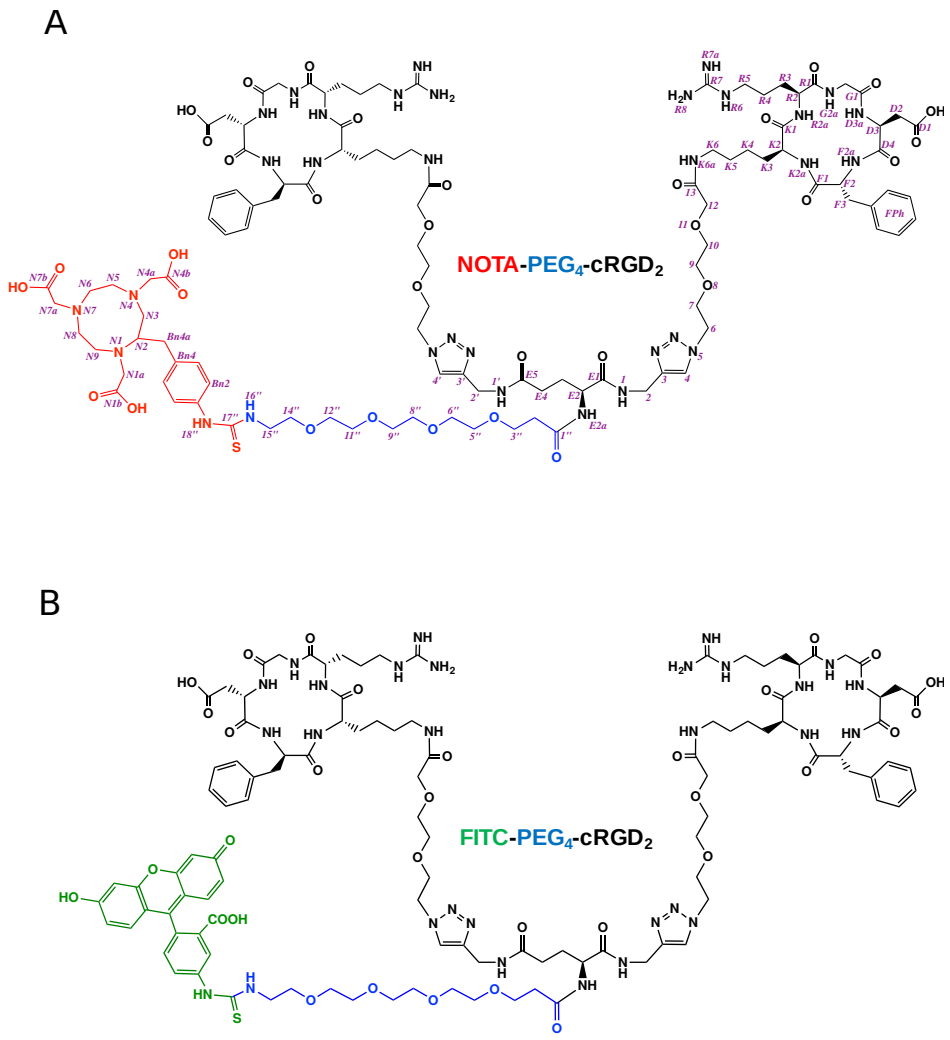

Figure 2.10: Chemical structures of (A) NOTA-PEG_4-$cRGD_2$ and (B) FITC-PEG_4-$cRGD_2$.

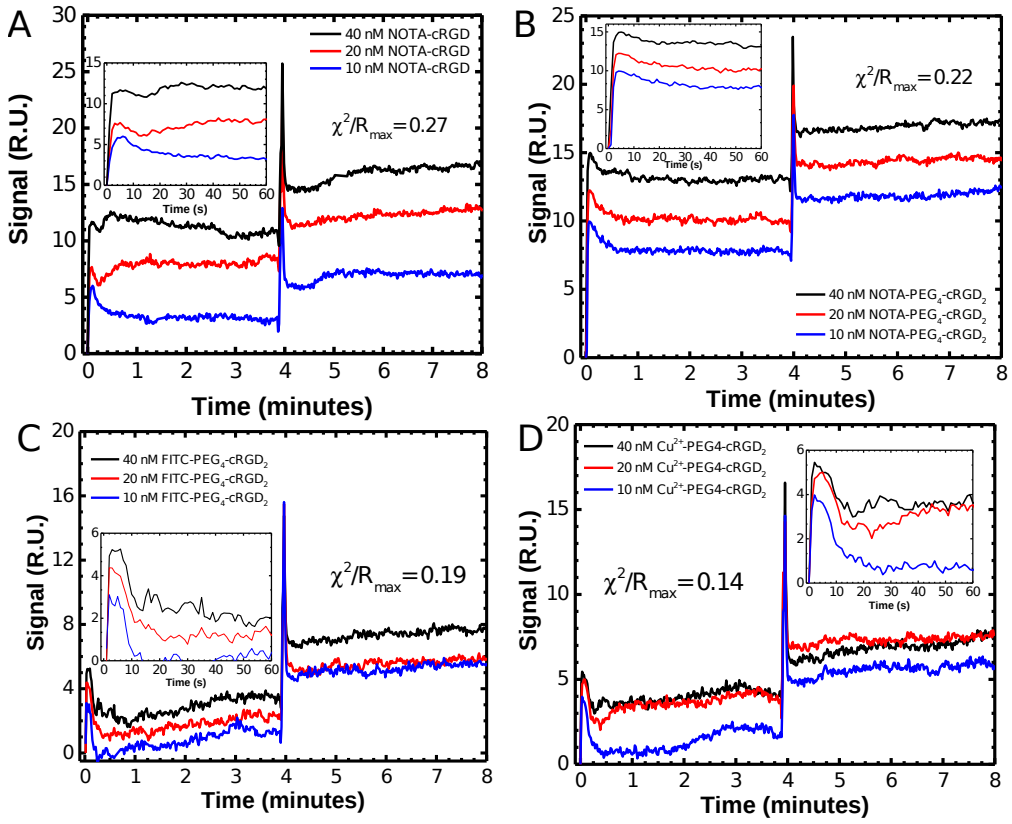

Figure 2.11: SPR sensograms depicting binding between cRGD ligands and $\alpha_V\beta_3$ integrin receptor. BIAcore 3000 kinetics studies of interactions between immobilized integrin $\alpha_V\beta_3$ receptor and (A) monomeric cyclic RGD probe (NOTA-cRGD), (B) dimeric cyclic RGD (NOTA-PEG$_4$-cRGD$_2$) probe, (C) cRGD$_2$ conjugated with FITC (FITC-PEG$_4$-cRGD$_2$), and (D) NOTA-PEG$_4$-cRGD$_2$ labeled with non-radioactive Cu^{2+}. Kinetic studies were performed at a 30 μL/min flow rate, with a 4 min association followed by a 10 min dissociation period.

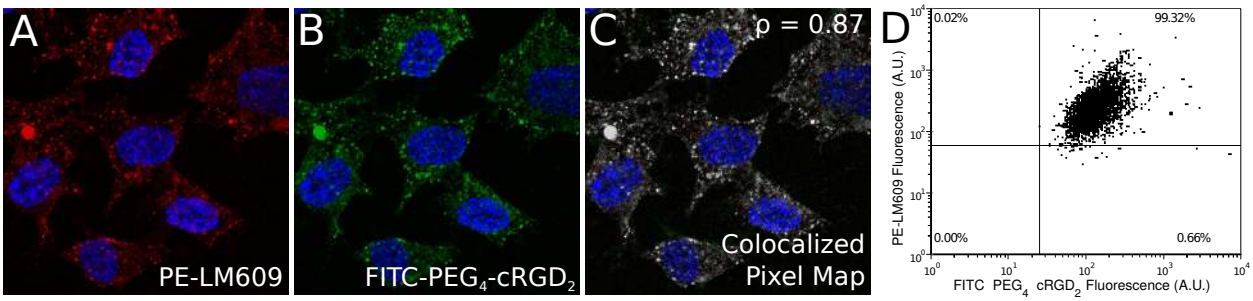

Figure 2.12: Colocalization between phycoerythrin-labeled anti-$\alpha_V\beta_3$ integrin primary antibody (PE-LM609) and FITC-labeled PEG_4-$cRGD_2$ probe. Human umbilical vein endothelial cells (HUVEC) were grown to confluency and incubated with both PE-LM609 and FITC-PEG_4-$cRGD_2$. Fluorescence microscopy images were acquired in DAPI/PE (A) and DAPI/FITC (B) channels and were superimposed to create colocalized pixel map (C) to calculate Pearson's coefficient. Flow cytometric analysis of HUVEC co-incubated with PE-LM609 and FITC-PEG_4-$cRGD_2$ demonstrated a very high degree of colocalization between integrin $\alpha_V\beta_3$ and FITC-PEG_4-$cRGD_2$ probe (D).

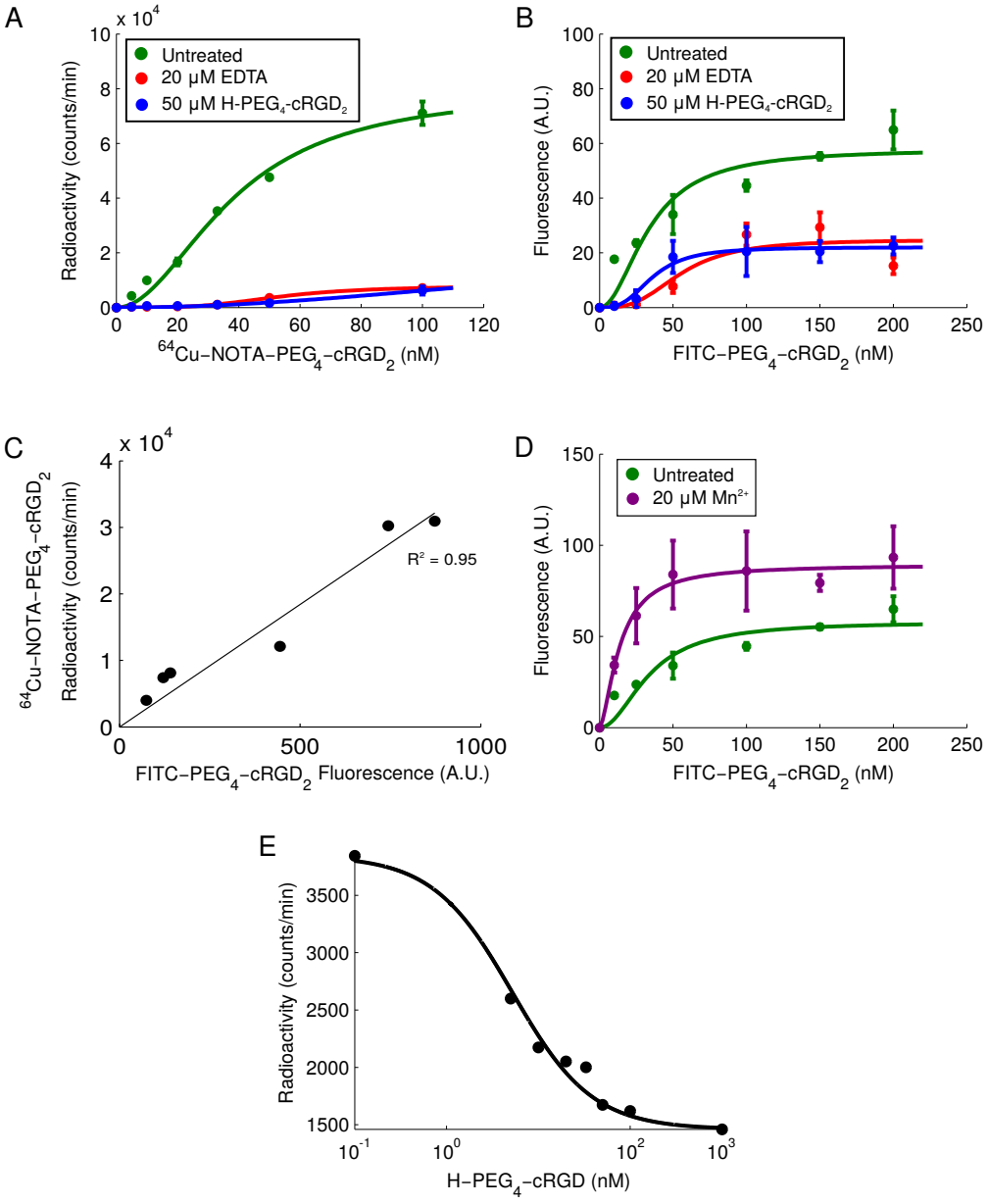

Figure 2.13: Binding kinetics of FITC and Cu^{64} labeled $cRGD_2$ probes. (A) Radioactivity of confluent HUVEC cells incubated with varying concentrations of ^{64}Cu-NOTA-PEG_4-$cRGD_2$ (green) and with either 20 μM EDTA (red) or 50 μM of H-PEG_4-$cRGD_2$ (blue). (B) Fluorescence of the FITC-PEG_4-$cRGD_2$ (green) with either 20 μM EDTA (red) or 50 μM of H-PEG_4-$cRGD_2$ (blue). (C) Correlation between FITC and Cu^{64} labeled $cRGD_2$ probes bound to HUVECs. (D) The fluorescence of HUVEC cells incubated with varying concentrations of FITC-PEG_4-$cRGD_2$ (green) and co-incubated with 20 μM of Mn^{2+} (purple). (E) Competition binding between ^{64}Cu-NOTA-PEG_4-$cRGD_2$ (50 nM) and increasing concentrations of unlabeled H-PEG_4-$cRGD_2$ in HUVEC cells.

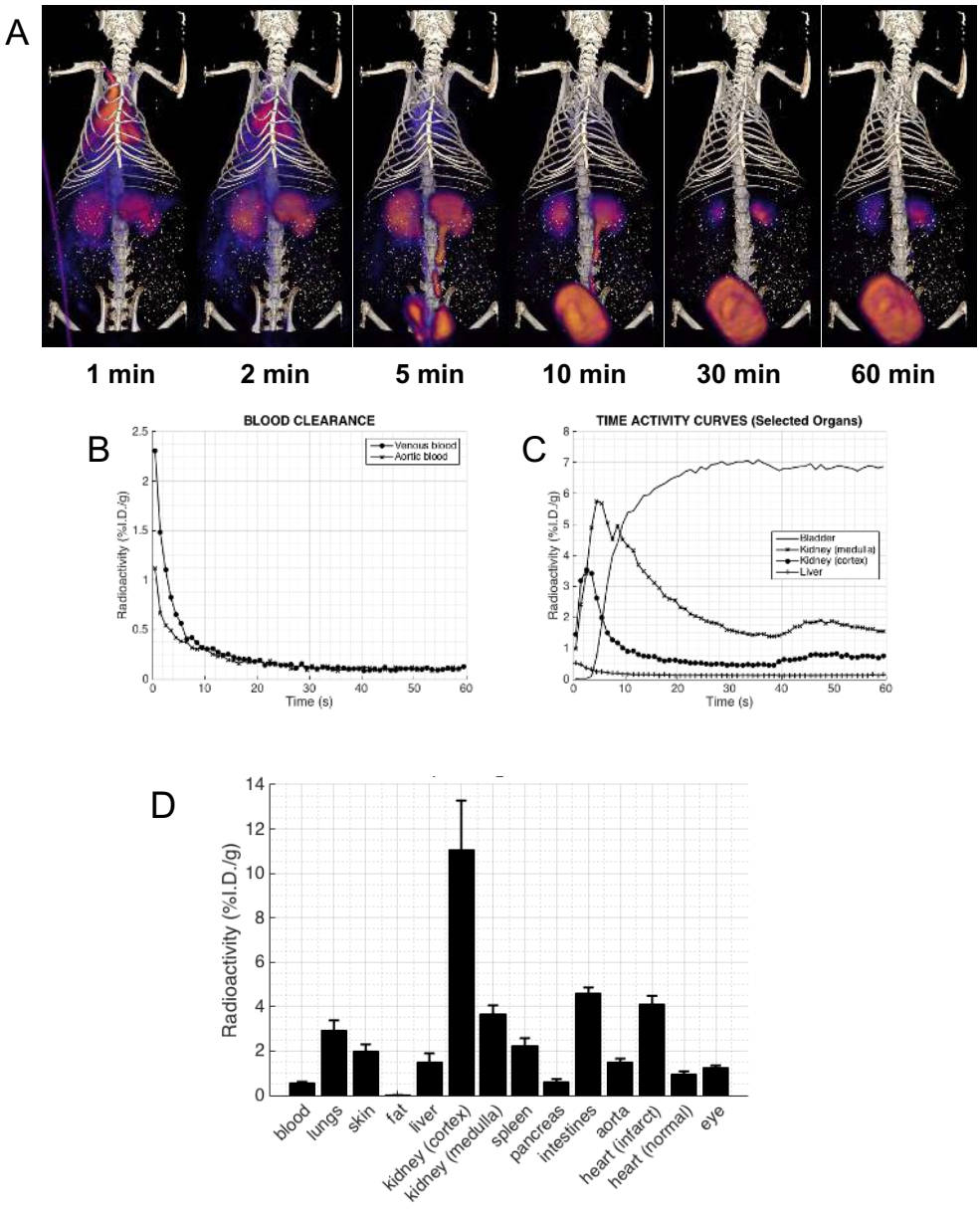

Figure 2.14: Dynamic PET-CT images (A) were used to plot the blood clearance (B) and time activity curves (TAC) of ^{64}Cu-NOTA-PEG$_4$-cRGD$_2$ in selected organs (C). (D) Biodistribution of ^{64}Cu-NOTA-PEG$_4$-cRGD$_2$ in selected organs at 90 min post- injection in Lewis rats subjected to myocardial infarction induced by surgical ligation of LAD. Results are expressed in percentage of injected dose per gram tissue (%I.D./g). These results suggest a rapid blood clearance through renal filtration and very low non-specific uptake in other critical organs.

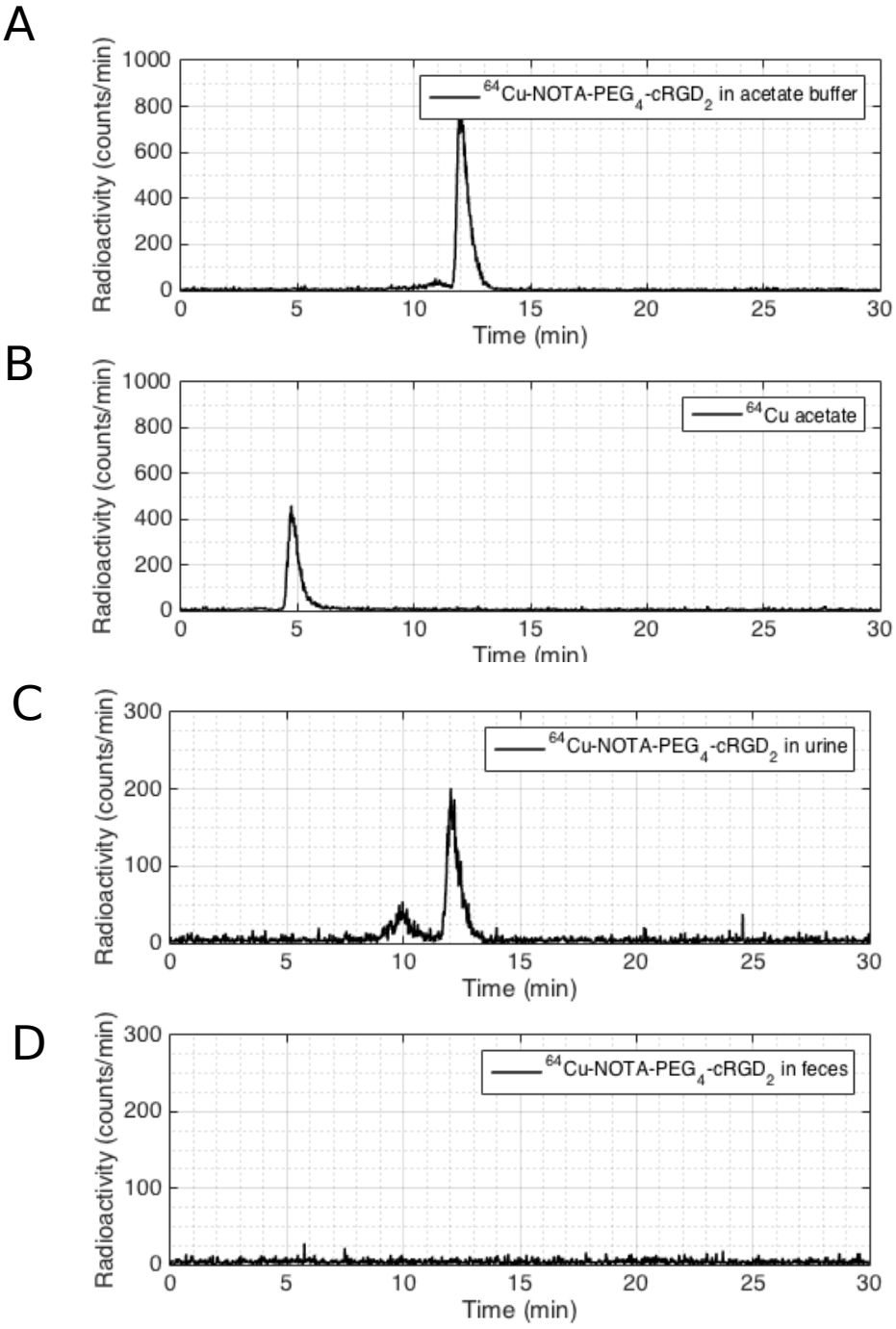

Figure 2.15: Representative radio-HPLC chromatograms for (A) ^{64}Cu-NOTA-PEG$_4$-cRGD$_2$ in acetate buffer 30 min after radiolabeling and immediately before injection, (B) ^{64}Cu-acetate used for radiolabeling, (C) ^{64}Cu-NOTA-PEG$_4$-cRGD$_2$ in urine at 90 min post-injection, and (D) ^{64}Cu-NOTA-PEG$_4$-cRGD$_2$ in feces at 90 min post-injection.

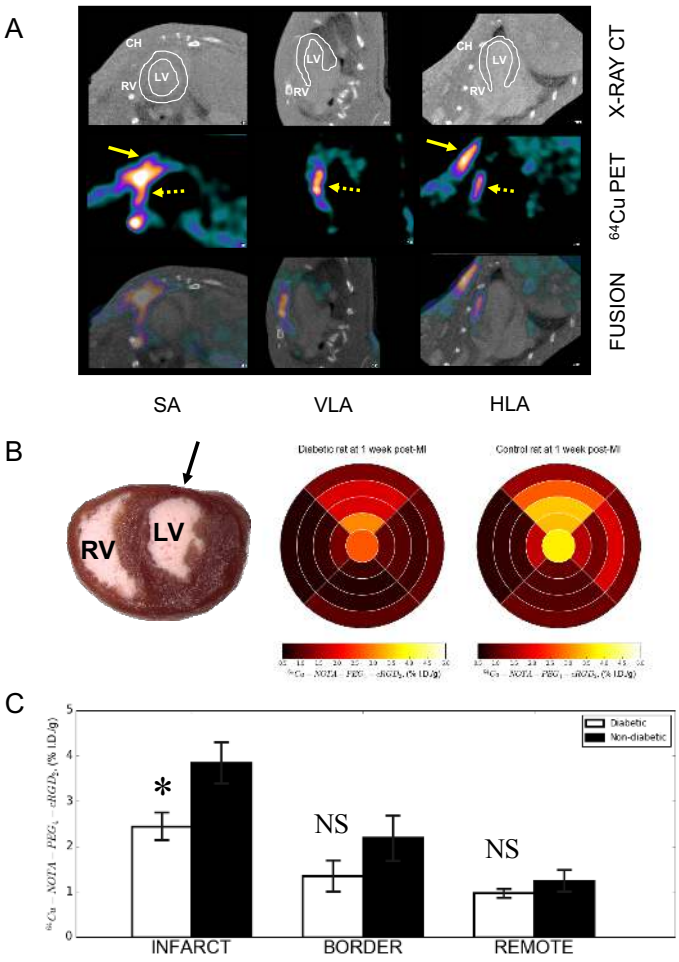

Figure 2.16: Representative in vivo hybrid PET-CT reconstructed short-axis (SA), vertical- (VLA) and horizontal long-axis (HLA) images acquired with iodinated contrast agent (Omnipaque) at 90 min post-injection of ^{64}Cu-NOTA-PEG$_4$-cRGD$_2$ (A). The iodinated blood pool contrast agent permitted better definition of right (RV) and left ventricle (LV) within the myocardium which is contoured with solid white line. Focal uptake of ^{64}Cu-NOTA-PEG$_4$-cRGD$_2$ was seen within anteriolateral LV regions (dashed yellow arrow) although significant uptake was seen in chest wall (CH) at the thoracotomy site (solid yellow arrows) indicating active wound healing associated $\alpha_V\beta_3$ receptor expression. Bull's eye myocardial plots of ^{64}Cu-NOTA-PEG$_4$-cRGD$_2$ activity in diabetic and non-diabetic Lewis rats subjected to surgical ligation of LAD to induce myocardial infarction (arrow) (B). Hearts were immediately excised at 120 min post-injection, cleaned and filled with inert dental molding material and cut in four 2-mm thick slices from apex to base. After removing right ventricle (RV), each left ventricular (LV) slice was cut in four segments (anterior, septal, posterior, lateral), and ^{64}Cu radioactivity was measured in each segment with gamma well counting. Data for each slice were expressed as percentage of injected dose per gram tissue (%I.D./g) and categorized as infarct, border and remote areas (C).

2.3.4 Discussion

Dimers constitute a valuable subclass of RGD cyclopeptides, characterized by better targeting capability and higher integrin-specific uptake, when compared to their monocyclic counterparts. In the past, a variety of linkers connecting two monomeric cyclic RGDs have been evaluated to modify radiotracer receptor binding affinity, organ uptake, biodistribution, and excretion kinetics from non-cancerous organs.

In this work, I describe the synthesis and chemical characterization of a novel dimeric cyclic-RGD probe for quantitative non-invasive imaging of $\alpha_V\beta_3$ activity followed by a multiscale biological analysis of probe's receptor binding and its pharmacokinetics. In a series of experiments I explored probe's *in vitro* binding affinity using surface plasmon resonance (SPR) with immobilized $\alpha_V\beta_3$ receptor and live endothelial cells expressing $\alpha_V\beta_3$. Finally, I evaluated the behavior of ^{64}Cu-NOTA-PEG$_4$-cRGD$_2$ *in vivo* and investigated its feasibility for non-invasive PET-CT imaging of $\alpha_V\beta_3$ expression following myocardial infarction in diabetic and non-diabetic animals.

We began the investigations by studying direct interactions between dimeric- and monomeric-cRGD probes and $\alpha_V\beta_3$ at the receptor level using surface plasmon resonance technique. SPR provides a powerful tool for the analysis of protein-protein and protein-ligand kinetics, including the determination of affinity, association and dissociation rates, and activation energies. SPR can be applicable even for low affinity systems which are often notoriously difficult to study using other techniques.

We demonstrated that the dimeric-cRGD construct is characterized by a very fast association to $\alpha_V\beta_3$ receptor ($k_{on} = 1.1 \times 10^7$ M^{-1} s^{-1}) which is approximately 40-fold greater than that of previously characterized monomeric cRGDfK ($k_{on} = 2.7 \times 10^5$ M^{-1} s^{-1}) see Table 2.2. In contrast, the receptor-bound dimeric-cRGD probe dissociated from the $\alpha_V\beta_3$ receptor at a much slower rate ($k_{off} = 2.1 \times 10^{-6}$ s^{-1}) than classical adhesive proteins like fibrinogen and vibronectin ($k_{off} = 9.8 \times 10^{-4}$ s^{-1} and 2.1×10^{-4} s^{-1}, respectively) [118]. All these results suggest that both dimerization and use of certain structural elements such as

PEG linkers and 1,2,3-triazole moieties, contributed to improved association to $\alpha_V\beta_3$ integrin (hence longer bound lifetime), while leaving dissociation properties essentially unchanged.

To study probe-receptor interactions at the cellular level in a biologically relevant model I used human umbilical vein endothelial cells (HUVEC), which are known to constitutively express $\alpha_V\beta_3$ integrin. The binding affinity (K_d) of fluorescein (38.27 nM) and ^{64}Cu-labeled (33.85 nM) dimeric cRGD probes were comparable to those of fibrinogen and vibronectin (27 nM and 64 nM, respectively). More importantly, the dissociation constant of the dimeric cRGD probes were approximately 20-fold smaller than most monomeric cRGD peptides, and similar to tetrameric cRGD probes reported in the literature [81]. Moreover, the dimeric-cRGD peptides have approximately only 2.5-fold lower affinity than $\alpha_V\beta_3$ integrin antibody (LM609, K_d = 14.4 nM), which suggests feasibility of ^{64}Cu-NOTA-PEG$_4$-cRGD$_2$ and FITC-PEG$_4$-cRGD$_2$ for high-sensitive targeted imaging of angiogenic activity. In addition, the tracer exhibits a nearly identical IC_{50} value (5.1 nM, see Figure 2.13E) as that reported for ^{18}F-Galacto-RGD (5 nM) [119]. While I have used endothelial cells in the own assay, I note that IC_{50} values can vary considerably from one cell-type to another [80]. This difference should be accounted for when comparing IC_{50} across cell lines.

Certain metal ions, when bound to the β_3 subunit of $\alpha_V\beta_3$, are known to induce a conformational change that can affect the binding of cRGD ligands [120]. Manganese (II) ions, for example, activate the $\alpha_V\beta_3$ integrin, while calcium ions or strong chelators like EDTA lead to its deactivation. To study this phenomenon, I incubated HUVECs with Mn^{2+} or EDTA. The addition of manganese led to a dissociation constant that was considerably lower (13.8 nM) in comparison to excess EDTA (Figure 4AB). These results support the notion that metal ions like Mn^{2+} play an important role in mediating the interactions between $\alpha_V\beta_3$ integrin and cRGD, and illustrate the important role of environmental conditions when assessing the binding characteristics and potential of cRGD-based probes as imaging agents.

Angiogenesis is a key factor in the process of cardiac healing after myocardial ischemia. Much work was focused at targeting angiogenesis for both diagnosis and therapy. For

this reason non-invasive methods for visualizing $\alpha_V\beta_3$ after myocardial infarction using both SPECT and PET have been reported in the literature. Noteworthy examples of radio-labeled $\alpha_V\beta_3$ probes include the ^{111}In-labelled SPECT tracer ^{111}In–RP748, Technetium-labeled SPECT tracers like ^{99m}Tc-RAFT-RGD, ^{99m}Tc-IDA-D-[c(RGDfK)]$_2$, and ^{99m}Tc-NC100692, as well as PET tracers such as ^{18}F-Galacto-RGD, ^{68}Ga-NODAGA-RGD, and the trimeric ^{68}Ga-TRAP(RGD)$_3$, all of which have been studied in animal models of myocardial infarction [121–125]. PET affords higher count numbers and sensitivity than SPECT (in part because PET does not use an extrinsic collimator), and as such the probe can be used to give more sensitive images with fewer artifacts than the available SPECT tracers. Moreover, the probe utilizes ^{64}Cu because of its favorable decay characteristics (half life 12.7h), which allow imaging at later time points than several other commonly used PET and SPECT isotopes like ^{18}F, ^{68}Ga and ^{99m}Tc (half life 110min, 68 min, and 6 hours, respectively). While the rapid pharmacokinetics of the radiotracer may speak to using a short half-life radionuclide, I chose to employ a longer half-life radioisotope which enabled the ^{64}Cu-NOTA-PEG$_4$-cRGD$_2$ to be more broadly applicable: the required ^{64}Cu can be produced at a nearby cyclotron facility and then used hours to a day later without requiring the type of on-site isotope production facilities that shorter-lived isotopes do. Moreover, the NOTA chelating moiety on the probe enabled fast single step labeling ($\sim$ 60 min) at room temperature. Other imaging probes can require higher temperatures and much long preparation times. The preparation of ^{18}F-Galacto-RGD, for example, requires temperatures as high as 70 °C and takes approximately 200 minutes—significantly longer than the halflife of the ^{18}F radionuclide itself [107].

While several multimeric cRGD-based probes have been described in that past, it has been found that little sensitivity or specificity is gained by increasing the cRGD multiplicity past two cRGD units [122, 125]; as such, I have focused here on enhancing the pharmacokinetic properties of a dimeric cRDG probe. In designing the structure of the dimer I decided to employ two PEG linkers, and 1,2,3-triazole moieties. Combining both of these structural

elements as pharmacokinetic modifiers was expected to improve the biodistribution and elimination of the tracer [106]. Additionally, I used NOTA when labeling with ^{64}Cu, which has been shown to exhibit lower accumulation in the liver than other available bifunctional chelators such as DOTA [126].

The favorable effects of these structural modifications on both pharmacokinetics and organ retention were verified with dynamic PET imaging followed by biodistribution studies, which provided vital insight into the *in vivo* behavior of ^{64}Cu-NOTA-PEG$_4$-cRGD$_2$. Within minutes after injection, I observed a rapid blood clearance of ^{64}Cu-NOTA-PEG$_4$-cRGD$_2$ with paralleled retention within kidney medulla and cortex. I also observed almost complete clearance after one hour with little gastrointestinal activity (Figure 2.14), which I attributed to the hydrophilicity of ^{64}Cu-NOTA-PEG$_4$-cRGD$_2$. I found high kidney and bladder retention, but essentially no detectable radioactivity in feces (Figure 2.15), indicating the main excretion route is through kidney filtration and urine (which has also been observed in other cRGD-based radiotracers [88, 125]).

While many of the previous studies of myocardial infarction employed healthy animals, here I focused specifically on imaging myocardial infarction in diabetic rats. High resolution microPET-CT imaging using ^{64}Cu-NOTA-PEG$_4$-cRGD$_2$ in diabetic and non-diabetic rats subjected to LAD ligation and subsequent myocardial infarction demonstrated both discrete and focal myocardial distributions (Figure 2.16). the probe was found to localize to the infarcted tissue within the anterio-lateral region of the heart, and this *in vivo* imaging pattern was obtained consistently for different rats (both diabetic and non-diabetic) at 1 week after surgical induction of myocardial infarction. Importantly, I found that the ratio of probe uptake in the infarcted region of the heart compared to a normal region was significantly higher in non-DM rats than in DM rats (3.85$\pm$0.51 versus 2.44$\pm$0.35, respectively), indicating decreased $\alpha_V\beta_3$ activity and, in turn, decreased capacity for neovascularization in rats with diabetes. Similar infarcted vs. normal myocardial segments for healthy rats have been reported in prior studies (4.7 ± 0.8 using ^{18}F-Galacto-RGD, 5.2 ± 0.8 using ^{68}Ga-NODAGA-RGD, and

4.1 ± 0.7 using ^{68}Ga-TRAP(RGD)$_3$ [121, 125]).

We found that the greatest $\alpha_V\beta_3$ activity occurred 1 week after induction of myocardial infarction in both healthy and diabetic rats, a finding in good agreement with previous studies using other RGD-based tracers in non-DM rats [124, 125]. This delayed $\alpha_V\beta_3$ uptake is a critical point to consider when designing potential stem-cell-based therapies for patients with myocardial infarction, especially those with other pathologies like diabetes that may limit their innate capacity for neovascularization. In particular, in diabetic patients, early detection and treatment could prove extremely important to myocardial infarction recovery, and to that end, rapid non-invasive imaging strategies like ours could play an important role in the clinical setting.

We demonstrated that *in vivo* targeted $\alpha_V\beta_3$ integrin imaging can be performed in combination with contrast CT imaging. The administration of X-ray contrast agent did improve definition of the myocardial edges and the blood pool. These *in vivo* PET-CT images with contrast provided better localization of ^{64}Cu-NOTA-PEG$_4$-cRGD$_2$ to the site of the myocardial infarction within the anterior-lateral wall and allowed for differentiation between the myocardial wall and thoracotomy site, which was characterized by active wound healing associated $\alpha_V\beta_3$ integrin expression. Moreover, the use of the X-ray contrast agent permitted reconstruction of the $\alpha_V\beta_3$ images without the need for a reference perfusion image. Reconstruction and orientation of the PET images was extremely difficult without the reference CT images. The image properties of ^{64}Cu-NOTA-PEG$_4$-cRGD$_2$ are superior due to the low background activity.

This combination of both anatomical and molecular targeted imaging with dimeric-cRGD-based agents holds great promise for non-invasive quantitative assessment of different uptake patterns observed within the myocardium of diabetic and non-diabetic animals post-MI. The results strongly suggest reduced $\alpha_V\beta_3$ integrin activation in the onset of diabetes. While the observed regional fluctuations in the radiotracer's retention remain in general agreement with previously reported observations with monomeric cRGD based SPECT and PET imaging

agents or more invasive non-imaging techniques [60, 81], targeted molecular imaging with ^{64}Cu-NOTA-PEG$_4$-cRGD$_2$ demonstrated excellent quality images, higher or comparable specific uptake within infarcted tissue, and relatively low non-specific uptake in critical organs. All told, these imaging results clearly indicate that the dimeric-cRGD probe has a potential for quantitative mapping of spatial and temporal changes in $\alpha_V\beta_3$ activation in small animal models of myocardial injury in the onset of diabetes as well as potentially expanding these studies to larger animals and humans.

2.3.5 Conclusion

During the last decade, much effort has been expended on the chemical modification of RGD peptides to increase affinity for $\alpha_V\beta_3$ integrin. Recent studies suggested that cyclic RGD dimers have high affinity due to bivalency and have relatively low non-specific uptake in other critical organs. These properties can be further optimized by modification of the distance between the two RGD motifs using PEG linkers. It was also shown that introduction of 1,2,3-triazole moieties has a positive impact on the pharmacokinetic profile of receptor-binding ligands. All of this has been taken into consideration during the development of the dimeric cRGD probe. This study described the synthesis, chemical characterization, and multi-scale biological evaluation of both radiolabeled and fluorescent dimeric RGD peptide ligands for molecular imaging of $\alpha_V\beta_3$ integrin activation at the receptor, single cell, organ and whole-body level. Here I demonstrated that the targeted PET-CT imaging of regional activation of $\alpha_V\beta_3$ integrin within ischemic tissue holds the potential to directly quantify the extent and localization of ongoing angiogenic process *in vivo* and to assess this process on cellular level *in vitro* using optical imaging with a fluorescent analogue of the targeted imaging agent. The enhanced focal retention, favorable blood clearance kinetics and biodistribution, and excellent quality of images obtained with ^{64}Cu-NOTA-PEG$_4$-cRGD$_2$ suggest the potential for future clinical translation. This and other molecular imaging-based approaches should lead to better understanding of pathophysiology and development of novel paradigms for patient

management.

2.3.6 Supporting Materials

Synthesis and Chemical Characterization

NMR spectra were recorded with a Varian Unity 500 spectrometer (Palo Alto, CA) in DMSO-d6/TFA. 2D NMR techniques including DQF-COSY, NOESY, TOCSY, gHSQC and gHMBC were used to confirm the structure of the synthesized NOTA-PEG_4-$cRGD_2$. Preparative RP-HPLC purifications were performed using a Shimadzu preparative system consisting of two LC-8A pumps controlled by a Shimadzu SCL-10A system controller, and a Shimadzu UV/VIS detector SPD-6A (λ=220 nm) equipped with a preparative flow cell. A Prochrom preparative column (50 mm x 35 cm) packed with Luna C18 (100$\mathring{A}$ pore size, particle size 10 μm) from Phenomenex (Torrance, CA) was used for the separations at a flow rate of 100 mL/min. Analytical HPLC runs were performed on Jupiter (Phenomenex) C18 column (4.6 mm x 250, pore size 300$\mathring{A}$, particle size 5 μm) with a flow rate of 1 mL/min. Peptides were eluted using a linear gradient of 0.05% trifluoroacetic acid (TFA) in CH_3CN (Solvent B) and 0.05% aqueous TFA (Solvent A). High-resolution (HR) mass spectra (MS) were recorded on HR electrospray mass spectrometer (Waters Synapt G2-Si ESI MS). MS experimental conditions were as follows: the capillary voltage 3.5 kV, sample cone 25 V, source offset 80, source temperature 100 °C, and desolvation temperature 150 °C, cone gas nitrogen 5 L/h, desolvation gas nitrogen 800 L/h, nebuliser gas nitrogen 6.5 bar. Whole samples were run by flow injection, and the mobile phase was CH_3CN/water (1:1, v/v) at a flow rate of 100 μl/min.

Within NOTA fragment all carbon resonances were distinguishable, however direct labeling of few protons and carbon signals by N5, N6, N8, N9, N1a, N7b and N1b, N4b, N7b was not possible (Figure 2.10). Also, due to the compound symmetry, the two identical cRGD fragments cannot be differentiated; however, their integration in comparison to well separated H-E3 and H-E4 protons could serve as proof of their presence. The amino acid sequence was

established based on the NOE's NH/CHα and the H/C NH/C=O/CHα correlation.

H and C atoms of the PEG and triazole fragments between lysine and glutamic acid, were assigned upon series of H/C and NOE correlations, namely: H-K6/C-13/H-12/C-10/H-10 and H-6/H-9, H-6/H-7, H-4/H-6, H-4'/H-6, H-2/H-4, H-2'/H-4', H-2/H-1/H-E2, H-2'/H-1'/H-E4. Similarly, bonds between glutamic acid and PEG as well as between benzyl groups and NOTA were established.

Supporting Tables

loc	nr	group	δ (ppm)
Glu	E2	CH	4.22
	E2a	NH	8.00
	E3	CH_2	1.70, 1.88
	E4	CH_2	2.09, 2.12
triazole	1/1′	2 × NH	8.33/8.26
	2/2′	2 × CH_2	4.28/4.26
	4/4′	2 × CH	7.82/7.85
PEG	6	2 × CH_2	4.47
	7	2 × CH_2	3.79
	9,10	4 × CH_2	3.53
	12	2 × CH_2	3.81
Lys	K2	2 × CH	3.90
	K2a	2 × NH	8.02
	K3	2 × CH_2	1.39, 1.52
	K4	2 × CH_2	0.99
	K5	2 × CH_2	1.29
	K6	2 × CH_2	3.00
	K6a	2 × NH	7.62
Arg	R2	2 × CH	4.14
	R2a	2 × NH	7.58
	R3	2 × CH_2	1.45, 1.69
	R4	2 × CH_2	1.35
	R5	2 × CH_2	3.08
	R6	2 × NH	7.48
	R7a, R8	2 × (2 × NH_2)$^+$	6.80, 7.20
Gly	G2	2 × CH_2	3.23, 4.02
	G2a	2 × NH	8.35
Asp	D2	2 × CH_2	2.37, 2.69
	D3	2 × CH	4.62
	D3a	2 × NH	8.06
Phe	F2	2 × CH	4.43
	F2a	2 × NH	7.96
	F3	2 × CH_2	2.80, 2.89
	FPh	10 × CH	7.10, 7.16, 7.22
PEG	2″	CH_2	2.38
	3″	CH_2	3.55
	5″, 6″, 11″, 12″	CH_2	3.46
	8″, 9″, 14″	CH_2	3.52
	15″	CH_2	3.62
	16″	NH	7.69
	18″	NH	9.60
NOTA	Bn2, Bn3	4 × CH	7.18, 7.40
	Bn4a	CH_2	2.51, 2.80
	N2	CH	3.33
	N3	CH_2	2.97, 3.04
	N	7 × CH_2	2.7–4.0

Table 2.3: ^{1}H NMR data of NOTA-PEG_4-cRGD_2 in DMSO-d6/TFA

loc	nr	group	δ (ppm)
Glu	E1	C=O	171.4
	E2	CH	52.2
	E3	CH_2	28.2
	E4	CH_2	31.7
	E5	C=O	171.4
triazole	2/2′	CH_2	34.3
	3/3′	C=C	144.8
	4/4′	=CH	123.0
PEG	6	CH_2	49.3
	7	CH_2	68.6
	9,10	$2 \times CH_2$	68.3
	12	CH_2	70.1
	13	C=O	169.1
Lys	K1	C=O	172.2
	K2	CH	54.5
	K3	CH_2	30.7
	K4	CH_2	22.7
	K5	CH_2	28.7
Arg	R1	CH	171.3
	R2	C=O	51.9
	R3	CH_2	28.7
	R4	CH_2	25.2
	R5	CH_2	40.3
	R7	C=N	156.6
Gly	G1	CH_2	169.6
	G2	C=O	43.2
Asp	D1	CH	171.7
	D2	C=O	34.9
	D3	CH_2	48.4
	D4	C=O	170.1
Phe	F1	CH	170.7
	F2	C=O	54.3
	F3	CH_2	37.3
	FPh	C_6H_5	126.2, 128.2, 129.1, 137.3
PEG	1″	C=O	170.3
	2″	CH_2	35.8
	3″	CH_2	66.6
	5″, 6″, 11″, 12″	CH_2	68.9–70.3
	8″, 9″, 14″	CH_2	68.3–70.3
	15″	CH_2	43.4
NOTA	Bn	C_6H_4	122.7,129.1,133.9,137.7
	Bn4a	CH_2	33.4
	N2	CH	58.6
	N3	CH_2	52.4
	N	CH_2	42.9,44.5,50.8,51.5,53.2,54.2,54.2
	N	COOH	168.8, 171.6, 173.4

Table 2.4: ^{13}C NMR data of NOTA-PEG_4-$cRGD_2$ in DMSO-d6/TFA (upon gHSQC and gHMBC spectra ± 0.2 ppm)

Supporting Figures

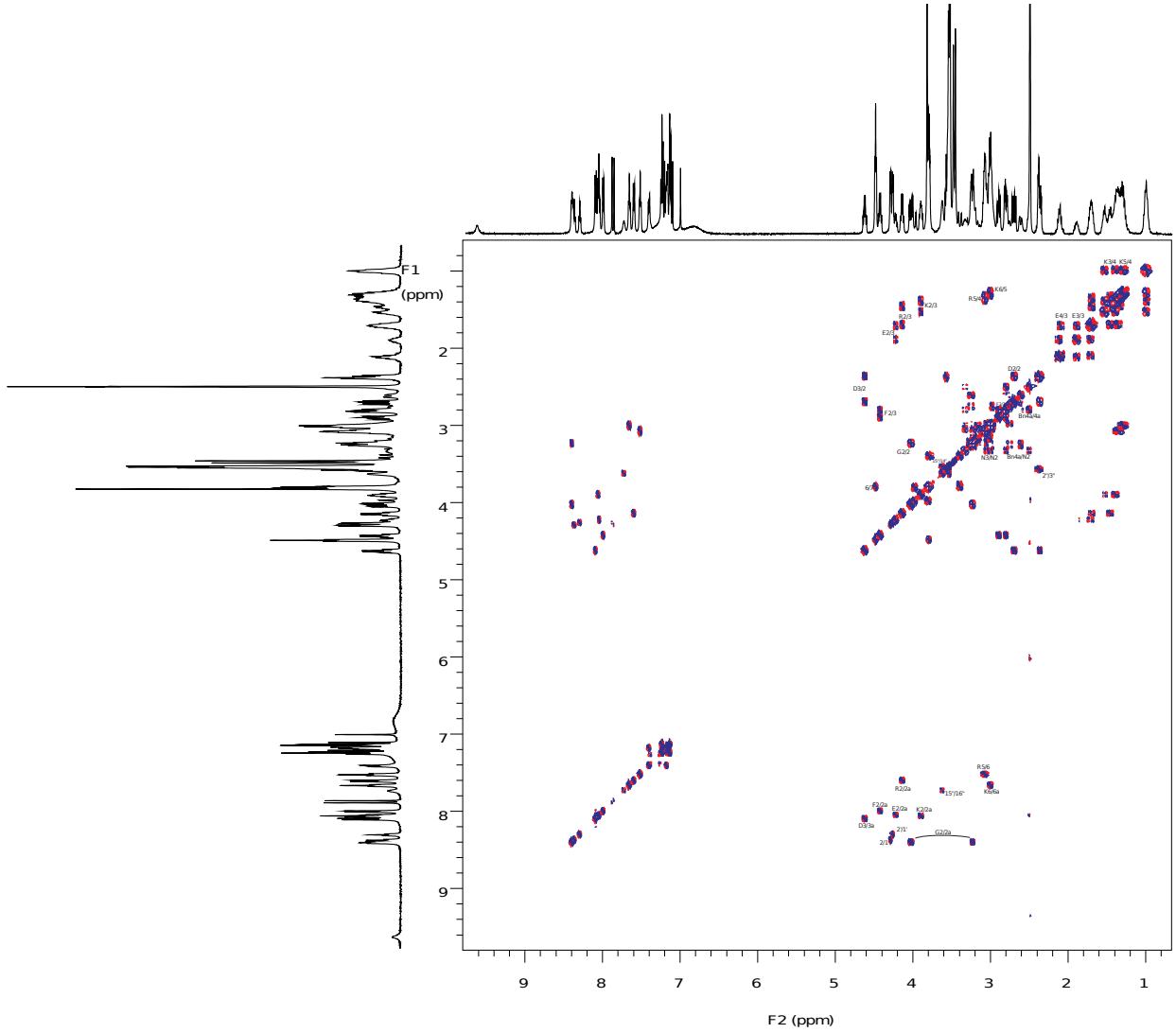

Figure 2.17: DQF-COSY spectrum of NOTA-PEG$_4$-cRGD$_2$ in DMSO-d6/TFA solution.

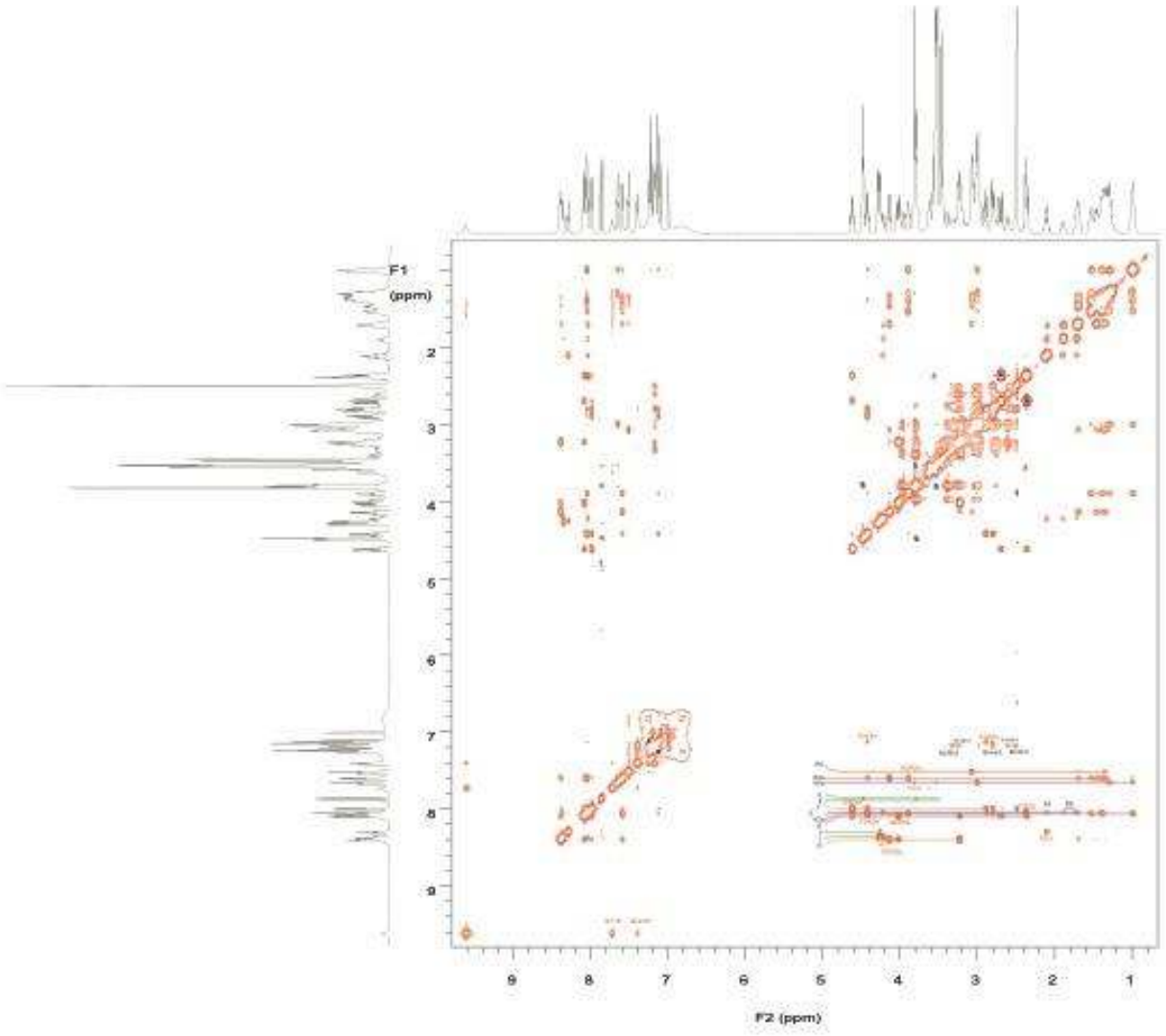

Figure 2.18: NOESY spectrum of NOTA-PEG_4-$cRGD_2$ in DMSO-d6/TFA solution.

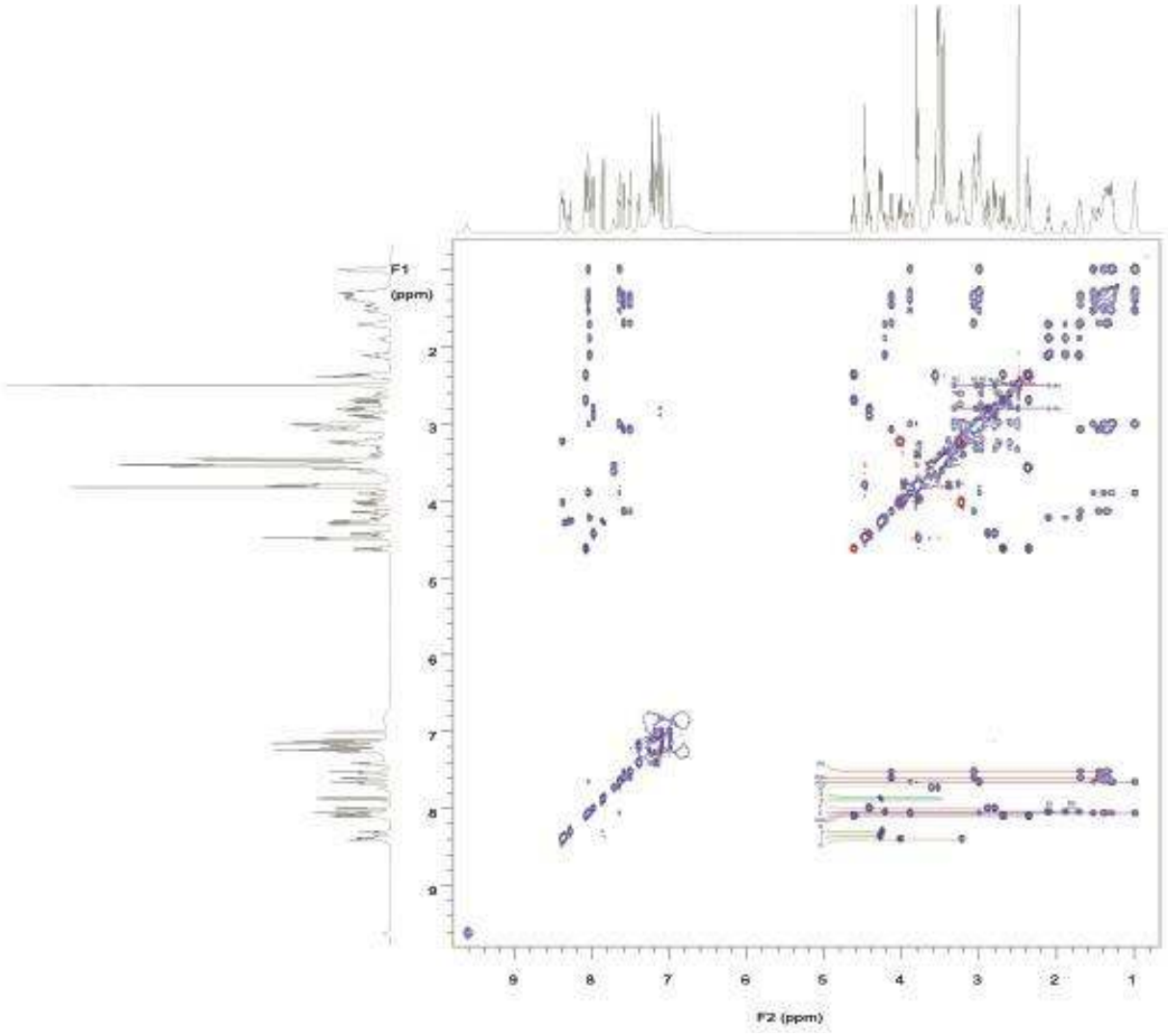

Figure 2.19: TOCSY spectrum of NOTA-PEG$_4$-cRGD$_2$ in DMSO-d6/TFA solution.

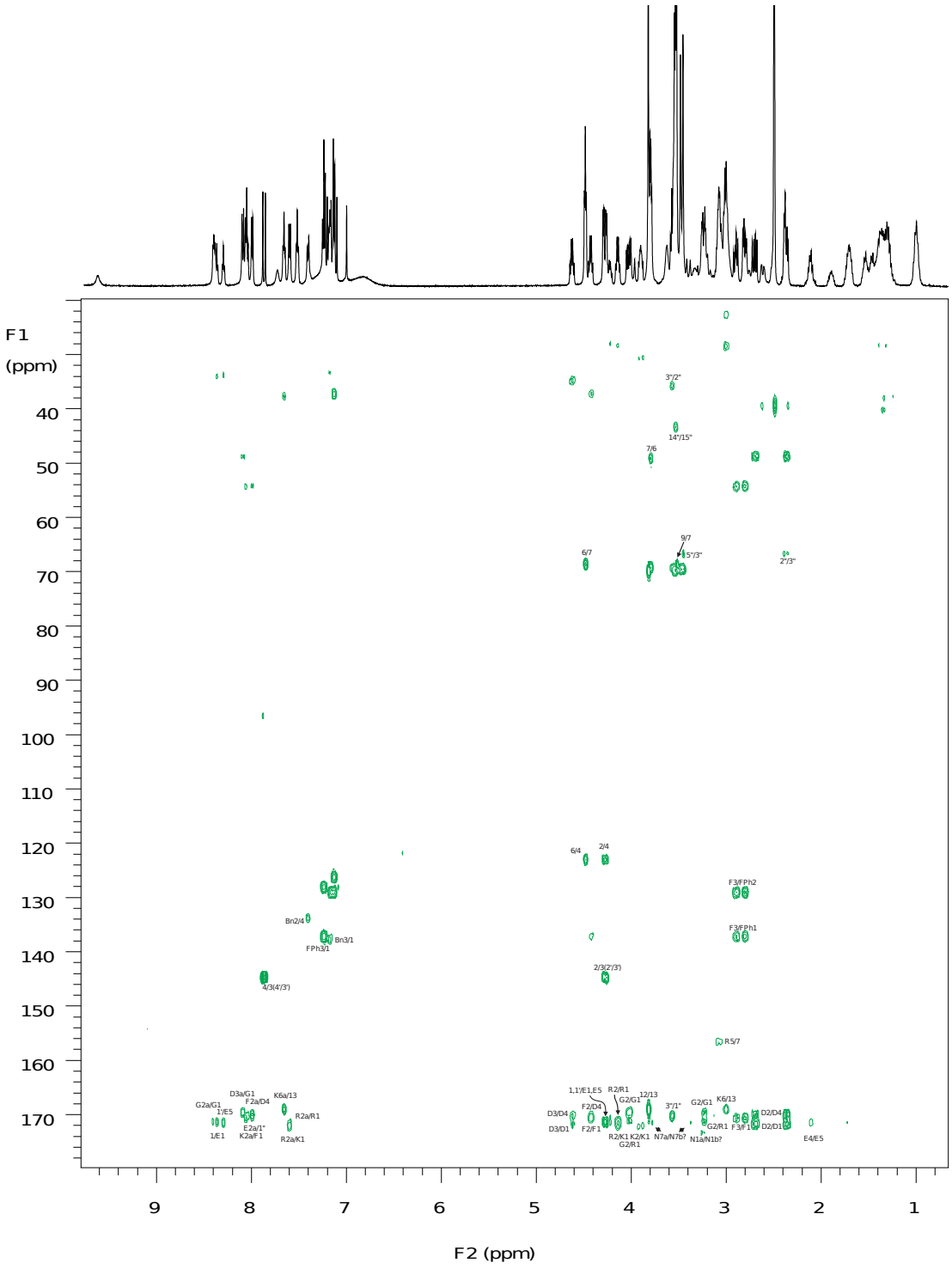

Figure 2.20: gHMBC spectrum of NOTA-PEG$_4$-cRGD$_2$ in DMSO-d6/TFA solution.

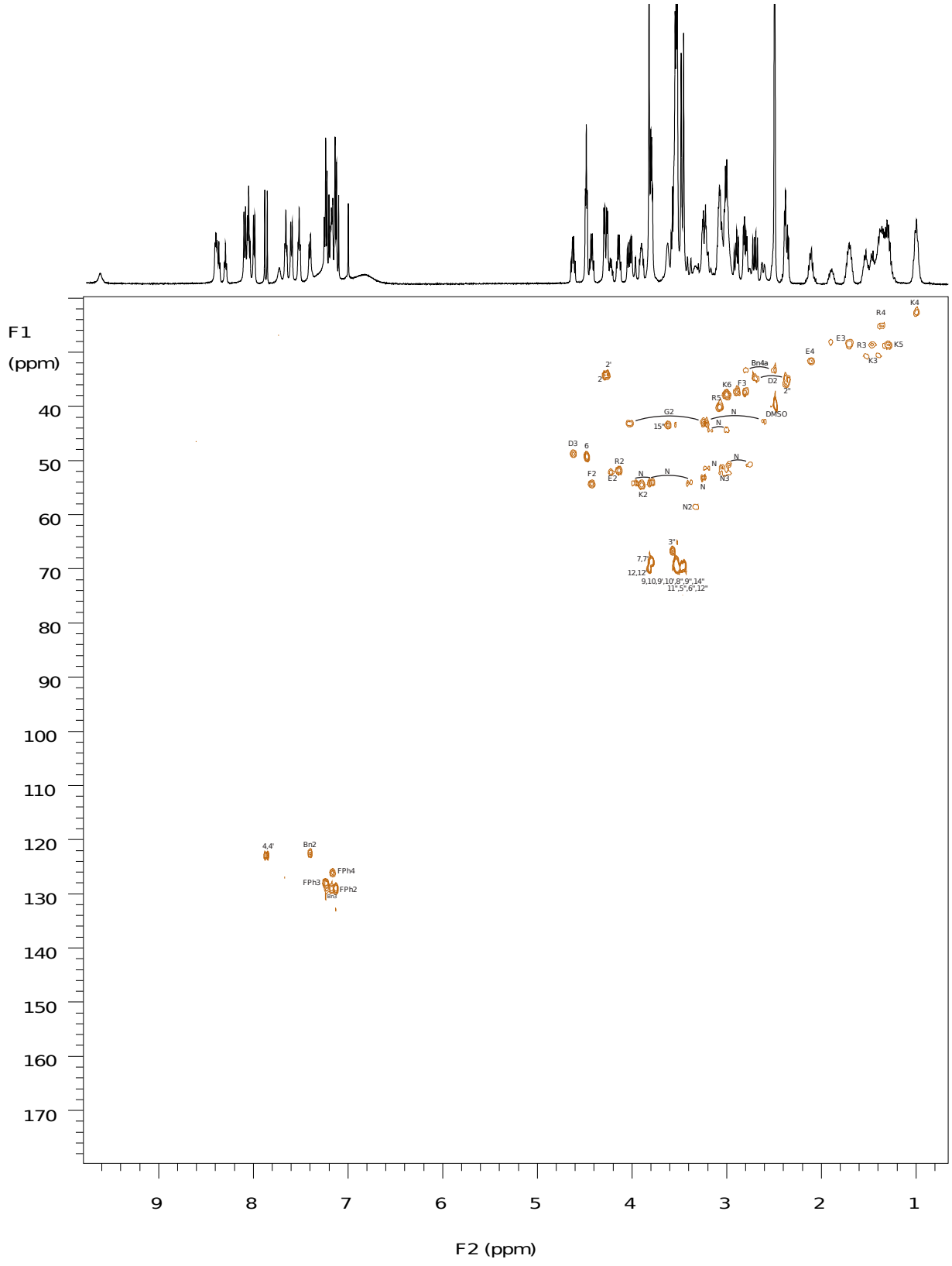

Figure 2.21: gHSQC spectrum of NOTA-PEG$_4$-cRGD$_2$ in DMSO-d6/TFA solution

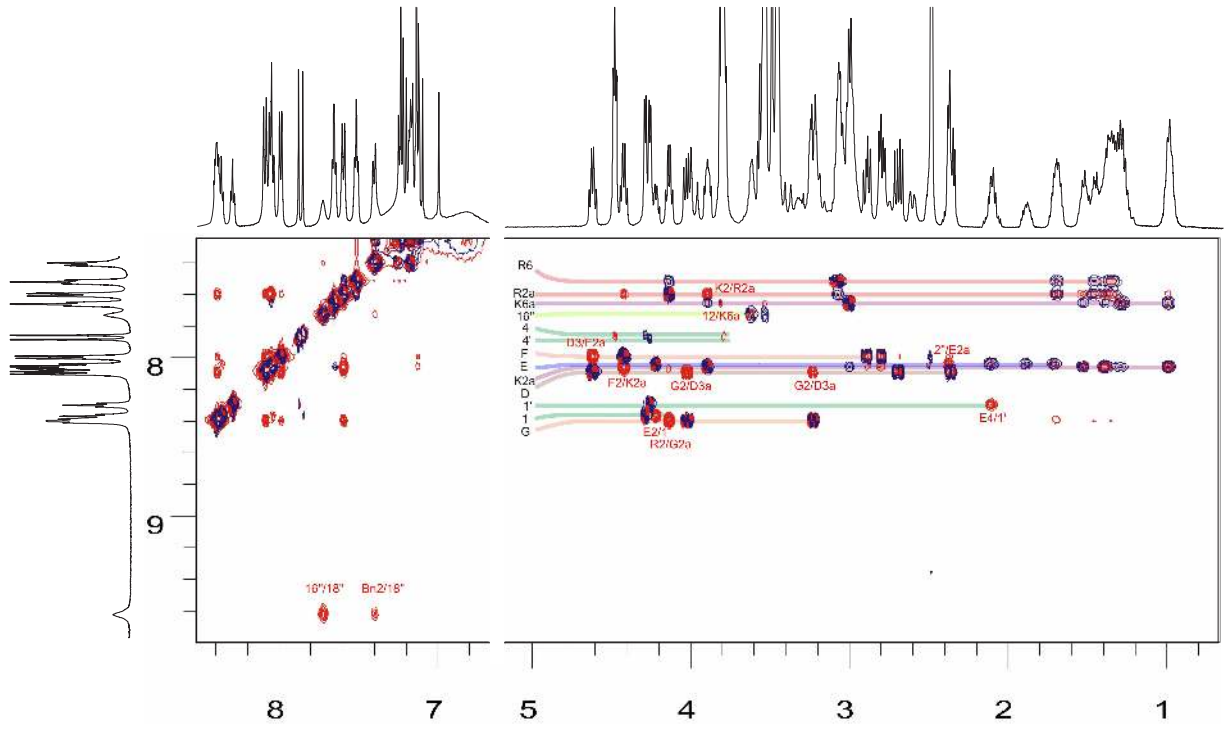

Figure 2.22: Superposition of TOCSY, DQF-COSY and NOESY NMR spectra of NOTA-PEG_4-cRGD_2 connectivities through amide protons.

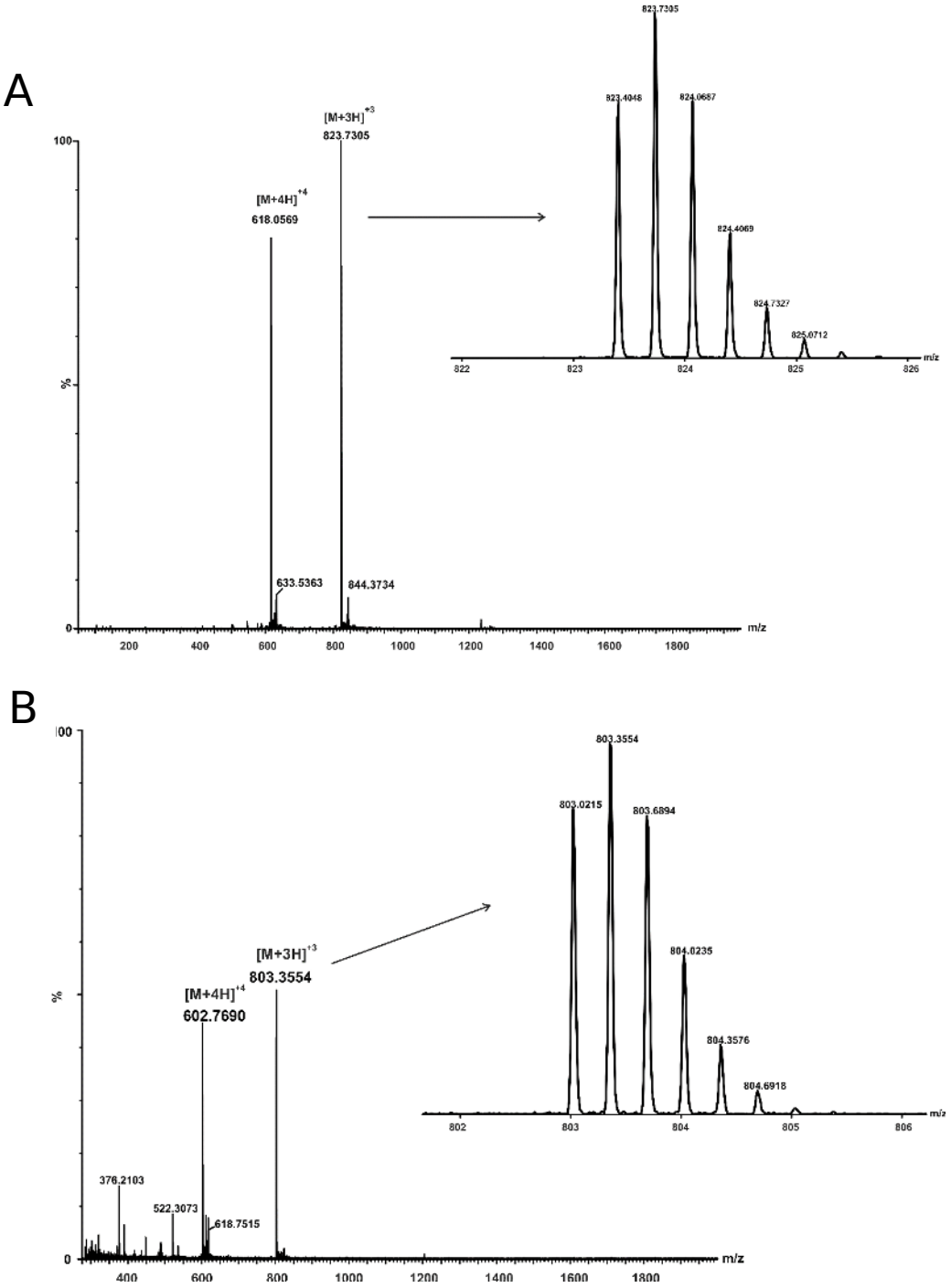

Figure 2.23: ESI mass spectra of (A) NOTA-PEG$_4$-cRGD$_2$ ([M+3H]$^{+3}$ m/z = 823.7305, [M+H]$^{+4}$ m/z=618.0569) zoom in on triply charged ion revealed monoisotopic signal m/z=823.4048; (B) FITC-PEG$_4$-cRGD$_2$ ([M+3H]$^{+3}$ m/z = 803.3554, [M+H]$^{+4}$ m/z=602.7690) zoom in on [M+3H]$^{+3}$ ion revealed triply charged monoisotopic signal m/z=823.4048

Chapter 3

Development and image-based characterization of preclinical model of PAD †

3.1 Introduction

Patients with diabetes mellitus (DM) in particular have been shown to have diminished capacity for neovascularization, which can lead to life-threatening complication in the heart and/or extremities, conditions known as coronary arterial disease (CAD) and peripheral arterial disease (PAD), respectively. So far, randomized clinical trials focused on the promotion of angiogenesis using local administration of growth factors like vascular endothelial growth factor (VEGF) or fibroblast growth factor (FGF) have shown no clear benefit in patients with CAD or PAD [25, 127, 128]. Careful interpretation of these results revealed that the unexpected failures could be attributed to a number of potential factors, including suboptimal delivery strategies, suboptimal duration of the therapy (which could lead to either insufficient growth of new vessels or excessive formation of nonfunctional vessels), and the myopic use of only a single growth factor at a time. Moreover, the evaluation of therapeutic angiogenesis in these trials was completed with relatively insensitive techniques focused on clinical endpoints like exercise tolerance, quality of life and survival, peripheral pressure measurements, and imaging of tissue perfusion.

More recently, focus within the scientific community has shifted towards the development of novel therapeutic strategies, such as genetic and stem cell-based approaches, as well as novel

†Work includes previously published material incorporating contributions from Hedhli Jamila, Slania Stephanie LL, Płoska, Agata, Czerwinski Andrzej, Konopka, Christian J, Wozniak Marcin, Banach, Maciej, Dobrucki Iwona T, Kalinowski Leszek, and Dobrucki, Lawrence W [1].

noninvasive imaging techniques to evaluate molecular events associated with angiogenesis [79,87,115,122,124,129]. It has been demonstrated that the extracellular matrix and integrins (including $\alpha_V\beta_3$ integrin a vitronectin receptor) are responsible for modulation of growth factor production in response to mechanical strain, and that they may play an integral role in the initiation of angiogenesis [64]. The physiological behavior of $\alpha_V\beta_3$, characterized by a very low expression in quiescent endothelium and upregulation in angiogenic cells, offer a tremendous advantage for the targeted imaging of angiogenesis. By imaging $\alpha_V\beta_3$ expression using radiolabeled probes, optimized for PET or SPECT, altered angiogenic activity may be diagnosed earlier and in a non-invasive manner, and the success of potential therapeutic strategies may be evaluated in almost real-time, which may lead to more individualized medical interventions and better patient outcomes.

Our group has previously evaluated a Technetium-99m labeled SPECT tracer (^{99m}Tc-NC100692, maraciclatide) [123] based on the arginine-glycine-aspartate (RGD) binding sequence for the imaging of $\alpha_V\beta_3$ integrin expression in various preclinical animal models of ischemia-induced angiogenesis [60]. This tracer, which showed a high $\alpha_V\beta_3$ affinity ($\sim$1 nM) and a rapid and efficient renal clearance route, was successfully used to evaluate peripheral angiogenesis in a murine model of hindlimb ischemia, and myocardial angiogenesis in both mice and rats [60]. Building on this and work of others, the field has seen renewed interest in developing chemically modified cRGD-based tracers with the hope of optimizing their pharmacokinetics, biodistribution, and target affinity and specificity [93]. These efforts resulted in the development of several multimeric tracers, which are particularly useful in areas with multivalent binding sites and clusters of integrins [5, 70, 88, 89, 130].

A probe by itself, however, is not enough; a suitable animal model is also necessary for preclinical work aimed at diagnosing and treating PAD. Although there exist a number of methods for surgically inducing peripheral ischemia, and streptozotocin treatment remains a preferred method for inducing diabetes, to my knowledge there is no systematic study aimed at developing an optimal protocol for studying diabetes-associated PAD in mice.

The goal of this investigation comes in two parts: first, determine an optimal animal model; and second, evaluate the efficacy of a novel multimeric cRGD tracer targeted at $\alpha_V\beta_3$ for the non-invasive PET imaging of peripheral angiogenesis in the onset of diabetes. The tracer was carefully characterized and used previously to evaluate myocardial angiogenesis in rats [5]. In the present study I demonstrate the feasibility of the probe for assessing angiogenesis in diabetic mice subjected to hindlimb ischemia. The imaging tracer was used to assess both temporal and spatial changes in local $\alpha_V\beta_3$ integrin expression in diabetic and non-diabetic animals subjected to surgical ligation of the right femoral artery in order to induce an angiogenic response. I detected a significant reduction in the $\alpha_V\beta_3$ activation in DM mice when compared to non-DM control mice. *En route* to this result, I established a number of other important findings relevant to both the murine model and the applicability of the probe for quantitatively assessing angiogenesis in diabetic mice. First, I show that the mouse model recapitulates several key markers of diabetes, including hyperglycemia, and enhanced GSP and HbA1c levels. Second, I demonstrate that a fluorescent analogue of the probe shows comparable specificity for $\alpha_V\beta_3$ an anti-$\alpha_V\beta_3$ antibody (LM609) when incubated under both normal and high glucose conditions. Third, I establish an optimal imaging protocol that allows for highly-detailed images. And finally, I validate the analysis of the PET-CT images and show a strong agreement with gamma well counting experiments on excised tissues, indicating that the probe can be used to accurately monitor $\alpha_V\beta_3$ expression in a non-invasive manner.

3.2 Methods

3.2.1 Diabetic Animal Model

All experiments were completed with the approval of the Institutional Animal Care and Use Committee of the University of Illinois at Urbana-Champaign, following the principles outlined by the American Physiological Society on research animal use.

Glycated Serum Protein and Glycated Hemoglobin A1c Male C57BL/6 mice (Jackson Laboratories) were used for all surgical and imaging interventions. A subset of mice (n=11) underwent streptozotocin (STZ, Sigma-Aldrich, USA) treatment to induce type-1 diabetes mellitus (DM). STZ was administered via intraperitoneal injection at a dose of 40 mg/kg for 5 days. Glucosuria and fasting glycemia ($> 200mg/dL$) two weeks after the first STZ treatment marked the success of DM induction. Diabetic (6 weeks after STZ treatment, n=11) and non-diabetic controls (n=4) were anesthetized with 1%-3% isofluorane vaporized in O_2 at a rate of 1 L/min via nose cone. Glycated serum protein (GSP) represents a measure of short-to-medium term glucose control. GSP was measured colorimetrically in the serum of blood collected from DM (2 and 6 weeks after streptozotocin administration) and non-DM mice using an enzymatic assay (Diazyme, USA). Briefly, blood was collected in a covered Eppendorf tube from the jugular vein of the animal and allowed to clot by leaving it undisturbed at room temperature. Clots were removed by centrifugation at 1,000-2,000 $\times$ g for 10 minutes in a refrigerated centrifuge. The resulting supernatant (serum) was used to measure GSP levels which were expressed in μmol/L.

Glycated hemoglobin A1c (HbA1c) is an important indicator of long-term diabetic control. HbA1c was measured in whole blood collected from DM (at 2 and 6 weeks) and non-DM mice using a direct enzymatic assay (Diazyme, USA). The HbA1c concentration was expressed directly as %HbA1c by use of a calibration curve.

Surgical Procedures All animals underwent hindlimb occlusion of the right femoral artery and a sham operation on the left hindlimb, following previously-described procedures [123]. Briefly, a small incision was made on the right leg to expose the femoral vasculature, and dual ligation of the femoral artery was performed distal to the profundus branch to induce unilateral hindlimb ischemia. All mice were allowed to recover for 7 days after surgery.

Ischemia Validation To validate the animal model, an additional group of normoglycemic mice (C57BL/6, n=3), was used to verify the occlusion and the reduction of blood flow in

ischemic hindlimb. Animals were imaged with laser doppler flowmetry Imager (moorLDI, Moor Instruments, UK) before, immediately after, and 1 week post-surgery. To confirm the presence of collateral vessels as a result of angiogenic and arteriogenic processes, Microfil (Flowtech Inc, USA) casting followed by the tissue clearing technique was performed on the same mice 4 weeks post-surgery using a procedure described previously [131].

Biodistribution One week after occlusion, 5 groups of animals were injected with 6.81 $\pm$ 0.536 MBq of ^{64}Cu-NOTA-PEG$_4$-cRGD$_2$ via the jugular vein and at various time points (30min n=3, 1hr n=3, 2hr n=3, 4hr n=3, and 24hr n=2), different organs were excised and subjected to gamma well counting. The mass and radioactivity of tissue sections were assessed with a Voyager Pro. (Ohaus, USA) and Wizard2 gamma well counter (PerkinElmer, USA) respectively. The ^{64}Cu signal was then corrected to account for background radioactivity, radioactive decay of the samples, and tissue weight.

3.2.2 In Vitro Binding Specificity

To validate the specificity of FITC-PEG$_4$-cRGD$_2$ to the $\alpha_V\beta_3$ integrin receptor, human umbilical vein endothelial cells (HUVECs) were first cultured on coverslips until confluent, before being fixed using a 4% solution of paraformaldehyde for paired-staining with both FITC-PEG$_4$-cRGD$_2$ (approximately 1 μM) and PE-labeled $\alpha_V\beta_3$ antibody LM609 (1:100, R&D Systems, USA). The cells on the coverslips were washed with buffer before and after each independent hour-long room temperature incubation, and the coverslips were ultimately mounted to microscope slides using DAPI Fluoromount (Southern Biotech). An Axiovert 200M inverted fluorescence microscope (Zeiss, USA) was then used for imaging (employing the 10x and 20x objectives). Finally, the images were analyzed using the ZEN 2012 software package (Zeiss, USA).

Because diabetes is characterized by high blood glucose levels, which could potentially modify the structure of $\alpha_V\beta_3$ via glycosylation and alter ligand-receptor interactions, I

performed additional experiments to assess cellular binding of PEG_4-$cRGD_2$ under high-glucose conditions. HUVECs were cultured in high-glucose (14 mM) growth media for 24 hours before incubation with FITC-PEG_4-$cRGD_2$ (0-1 μM) at 4°C for 2 hours. A control group was cultured in normoglycemic (5.5mM) growth media followed by incubation with FITC-PEG_4-$cRGD_2$. Binding of FITC-PEG_4-$cRGD_2$ to $\alpha_V\beta_3$ integrin was assessed using flow cytometry (LSR II Flow Cytometry Analyzer, BD Biosciences, USA).

3.2.3 In Vivo Imaging of PAD Associated Angiogenesis

One week after occlusion, DM and non-DM mice (n=15) were injected with 6.81 ± 0.536 MBq of ^{64}Cu-NOTA-PEG_4-$cRGD_2$ via the jugular vein and 60 minutes later *in vivo* microPET-CT imaging was performed using a small animal dedicated Inveon system (Siemens Healthcare USA). An additional group of non-diabetic mice (n=4) was injected with 7.21 ± 2.31 MBq of ^{64}Cu-acetate to study differential organ biodistribution of ^{64}Cu-NOTA-PEG_4-$cRGD_2$. Animals were placed on a polyacrylic bed in the supine position with legs secured in an extended position. Mice underwent X-ray microCT imaging (80kVp, 500μA, 100μm spatial resolution) followed by 15 min microPET imaging (15% energy window centered at 511 keV). All mice were euthanized immediately after last imaging session was completed and tissue samples were taken for gamma well counting and snap-frozen in liquid nitrogen for immunofluorescence analysis.

Image Analysis The microPET and microCT images were reconstructed using the OSEM/3D algorithm (Siemens Healthcare USA) and the cone-beam technique (Cobra Exim), respectively. MicroPET images were fused with microCT images and quantified using a semiautomated approach developed and evaluated previously [132]. Briefly, complex irregular volumes of interest (VOIs) were generated from the microCT images the proximal region was selected above the knee and near the ligation site where as the distal area was below the knee. The VOI's were applied on the co-registered microPET images to calculate absolute ^{64}Cu

activities using the Inveon Research Workplace (Siemens Healthcare USA). These complex VOIs included only soft tissue (skeletal muscles) after the removal of bone structures during the image segmentation process. To validate the accuracy of the quantitative targeted imaging approach, image-derived results were compared with the gamma well counting analysis of the corresponding tissue samples.

3.2.4 Postmortem Analysis

Gamma Well Counting Skeletal muscles from both the ischemic and non-ischemic hindlimbs were excised and separated into distal and proximal sections based on the location of the ligature in the ischemic limb and anatomical landmarks in the non-ischemic limb. The mass and radioactivity of tissue sections were assessed with a Voyager Pro. (Ohaus, USA) and Wizard2 gamma well counter (PerkinElmer, USA) respectively. The ^{64}Cu signal was then corrected to account for background radioactivity, radioactive decay of the samples, and tissue weight.

Histology and Immunofluorescence Ischemic and non-ischemic hindlimb sections collected from diabetic and non-diabetic animals were embedded in the Optimal Cutting Temperature (OCT) compound. The embedded tissue sections were then snap frozen in liquid nitrogen and cut into 5μm sections using a cryotome. The cut sections were then fixed in ice-cold acetone and stained with either a Cy-5 fluorescent endothelial cell marker (CD31, EMD Millipore, USA), FITC-PEG$_4$-cRGD$_2$ (1μM), and inflammatory markers APC-CD14 (Santa Cruz Biology,USA), and PE-CD74 (R&D, USA). The stained sections were then relocated to an incubator and allowed to incubate overnight. After incubation, the stained sections were mounted using DAPI fluoromount (Southern Biotech, USA) and images were acquired using a fluorescent microscope (Zeiss Axiovert 200M) at both 10x and 20x objectives. For processing, the acquired images were assessed using Zeiss Zen Blue software for the total area positively stained in several randomly chosen (200 $\times$) fields. This software was validated

in a previous study conducted by our group [123]. Acquired stained images of the sections were assessed for co-localization between the different fluorescent antibodies (PE-CD74, APC-CD14, and Cy-5-CD13) and the FITC-PEG_4-$cRGD_2$. Different antibody channels were separated and quantified using an ImageJ-plugin (Coloc2) to obtain the Pearson's correlation coefficient. This assessment was repeated for each of the images randomly chosen for percent positive area quantification.

3.2.5 Statistical Analysis

The Student t test was used to compare 2 groups DM vs non-DM. One-way ANOVA was used to compare multiple parameters. A value of $P < 0.05$ was considered significant.

3.3 Results

3.3.1 Radiochemical purity and stability of the cRGD probes

The radiochemical purity of ^{64}Cu-NOTA-PEG_4-$cRGD_2$, determined in both pH 7.4 PBS and blood plasma using C-18 RP-HPLC, was $> 95\%$ up to 24 hrs after labeling [5]. The probe's fluorescent analogue, FITC-PEG_4-$cRGD_2$, demonstrated similarly high stability in both media (data not shown).

3.3.2 Animal model of peripheral angiogenesis in diabetes

Changes in blood biomarkers between 2 and 6 weeks after DM induction DM was introduced in a subset of mice through streptozotocin (STZ) treatment. After induction, I measured three key DM biomarkers: circulating blood glucose, GSP, and HbA1c blood levels. I detected a change in all three markers as early as two weeks after STZ administration. While I found no significant change in glucose level between weeks 2 and 6, I saw a significant surge in GSP and HbA1c levels (3 and 1.3-fold, respectively, see Figure 3.1). These results indicate

that many important diabetes-associated physiological changes can take up to 6 weeks to manifest in the murine model, and as such, I opted to conduct the *in vivo* experiments 6 weeks after STZ treatment.

Validation of the animal model of peripheral ischemia The right femoral arteries of the animals were surgically ligated in order to model peripheral vascular occlusion. This resulted in distal ischemia followed by the initiation of both the angiogenic and arteriogenic processes. Microfil casting and tissue clearing techniques were used in a subset of animals to visualize the location of the occlusion and the predicted ischemic area in relation to other anatomical structures (see Figure 3.2). To verify the completeness of the surgical ligations, I performed Laser Doppler imaging of peripheral perfusion. Immediately after the surgery I observed dramatic reduction ($> 80\%$) in blood perfusion within the ischemic hindlimb, which was partially recovered at 1 week after the ligation (see Figure 3.2). Based on this observation, and results published previously [5], I used the 1 week time point to study the differences in peripheral angiogenesis in the DM and non-DM mice.

3.3.3 Properties Of FITC-PEG$_4$-cRGD$_2$–$\alpha_V\beta_3$ binding In a high-glucose microenviroment

The specificity of the probe was assessed by co-incubating FITC-PEG$_4$-cRGD$_2$ and the commercially available phycoerythrin-labeled $\alpha_V\beta_3$ antibody, PE-LM609. For these experiments I used human umbilical vein endothelial cells (HUVECs), which are known to constitutively express $\alpha_V\beta_3$. As shown in Figure 3.3 there is a strong colocalization between the fluorescein and phycoerythrin signals. This is in accordance with the previously published studies showing a high correlation between FITC-PEG$_4$-cRGD$_2$ and PE-LM609 fluorescence using single cell flow cytometry [5].

Of particular importance to imaging $\alpha_V\beta_3$ expression in DM patients is to determine whether a high-glucose environment can affect the $\alpha_V\beta_3$ receptor's binding properties. To

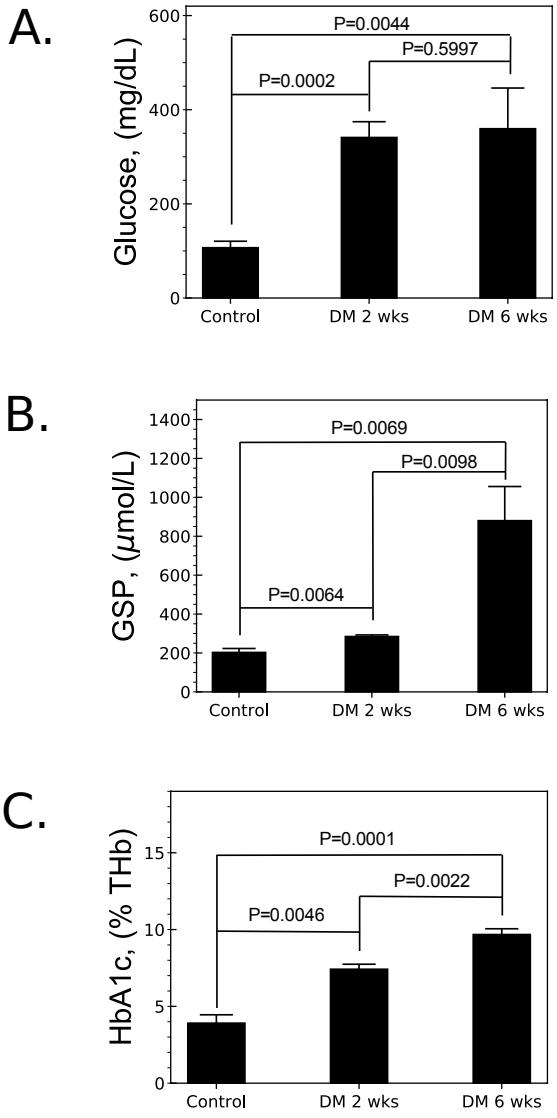

Figure 3.1: Characterization of diabetes-associated blood markers. (A) Glucose level was found to rise as soon as 2 weeks after induction of diabetes, but no further increase was found at the 6 week time point. (B) Glycated serum protein (GSP) showed an increase at 2 weeks, and surged dramatically by week 6. (C) Glycated hemoglobin A1c (HbA1c) increased consistently over the 6 week time frame.

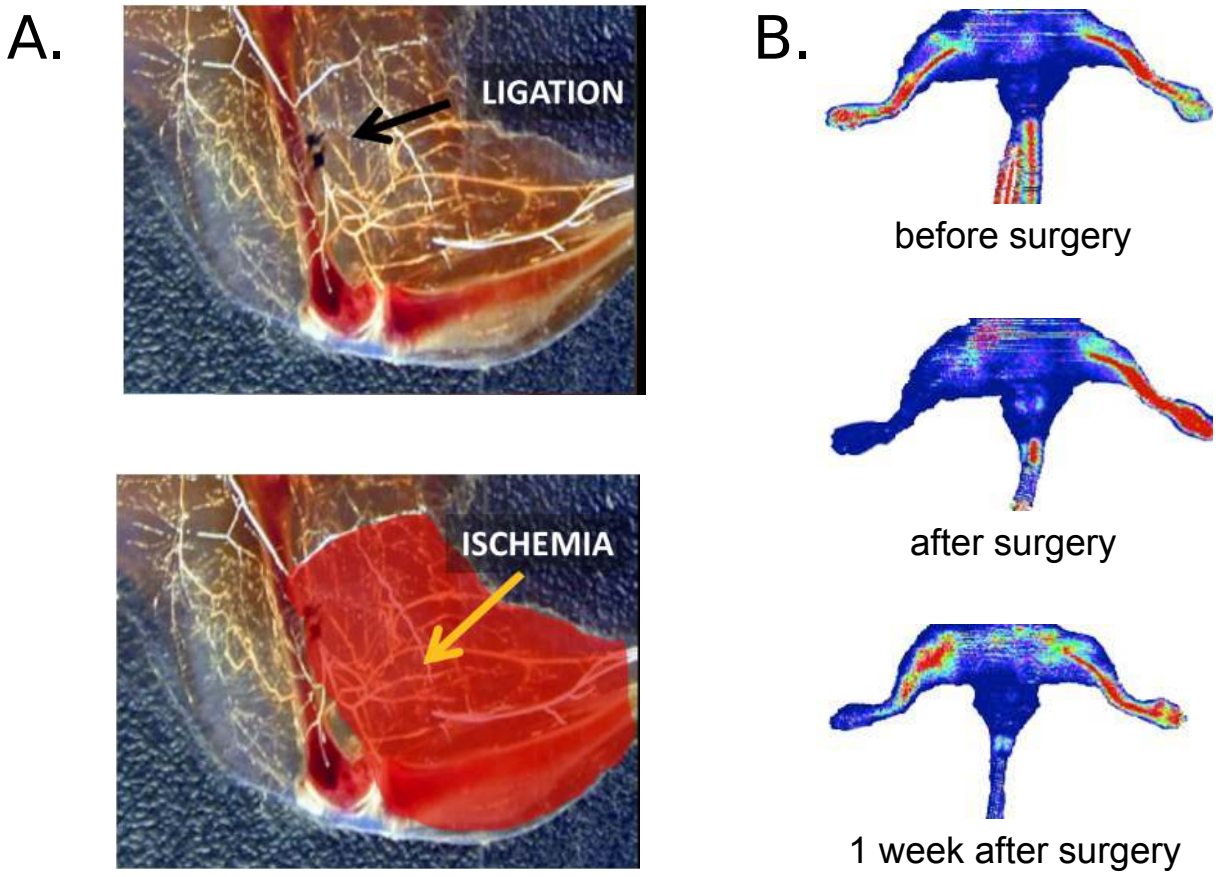

Figure 3.2: Surgical model of murine hindlimb ischemia. (A) Animals underwent surgical occlusion of the right femoral artery by placing two ligatures distal to profundus branch inducing unilateral hindlimb ischemia (bottom, yellow arrow). Placement of ligatures (top,black arrow) and vascular occlusion was visualized with the Microfil casting and tissue clearing technique. (B) The surgery resulted in an immediate decrease in perfusion in ischemic hindlimb with a partial recovery at 1 week after the surgery, as assessed using Laser Doppler flowmetry.

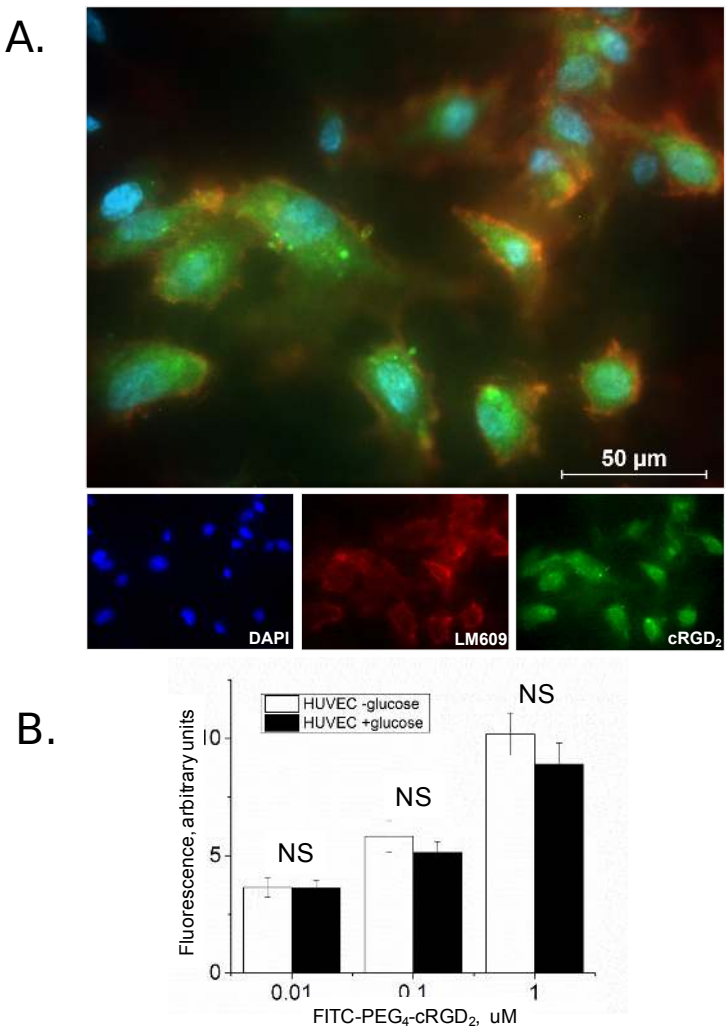

Figure 3.3: Colocalization of FITC-PEG_4-$cRGD_2$ and LM609 to human umbilical vein endothelial cells (HUVECs) expressing $\alpha_V\beta_3$ integrin. (A) Incubation of HUVECs with 1 μM FITC-PEG_4-$cRGD_2$ (green) and phycoerythrin-conjugated LM609 (1:100, red). The high degree of overlap indicates specific binding of the probe to $\alpha_V\beta_3$. (B) HUVECs incubated for 24 hrs in low-glucose (5.5mM) or high-glucose (14mM) medium did not result in any significant differences in FITC-PEG_4-$cRGD_2$ uptake, as assessed by flow cytometry.

exclude this possibility, I incubated HUVECs with the FITC-PEG_4-$cRGD_2$ in growth media supplemented with 14 mM glucose. Comparison with a control HUVECs cultured in normal growth media showed no significant difference in FITC-PEG_4-$cRGD_2$ uptake under elevated glucose conditions (see Figure 3.3). This observation indicates that any differences in the uptake of the imaging probe that arise between diabetic and non-diabetic animals is likely due to changes in $\alpha_V\beta_3$ integrin expression/activation levels and not glycation-associated modification of the vitronectin receptor.

3.3.4 Pharmacokinetics and biodistribution

To demonstrate that the radiotracer exhibits favorable organ retention for the purpose of imaging peripheral angiogenesis, I performed comparative biodistribution studies using both targeted ^{64}Cu-NOTA-PEG_4-$cRGD_2$ and the non-targeted ^{64}Cu-acetate as control. Figure 3.4 shows the difference in the biodistribution profiles of both radiotracers. As expected, non-targeted ^{64}Cu-acetate demonstrated increased uptake in all organs (including blood) with a very high uptake ($> 20\%I.D./g$) in the liver, gallbladder, kidneys, and intestines due to non-specific affinity to tissue proteins. In contrast, ^{64}Cu-NOTA-PEG_4-$cRGD_2$ uptake was significant in the gallbladder, kidney cortex and intestines. In addition, PET imaging revealed that ^{64}Cu-NOTA-PEG_4-$cRGD_2$ cleared rapidly from the blood (contributing to an overall low background) and was excreted predominantly by kidney filtration.

We performed additional biodistribution studies of ^{64}Cu-NOTA-PEG_4-$cRGD_2$ at a series of time points (30 min, 1 hr, 2hr, 4h and 24hr after injection) to evaluate the clearance of the probe and establish the optimal post-injection timing for a PET-CT scan (see Figure 3.5). I found that PET imaging at 1-2 hours post injection resulted in the optimal blood clearance and uptake within the ischemic muscle.

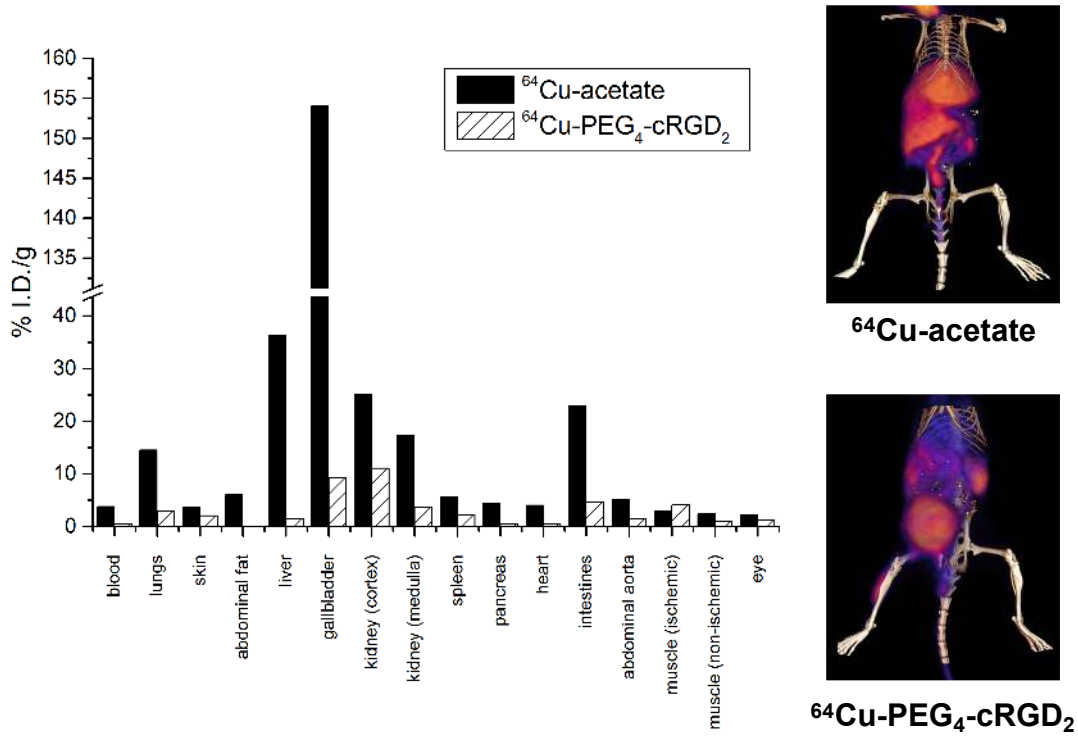

Figure 3.4: Organ-specific uptake (right, assessed using PET-CT) and biodistribution (left, assessed using gamma well counting) of ^{64}Cu-NOTA-PEG$_4$-cRGD$_2$ and the non-targeted ^{64}Cu-acetate one hour after jugular vein injection demonstrates a favorable biodistribution and optimal retention for targeted *in vivo* imaging of peripheral angiogenesis.

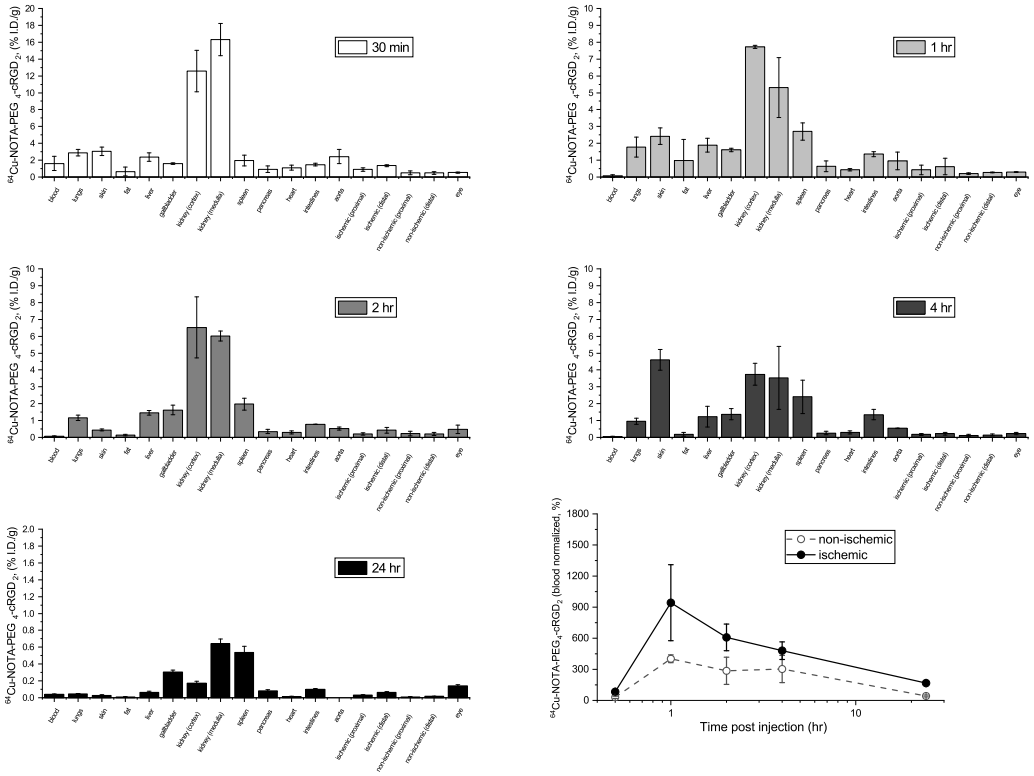

Figure 3.5: Biodistribution of ^{64}Cu-NOTA-PEG$_4$-cRGD$_2$ at various time points after injection. At the 30 min time point, the probe was mainly in the bloodstream, while the one and two hour time points showed the greatest accumulation in the distal ischemic tissue. Later time points showed little accumulation in the ischemic limb, and largely resembled the non-ischemic tissue. These results indicate the optimal time point for imaging is between one and two hours after administration of the tracer.

3.3.5 PET-CT imaging analysis versus gamma well counting

Representative PET-CT images of peripheral angiogenesis acquired 1 week after surgical ligation are shown in Figure 4.7. Confirmed by biodistribution studies, PET-CT images obtained 1 hr after intravenous injection of the radiotracer were of excellent quality and demonstrated "hot spots"—of increased ^{64}Cu-NOTA-PEG$_4$-cRGD$_2$ uptake within the ischemic hindlimb—whereas the non-ischemic muscle showed no significant uptake. Moreover, VOI-based image analysis of PET-CT images (see Figure 4.7) correlated well (R^2=0.9602) with postmortem ^{64}Cu-NOTA-PEG$_4$-cRGD$_2$ activities in the hindlimb muscle sections measured using gamma well counting immediately after PET-CT imaging (see Figure 4.7).

3.3.6 Diabetes-associated reductions in $\alpha_V\beta_3$ can be monitored non-invasively using ^{64}Cu-NOTA-PEG$_4$-cRGD$_2$

Most importantly, I found a significant ($P < 0.05$) reduction of ^{64}Cu-NOTA-PEG$_4$-cRGD$_2$ uptake in all muscle segments (distal and proximal) of diabetic animals when compared to the non-diabetic control segments (see Figure 3.7). Quantitative analysis of PET-CT images confirmed this result, indicating that DM mice had significantly lower %I.D./g in their distal ischemic tissue than non-diabetic mice. PET imaging showed a significant increase in the retention of ^{64}Cu-NOTA-PEG$_4$-cRGD$_2$ in the ischemic (relative to non-ischemic) hindlimbs, which demonstrates the probe's specificity to areas of active angiogenesis and $\alpha_V\beta_3$ expression. Together, these findings indicate that molecular imaging with ^{64}Cu-NOTA-PEG$_4$-cRGD$_2$ is suitable to quantitatively asses different angiogenic responses in DM and non-DM environments.

In order to investigate the physiological effects that are associated with $\alpha_V\beta_3$ expression in both DM and non-DM mice, I evaluated tissue samples collected from all animals. Both ischemic and non-ischemic distal hindlimb muscle sections were stained with FITC-PEG$_4$-cRGD$_2$, Cy-5 labeled endothelial cell marker (CD31), CD14 (a marker mostly associated with

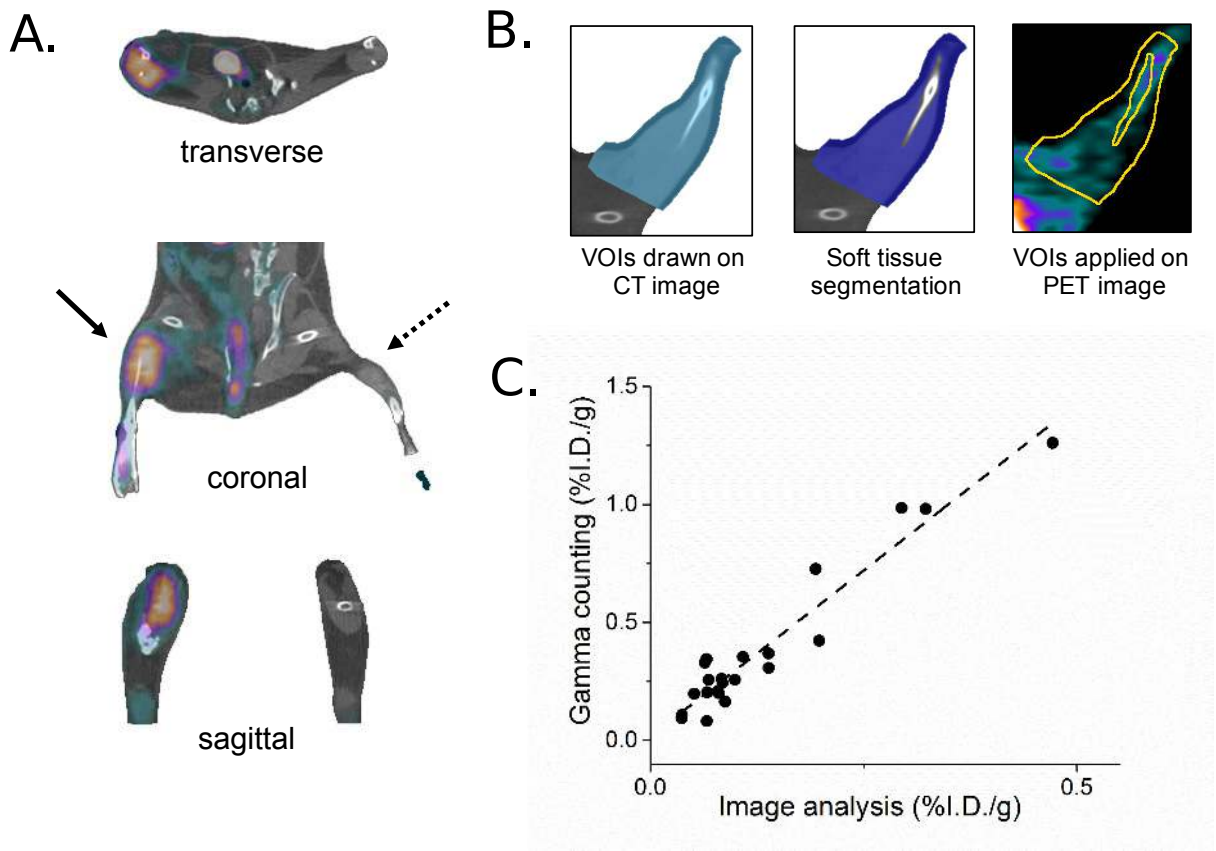

Figure 3.6: PET-CT imaging analysis. (A) Representative *in vivo* PET-CT images of peripheral angiogenesis 1 week after surgical ligation of the right femoral artery. One hour after intravascular injection of ^{64}Cu-NOTA-PEG$_4$-cRGD$_2$ a significant uptake of the radiotracer ("hot spot") was observed in the ischemic hindlimb. (B) For the image analysis, volumes-of-interests (VOIs) were drawn on CT images of ischemic and non-ischemic hindlimbs (left) followed by segmentation of hindlimb muscles (middle). These irregular VOIs were placed on PET images to calculate the radiotracer's uptake (expressed in %I.D./g tissue, right). (C) Correlation between the two methods (PET-CT and gamma well counting) used to measure radiotracer uptake in mice hindlimbs showed a strong linear correlation ($R^2 = 0.9602$, solid line).

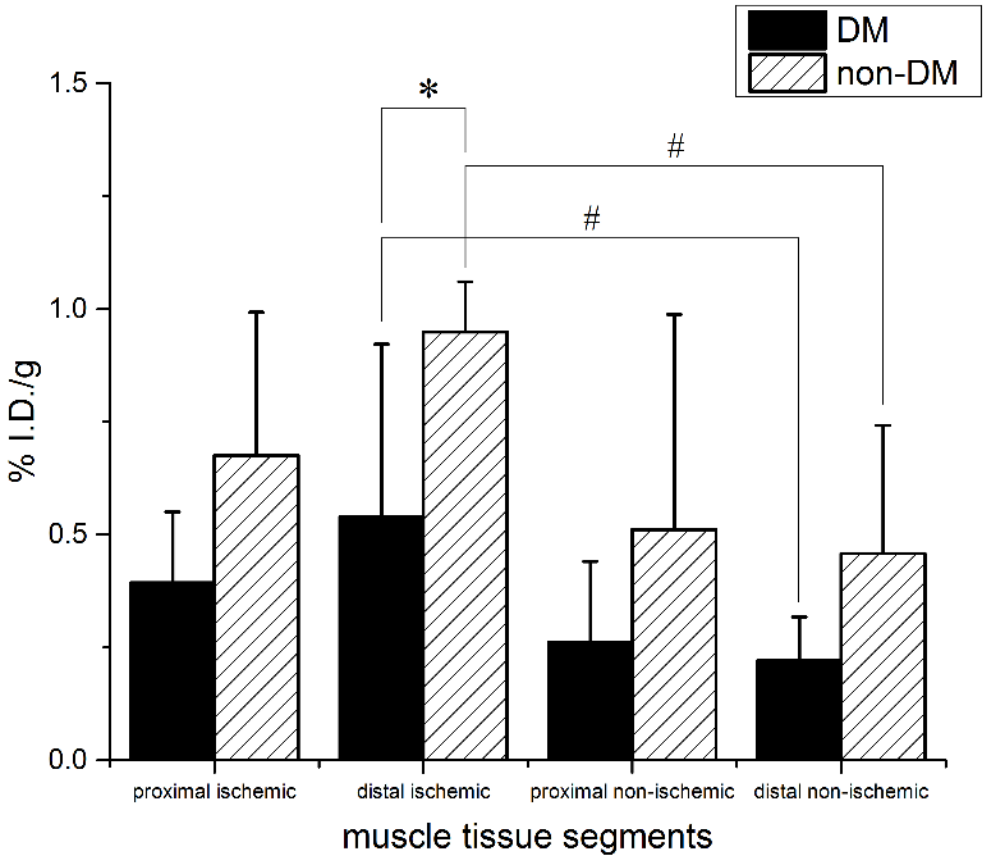

Figure 3.7: Analysis of ^{64}Cu-NOTA-PEG$_4$-cRGD$_2$ retention in the hindlimbs of DM and non-DM mice 1 week after surgical ligation of the right femoral artery. Overall there was a significant ($\#P < 0.05$) increase in ^{64}Cu-NOTA-PEG$_4$-cRGD$_2$ retention in the distal segments of the ischemic relative to the non-ischemic hindlimbs, as well as a significant ($*P < 0.05$) decrease in the distal ischemic hindlimb of DM mice compared to non-DM controls.

macrophages and dendritic cells), or CD74 (a cell surface receptor expressed by macrophages and endothelium cells which has been linked to reperfusion after vascular injury [133]). Representative immunofluorescence images taken from DM and non-DM mice are shown in Figure 3.8 A, B, C. I found CD31 positive endothelial cells within the capillaries and small arterioles of the non-diabetic ischemic hindlimb sections, which correlated with high $\alpha_V\beta_3$ expression. By comparison, the DM mice showed significant reduction in CD31 positive staining and FITC-PEG_4-$cRGD_2$ (3.5- and 3.8-fold respectively) in their ischemic muscle tissues, suggesting both a reduction in capillary density and decreased $\alpha_V\beta_3$ expression in DM animals relative to the non-DM controls. I found as well that DM mice showed a statistical significant reduction (3.2 and 4 fold) for both CD14 and CD74 respectively as shown in Figure 3.8 A, B. These results demonstrate the dynamic changes in the DM microenvironment. I performed additional histology studies to determine the extent of co-localization between the FITC-labeled probe and CD14 or CD74. The FITC-PEG_4-$cRGD_2$ showed a modest degree of co-localization (Pearson coefficient of 0.50) with the labeled CD14, but a much stronger correlation (Pearson coefficient of 0.71) with the labeled CD74 see Figure 3.8 D. This supports the idea that the probe is effectively targeting regions of active angiogenesis and vascular repair. As expected, the greatest degree of co-localization occurred with CD31 (correlation coefficient of 0.765), indicating that the probe targets endothelial cells much more strongly than macrophages, dendritic cells, or other cell types associated with the ischemic response. Finally, I also found that both CD14 and CD74 staining were significantly reduced in DM relative to non-DM ischemic tissues (by about 3.2 and 4.0 fold, respectively). This once again underscores the negative impact of DM on vascular regeneration.

3.4 Discussion

The study presented here focuses on finding an optimal animal model for the study of PAD and the feasibility of assessing diabetes-associated differences in peripheral angiogenesis using

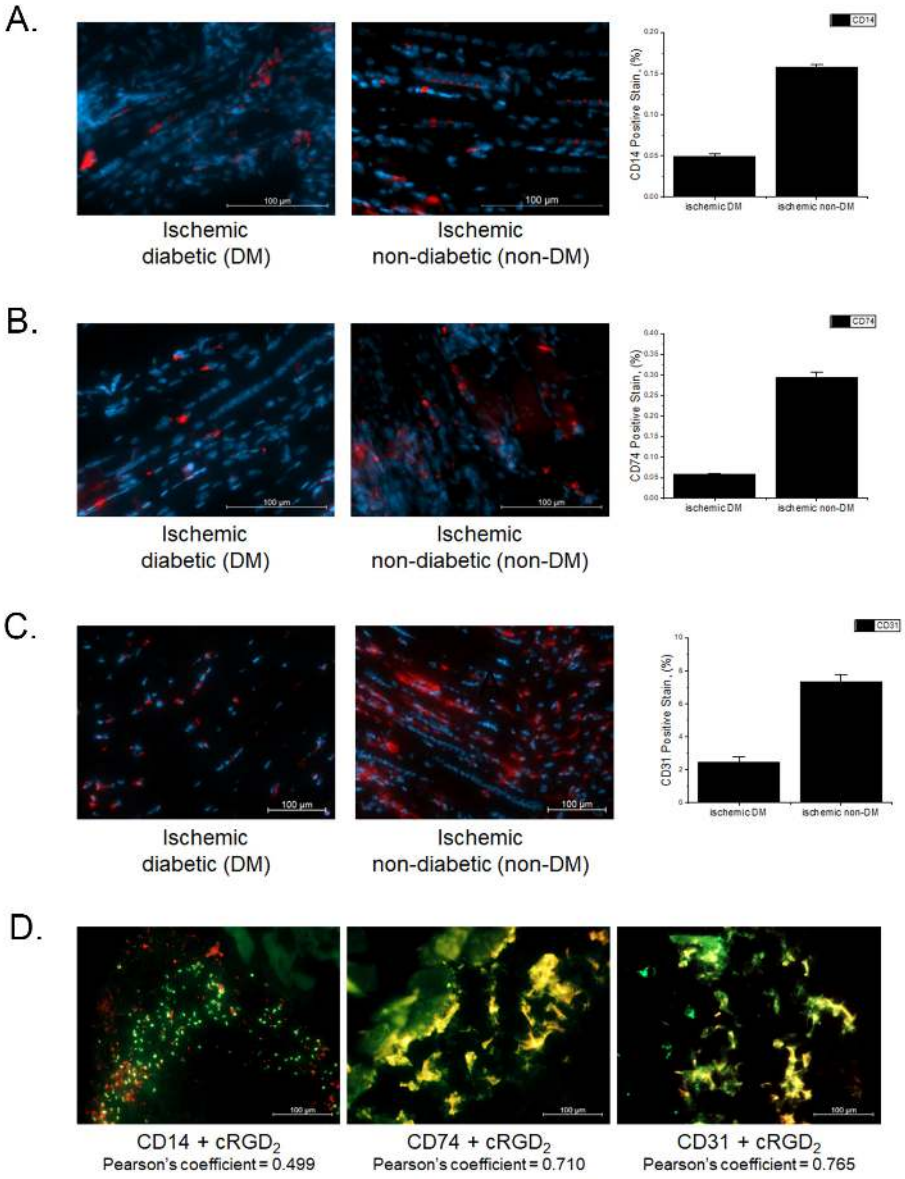

Figure 3.8: Representative cross sections taken from ischemic lower hindlimbs of both DM (left) and non-DM (right) mice 1 week after femoral occlusion. (A) Sections were stained with inflammation marker CD14 (red) and co-stained with DAPI (blue) to visualize nuclei. (B) Sections were stained with reperfusion marker CD74 (red) and co-stained with DAPI (blue) to visualize nuclei. (C) Sections were stained with endothelial marker CD31 (red) and co-stained with DAPI (blue) to visualize nuclei. (D) Sections were stained with CD14, or CD74, or CD31 (red) and fluorescent analogue FITC-PEG_4-$cRGD_2$. Fluorescence quantification showed a reduction in both capillary density (CD31 staining), inflammation (CD14), reperfusion (CD74), and FITC-PEG_4-$cRGD_2$ ($\alpha_V\beta_3$) retention in DM animals when compared with non-DM controls $*P < 0.05$. I found a strong correlation between CD31, CD74 and FITC-PEG_4-$cRGD_2$, and a modest degree of co-localization between CD14 and FITC-PEG_4-$cRGD_2$.

a ^{64}Cu labeled dimeric cyclic RGD-based PET-CT probe targeted at $\alpha_V\beta_3$. The design of the probe benefitted from years of prior results; it is characterized by high chemical stability, a favorable biodistribution, and a focal retention that results in an excellent quality of obtained images. ^{64}Cu was chosen as a PET imaging isotope due to its relatively easy chemistry, the availability of strong chelators capable of providing a firm backbone for the radioactive label, and the potential for clinical translation due to its relatively long half-life ($\sim$ 12.7 hours). Furthermore, a fluorescent analogue of the targeted tracer (FITC-PEG$_4$-cRGD$_2$), was developed and successfully used for *in vitro* studies in cell and tissue samples. The availability of this type of dual-modality probe may allow for future clinical translation in the field of image-guided surgery or intraoperative microscopy.

The $\alpha_V\beta_3$-targeted probes used in this study have been characterized our group in detail previously [5]. Briefly, in order to verify its specificity and cellular binding kinetics, I evaluated the colocalization of FITC-PEG$_4$-cRGD$_2$ with the $\alpha_V\beta_3$-specific antibody LM609 in cultured integrin-expressing endothelial cells (HUVECs, chosen because there are no mouse-specific antibodies for $\alpha_V\beta_3$). Importantly, because diabetic animals are known to have uncontrollably high circulating glucose levels (which can alter the endothelial microevironment, induce conformational changes in the vitronectin receptor, and possibly impact other receptor-ligand interactions), in the present work, I also investigated the binding affinity of FITC-PEG$_4$-cRGD$_2$ in a high-glucose environment. I observed no significant change across a range of probe concentrations spaning from 0.01 to 1 μM. This indicates that the differences in the angiogenic response I observed between diabetic and non-diabetic mice were associated with physiological changes due to changes in $\alpha_V\beta_3$ expression and not the binding affinity of the probe. Intriguingly, I note a relative decrease in probe accumulation in the non-ischemic diabetic limbs relative to the non-diabetic limbs. Because the binding affinity of the probe is unaffected by a high-glucose environment, I attribute this to a decrease in $\alpha_V\beta_3$ expression in the diabetic animals.

Following the *in vitro* applications, I evaluated the specificity of the probe *in vivo*. The

labeling protocol I use involves first dissolving ^{64}Cu in acetate buffer, and then combining that with a solution of the unlabeled probe. It is therefore important to show that labeled acetate exhibits no obvious accumulation in ischemic tissue. I subjected animals to a surgical femoral artery ligation and injected them with either ^{64}Cu-NOTA-PEG$_4$-cRGD$_2$ or the non-specific ^{64}Cu-acetate. I found a greater accumulation of ^{64}Cu-NOTA-PEG$_4$-cRGD$_2$ in the ischemic hindlimb relative to the non-ischemic hindlimb while ^{64}Cu-acetate showed comparable accumulation in both limbs paralleled by strong uptake in other organs. This further verifies the suitability of the ^{64}Cu-NOTA-PEG$_4$-cRGD$_2$ for *in vivo* targeted imaging of angiogenesis.

In order to establish that the animal model used in the investigations faithfully mimics diabetes-associated pheripheral ischemia in human patients, I measured a number of important diabetic markers in experimental animals. The animals were first treated with STZ for three days which resulted in significant increase of circulating blood glucose levels. In humans, this can caused changes in both the short term (altering the expression levels of several proteins) and long term (giving rise to glycosylated hemoglobin) [134, 135]. These animals showed similar clinical signs of short- and long-term effects, including enhanced GSP and HbA1c levels (taking about 6 weeks after STZ treatment to fully materialize). Moreover, these enhancements were found to correlate with the decrease in angiogenic response confirmed with PET-CT imaging. Taken together, these findings represent an important part of establishing the utility of the model for the study of diabetes-associated vascular complications.

We next sought to establish the optimal time point for PET-CT imaging after administration of the ^{64}Cu-NOTA-PEG$_4$-cRGD$_2$ by performing biodistribution studies at various time points after injection of the radiotracer. I found a time interval between 1 and 2 hours to be optimal, demonstrating low blood activities and significant accumulation within the ischemic tissue. I found that the main excretion route was via the bladder, which is favorable for probes with translational applicability because it avoids accumulation within the digestive track, and poses relatively little risk to other organs.

We validated the results from the PET-CT imaging and quantitative image analysis by postmortem evaluation of the radioactivity of excised tissues using gamma well counting. Gamma well counting is traditionally considered a "gold-standard" technique that enables measurement the absolute values of radiotracer activity. It is immune to several limitations that image-based whole body analyses face, including the partial volume effect and tissue attenuation. Unfortunately, gamma well counting is highly invasive, the animals need to be euthanized and tissues samples collected postmortem. I found a strong positive correlation between the image-based analysis and gamma well counting results. As expected, uncorrected PET-CT image analysis tended to underestimate the magnitude of the absolute ^{64}Cu-NOTA-PEG$_4$-cRGD$_2$ uptake (expressed as %I.D./g) which I attribute predominantly to partial volume errors (tissue attenuation is negligible in small animals), detector sensitivity and different energy ranges. This discrepancy could be potentially eliminated using partial volume correction techniques, normalization of detector efficiency and allowing comparable energy ranges.

The results of the PET-CT study strongly suggest reduced $\alpha_V\beta_3$ activity in the onset of diabetes, which negatively affects the angiogenic process. This observation is further verified by immunofluorescence staining in which diabetic tissues showed a significant reduction in the expression of CD31, CD14, and CD74 (markers of endothelial cells, macrophages, dendritic cells, and vascular repair) and retention of FITC-PEG$_4$-cRGD$_2$. This finding is in agreement with studies performed previously by the group using both SPECT and PET cRGD-based tracers, and by others using more invasive techniques [136]. Diabetes-induced impairment of collateral blood vessel formation has also been demonstrated in other preclinical animal models of diabetes [5, 137].

While the underlying causes are not completely understood, attenuated angiogenesis in diabetes has been linked to improper degradation of the basement membrane, to alterations in the delicate balance of growth factors and cytokines that regulate vascular stability, and to problems in signal transduction including VEGF dysregulation (as shown by reduced

expression of VEGF mRNA and protein) [136]. Rivard *et al.* in particular, demonstrated that hindlimb ischemia created by ligation of the femoral artery was associated with a greater reduction in capillary formation and blood flow to the ischemic limb in diabetic transgenic mice (NOD) relative to non-diabetic (C57) wild type mice. In these studies, NOD mice showed a much lower rate of perfusion (ischemic limb to normal limb) 14 days following femoral artery ligation and a reduction in capillary density in ischemic hindlimb muscles at 35 days when compared with healthy littermates [136].

Although others have investigated the effects of diabetes on neovascularization, most have relied on invasive assessment techniques with little applicability in the clinical setting. Due to its non-invasive nature, PET-CT imaging represents a powerful tool for studying the vascular complication of diabetes, in the laboratory, and perhaps some day in the clinical practice. The ability to image active angiogenesis may enable earlier detection of vascular pathologies, and better evaluation of treatment options for patients with peripheral arterial disease. These could lead to more personalized therapeutc interventions and ultimately better patient outcomes.

3.5 Conclusions

Diabetes is known to cause severe vascular complications that can lead to debilitating injury, and in some cases even death. While early detection of these complications remains a challenge, new methods involving focused regional PET-CT acquisitions of $\alpha_V\beta_3$ activity are showing promise as a means of assessing tissue angiogenesis *in vivo*. I have demonstrated this promise using a new molecular probe to image neovascularization within ischemic tissue in diabetic and non-diabetic mice. To achieve that goal I established an optimal animal model to mimic PAD in DM patients. This approach enables a quantitative spatio-temporal characterization of $\alpha_V\beta_3$ activity that may one day allow for the real-time evaluation of the therapeutic efficacies of different medical interventions (medicinal, surgical, or emerging

genetic or cell-based interventions). The dimeric cRGD-based imaging probe displays intense focal retention, leading to *in vivo* acquisitions of superior image quality. Coupled with favorable blood clearance kinetics and optimal biodistributions, its potential for clinical use in imaging and monitoring angiogenesis in patients with peripheral vascular disease is significant.

Chapter 4

Multidimensional Assessment of PAD †

4.1 Introduction

The main function of the cardiovascular system is to provide the tissues of the body with well-perfused vascular beds capable of delivering vital oxygen, nutrients, humoral agents, the collecting and removing metabolic waste [138, 139]. Angiogenesis, the process by which new vessels are formed from preexisting ones, is involved in the maintenance of these vascular beds, as well as a wide range of other biological processes—both benign and pathological—including vascular remodeling, wound healing, endometriosis, and cancer [22, 24, 25, 140].

Peripheral arterial disease (PAD) is characterized by a progressive arterial stenosis often leading to the occlusion of the peripheral arterial bed, and is associated with an elevated risk of cardiovascular and cerebrovascular events. Although approximately 27 million people in Europe and North America have the disease, PAD still remains largely underdiagnosed [141].

As PAD progresses, the narrowing vasculature reduces blood flow to the periphery, resulting in a decreased perfusion and increased hypoxia. These changes in microenvironmental conditions can in turn activate one or both of the primary revascularization pathways. Angiogenesis, which is triggered under hypoxic conditions, leads to the formation of new capillary beds from preexisting vessels. It is a dynamic and complex multistep process, which requires endothelial proliferation and remodeling, an interplay of various pro- and anti-

†Work includes material incorporating contributions from Jamila Hedhli MinWoo Kim, Hailey J. Knox, Than Huynh, Matthew Schuelke, Iwona T. Dobrucki, Leszek Kalinowski, Jefferson Chan, Albert J. Sinusas, Michael F. Insana, Lawrence W. Dobrucki.

angiogenic factors, and interactions among endothelial cells, extracellular matrix (ECM) and smooth muscle cells [128]. Arteriogenesis, which is triggered by changes in the biomechanical properties of the vasculature as a result of decreased blood flow, leads to the enlargement of preexisting arteriolar connections in order to establish collateral circulation.

Despite significant progress, a complete understanding of the complex web of interactions that mediate the angiogenic and arteriogenesis responses remains elusive. This is not for lack of effort; a large and growing list of experimental techniques have been brought to bear over the last decades, each illuminating its own piece of the larger puzzle. Traditional molecular and cellular biology methods have elucidated many biochemical details of intracellular angiogenic signalling [62, 142, 143], while more physiologically-minded approaches, such as measurement of blood flow, blood volume, and vessel permeability, have been used to characterize hypoxia-induced angiogenesis at the tissue level and in whole animal [4, 144, 145].

Of particular importance, the past several years have revealed new methods for the non-invasive *in vivo* imaging of peripheral vasculature. These include major advances aimed at imaging blood perfusion using ultrasound (US) [3, 146], photoacoustic imaging (PA) [147], and laser speckle contrast imaging (LSCI) [148], as well as quantitative molecular imaging approaches using radiolabeled probes targeted at specific angiogenic biomarkers such as matrix metalloproteinases, VEGF isoforms, and $\alpha_V\beta_3$ integrin [5, 60, 89, 102, 107, 122, 127, 149, 150]. While each of these imaging modalities is powerful on its own, and capable of providing functionally relevant windows into the molecular and physiological processes in both animals and humans, their greatest potential lie in their combined use as part of a broader multimodal imaging strategy. A 2008 review by Cai *et al.* highlighted the importance of such a multimodal approach, and predicted that the future of angiogenesis research rests in the combination of multiple imaging modalities yielding a synergistic and complementary view [129]. This vision was recently realized in the recent study [2], in which LSCI was paired with targeted PET-CT imaging of $\alpha_V\beta_3$ to demonstrate multifaceted actions of mesenchymal stem cells resulting in an increase of angiogenesis and blood perfusion recovery in a murine model of

peripheral arterial disease (PAD).

Understanding both the progression of PAD and the bodily response to the disease, requires the simultaneous evaluation of several interrelated molecular, anatomical, and functional parameters, all within a living subject. These parameters include various gene expression, blood perfusion, and oxygenation levels in different muscle tissues. In this article, I employ an integrated multimodal approach to study PAD with SPECT imaging using two molecular probes targeted at HIF-1α and $\alpha_V\beta_3$, as well as high resolution Ultrasonic Power Doppler, PA, and LSCI for perfusion and blood oxygenation imaging. Combined, these methods offer a unique profile of hypoxia-induced angiogenesis that ties together the roles of a key regulator (HIF-1α), one of its biologically-important targets (the $\alpha_V\beta_3$ integrin), and the effects of their combined activity on angiogenesis, perfusion, and tissue oxygenation. In addition, this study also reports on one of the first preclinical uses of label free power Doppler US for blood flow imaging [3], with improved sensitivity to enable greater differentiation between fast (arterial) and slow (capillary) flows. Once developed, this technology may allow for routine assessments of microvascular health by primary care professionals, and ultimately, improved patient management leading to better outcome.

4.2 Methods

Our research plan is outlined in Figure 4.1. Briefly, 4 to 6 week old mice were subjected to the right femoral artery ligation to induce peripheral ischemia. Animals were imaged serially with several modalities at various time points to investigate spatiotemporal changes within the ischemic microenvironment.

4.2.1 Animals

All experiments were performed according to the guiding principles of the American Physiological Society and approved by the Institutional Animal Care and Use Committee.

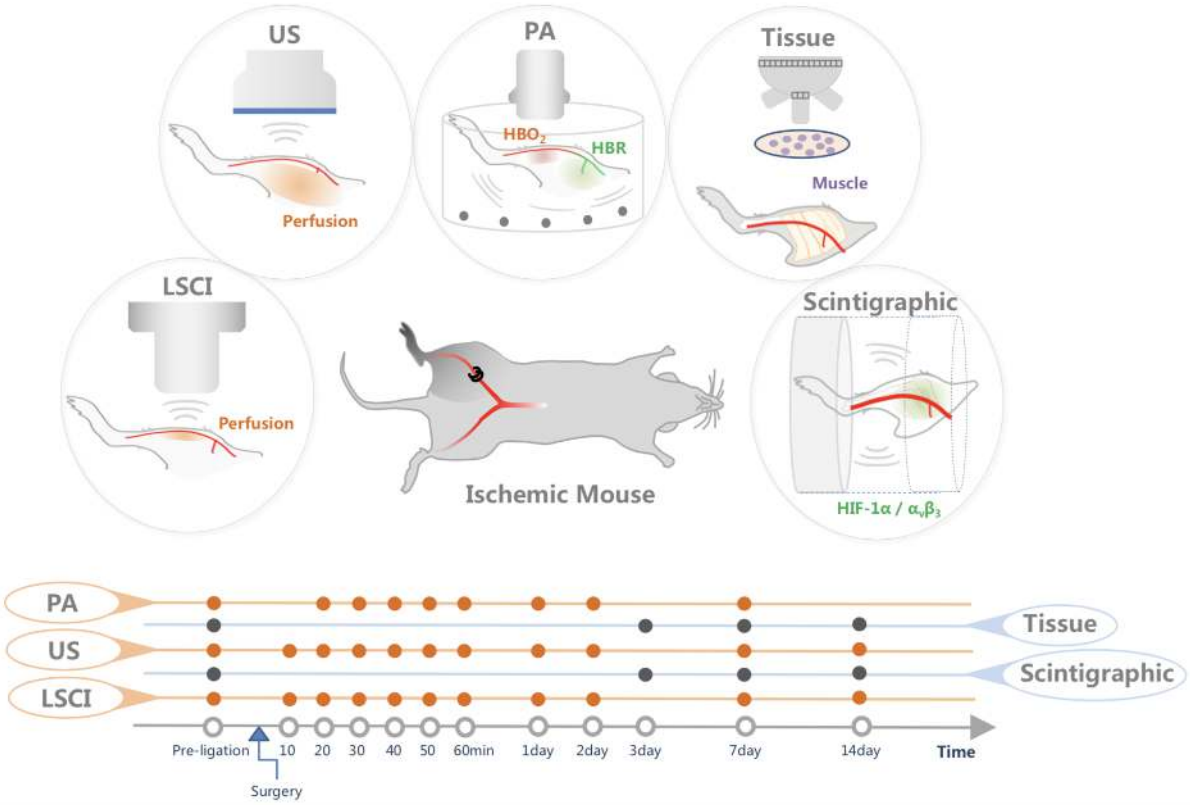

Figure 4.1: Study overview. The right femoral artery was ligated to mimic PAD. The animals were serially evaluated for $\alpha_V\beta_3$ and HIF-1α (using SPECT), measures of blood perfusion (using US, LSCI, and PA). At days three, seven and 14, skeletal muscle tissue was extracted for immunohistochemistry experiments (denoted Tissue).

Induction of unilateral hindlimb ischemia via surgical ligation of the right femoral artery to was performed according to procedures described previously [123]. Briefly, 29 male black C57BL/6 mice (Charles River Laboratories, US) were anesthetized with 1-3% isofluorane. The right femoral artery was exposed and two ligatures were placed distally to the profundus branch and proximally from the artery bifurcation. On the opposite leg, a sham operation was performed which included a skin incision, and exposure of the left femoral artery, but no ligatures were placed. The surgical model used in all experiments resulted in small postoperative wounds with minimal inflammation, and the formation of collaterals between several proximal vessels including the profundus branch and the distal section of the femoral artery. The mice were allowed to recover for serial scintigraphic imaging of $\alpha_V\beta_3$ integrin

and hypoxia.

4.2.2 Ultrasound Imaging

A subset of seven (n=7) animals were used for perfusion assessment employing US. Mice were placed in a supine position on a heating pad set to 37 °C, and both hindlimbs extended. Animals were imaged prior to ligation surgery and at a series of post-operative time points (10, 20, 30, 40, 50, and 60 minutes, and 1, 2, 7, and 14 days). Echo data were acquired using a Vevo 2100 system and an MS 400 linear-array transducer (FUJIFILM VisualSonics Inc. Toronto, Ontario, Canada). The transducer, emitting 2-cycle pulses with a 24 MHz center frequency, was positioned on an ischemic region of each animal's hindlimb. The focal depth was set between 4–6 mm, and the aperture size was adjusted to maintain f/2. A color-Doppler acquisition frame included a packet size of 17 pulses transmitted at a time interval of 1 ms giving a slow-time pulse repetition frequency (PRF) of 1 kHz. For each pulse transmission, beam formed IQ echo data were recorded for off-line analysis. The scan-lines were separated laterally by 0.06 mm. For each animal, 100 Doppler frames were recorded with a frame-time interval of 0.11s. The complex-valued IQ echo data are represented by 3-D data array, $\boldsymbol{\mathcal{X}} \in \mathbb{C}^{N \times S \times K}$, where N, S and K are the numbers of slow-time samples, spatial samples, and frames, respectively (see Figure 4.2).

A filtering procedure can then be applied in order to isolate blood components from unwanted clutter (*e.g.* surrounding tissue motion and acquisition noise). I adopt a block-wise method to enhance the filter performance. This technique is robust to the high degree of complexity associated with the spatiotemporally-varying characteristics of the data sources. The full data array $\boldsymbol{\mathcal{X}}$ are divided into overlapping sub-arrays $\tilde{\boldsymbol{\mathcal{X}}}_j \in \mathbb{C}^{\dot{N} \times \dot{S} \times \dot{K}}$, $j \in \{1, \cdots, J\}$, where J is the total number of blocks. Each sub-array is individually processed by a higher-order singular value decomposition (HOSVD) technique to detect the local perfusion. The

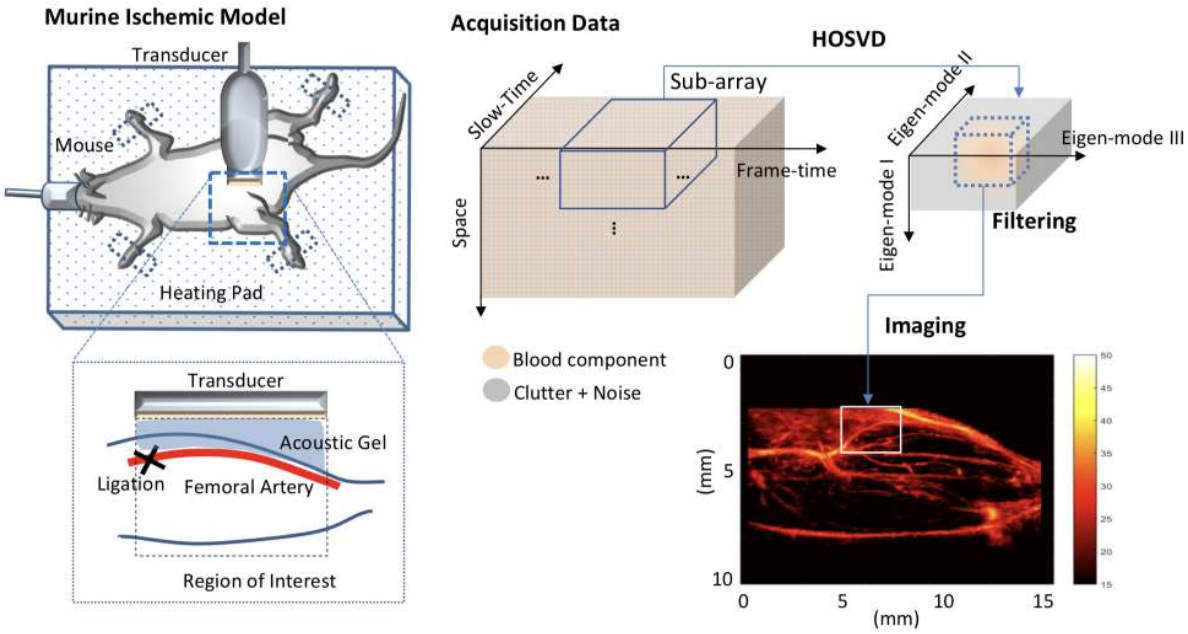

Figure 4.2: Ultrasound imaging and data analysis protocol. An anesthetized mouse is placed in a supine position and its right femoral artery is ligated to induce ischemia. Without contrast-enhancement, standard Doppler ultrasound acquisition results at 24MHz in 3D data array involving spatial, slow-time (kHz-order sampling rate), and frame-time (Hz-order sampling rate) axes. The data array is divided into sub-blocks and each data block is individually processed by the HOSVD methodology [3] to detect local blood perfusion.

HOSVD of $\tilde{\boldsymbol{\mathcal{X}}}_j$ is expressed as

$$\tilde{\boldsymbol{\mathcal{X}}}_j = \sum_{(i_1,i_2,i_3)\in\Omega} g_{i_1,i_2,i_3} \boldsymbol{u}_{i_1} \times \boldsymbol{v}_{i_2} \times \boldsymbol{w}_{i_3}, \tag{4.1}$$

where Ω signifies full space and $\times$ is an outer-product operation. The vectors $\boldsymbol{u}_{i_1}$, $\boldsymbol{v}_{i_2}$ and $\boldsymbol{w}_{i_3}$ are i_1, i_2 and i_3th eigenvectors for the slow-time, spatial and frame-time modes, respectively. The new coordinates, by means of combination of the eigenvectors, naturally give rise to a separation of the sources through their statistical independence. g_{i_1,i_2,i_3} is associated with signal power at (i_1, i_2, i_3)th coordinates. The filtering is performed by selecting the subspace where blood dominates and rejecting the rest where clutter and noise dominates. The process

can be expressed as

$$\tilde{\boldsymbol{\mathcal{B}}}_j = \sum_{(i_1,i_2,i_3)\in B} g_{i_1,i_2,i_3} \boldsymbol{u}_{i_1} \times \boldsymbol{v}_{i_2} \times \boldsymbol{w}_{i_3}, \tag{4.2}$$

where $\tilde{\boldsymbol{\mathcal{B}}}_j$ is the filtered data and B is the blood subspace. The subspace is roughly determined by prior knowledge of properties of the sources. The optimal one is empirically selected by comparison of the resulting image contrast. The local spatial perfusion is estimated by averaging signal power $|\tilde{\boldsymbol{\mathcal{B}}}_j|^2$ over slow-time and frame-time axes, and converting the result to dB-scale. The final image is obtained by compounding all J local estimates (Figure 4.3). See the table 4.1 summarizing all parameter values.

Parameter	Value
Axial (fast-time) samples (M)	200-272
Axial sampling rate	24.0 MHz
Axial size	6.4-8.7 mm
Slow-time samples (N)	17
Slow-time sampling rate	1.0 kHz
Frame-time samples (K)	100
Frame-time sampling rate	9 Hz
Scan-line numbers (L)	240-250
Scan-line density	16.67 lines/mm
Lateral size	14.4-15.0 mm
Spatial samples (S=LM)	48000-68000
Sub-block size ($\dot{N}\times\dot{S}\times\dot{K}$)	17×768×30
Slow-time division (J_1)	1
Spatial division (J_2)	1600
Frame-time division (J_3)	10
Sub-block numbers (J=$J_1J_2J_3$)	16000

Table 4.1: Parameters

4.2.3 Laser speckle contrast imaging

Seven (n=7) animals imaged previously with ultrasonic Power Doppler were also scanned using laser speckle contrast imaging prior to ligation surgery and at a series of post-operative time points (10, 20, 30, 40, 50, and 60 minutes, and 1, 2, 7, and 14 days). Images were obtained

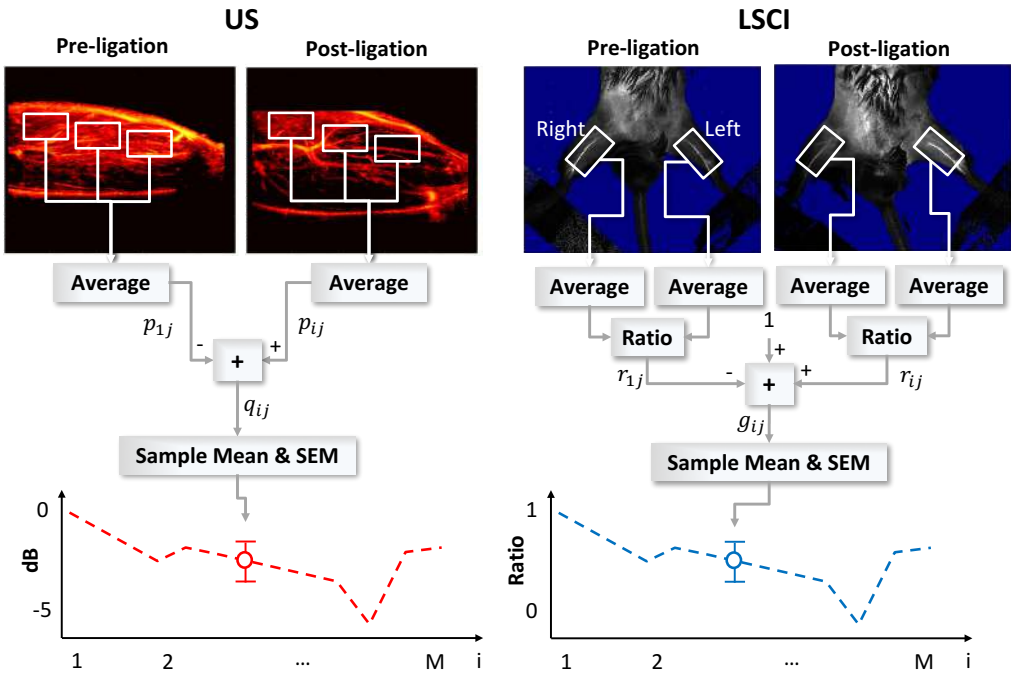

Figure 4.3: Perfusion quantification using US and LSCI. US and LSCI images were obtained at multiple time points before and after femoral artery ligation. The white rectangular windows in the images represent individual ROIs over which perfusion was averaged. In the US images, the difference between the pre- and post-operative state was computed for each mouse sample. Subsequently, the mean and SEM of this difference was plotted at each time point. The graph shows 0 dB pre-ligation ($i = 1$) as a reference, and the relative changes for all post-ligation timepoints ($i > 1$). In the LSCI images, the ratio between an ischemic right hindlimb region and its corresponding healthy left hindlimb region was computed, and their difference (plus unity, such that all values are relative to 1) was plotted.

using a moorFLPI-2 laser perfusion imager (Moor Instrument, UK) operated from a Windows-based computer system installed with the moorFLPI software (moorFLPI Measurement V3.0, Moor Instruments, Devon, UK). Before initiating measurements, the laser speckle instrument was calibrated according to the manufacturer's recommendations. Then, a divergent beam (785 nm, near-infrared) illuminated hindlimb tissue to a 1 mm in depth. High-resolution speckle images were acquired using a 768 $\times$ 576 pixel grayscale charge-coupled device camera set to record each frame for a duration of 60 seconds. In addition, the feet of three (n=3) mice were imaged prior to surgery and at 1 hr, 1 day, 2 days and 7 days post-surgery. For collateral circulation assessment, the skin was removed from the right hindlimb of the animal. The mice were imaged prior to surgery, and subsequently at 2,10, and 25 min post-ligation.

4.2.4 Photoacoustic imaging

Another subset of seven (n=7) mice was used for PA imaging. Each animal, was imaged with Endra Nexus 128 PA tomographer (Endra, Inc., Ann Arbor, MI, USA) at (20, 30, 40, 50, and 60 minutes, and 1, 2, and 7 days) post-surgery. Images were acquired at 750 and 850 nm using continuous rotation mode with a 6 second rotation time. A 3D reconstruction was performed for each image, and signal intensity was accumulated over an 8 mm thick slab. The signal in each PA image was quantified by determining the mean PA signal in a 2 mm^2 region of interest (ROI). A ratiometric signal was determined by taking the ratio of signal at 750 nm to 850 nm. Data was processed using the freely available Horos software (Horos Project, https://www.horosproject.org/).

4.2.5 Perfusion trend analysis for ultrasound and laser speckle contrast imaging

Perfusion images obtained through Power Doppler US were used to track tissue perfusion changes over the course of two weeks. Through imaging the animal hindlimbs at various time

points (before and after ligation), I were able to track the average perfusion changes over the regions illustrated in (Supplementary Data, Figure S1). These regions intentionally exclude arteries in order to focus on tissue perfusion. The depth of each region was set to less than 6 mm to provide a consistently high echo signal to noise ratio. The average perfusion during the ith time point in the jth mouse is represented as

$$p_{ij}, i \in \{1, \cdots, M\}, j \in \{1, \cdots, N\}, \tag{4.3}$$

where M and N are the number of time points and mice included in this study, respectively. We compute the change in perfusion over time as $q_{ij} = p_{ij} - p_{1j}$ where p_{1j} is the preligation regional perfusion value. The temporal variation is analyzed by plotting sample mean $\bar{q}_i = \frac{1}{N}\sum_{i=1}^{N} q_i$ and standard error of the mean (SEM) $\tilde{q}_i = \sqrt{\frac{1}{N}}\sqrt{\frac{1}{N-1}\sum_{i=1}^{N}(q_i - \bar{q}_i)^2}$ for every time point i.

The trend for LSCI was obtained by a comparable procedure, but I report the ratio of signal from the right ischemic hindlimb to that of the left control hindlimb:

$$r_{ij} = \langle p_{ij}^{(R)} \rangle / \langle p_{ij}^{(L)} \rangle \tag{4.4}$$

where $\langle p_{ij}^{(R)} \rangle$ and $\langle p_{ij}^{(L)} \rangle$ are perfusion averages over the boxes on right and left hindlimbs, respectively. Because the spatial absolute image values are highly sensitive to ambient light conditions I normalize the perfusion change using $g_{ij} = r_{ij} - r_{1j} + 1$ and plot the mean and SEM for g_{ij} at every time point.

4.2.6 Blood oxygenation analysis for Photoacoustic Imaging

Because the oxygenated (HbO_2) and deoxegenated (HbR) forms of hemoglobin have different near-infrared absorbsion properties, PA is able to detect the relative level of blood oxygenation [151]. Briefly, the amplitude of the acquired PA image describes the local energy absorption at wavelength λ_i. This in turn can be expressed as $\phi(\lambda_i, x, y, z)$, with a spatial average $\bar{\phi}(\lambda_i)$.

The contribution of the two forms of hemoglobin to the spatial mean absorption can be represented as

$$\bar{\phi}(\lambda_i) = \epsilon_{HbR}(\lambda_i)[\text{HbR}] + \epsilon_{HbO_2}(\lambda_i)[\text{HbO2}] \tag{4.5}$$

where ϵ_{HbR} and ϵ_{HbO2} are the molar extinction coefficients of HbR and HbO_2 at wavelength λ_i, respectively. The operator $[\cdot]$ denotes the relative concentration of hemoglobin. The two concentrations can thus be estimated by a least squares solution as

$$\begin{bmatrix} [\text{HbR}] \\ [\text{HbO}_2] \end{bmatrix} = \left(\begin{bmatrix} \epsilon_{HbR}(\lambda_1) & \epsilon_{HbO_2}(\lambda_1) \\ \vdots & \vdots \\ \epsilon_{HbR}(\lambda_L) & \epsilon_{HbO_2}(\lambda_L) \end{bmatrix} \right)^{\dagger} \begin{bmatrix} \phi_{jk}(\lambda_1) \\ \vdots \\ \phi_{jk}(\lambda_L) \end{bmatrix} \tag{4.6}$$

where $M^{\dagger} = (M^T M)^{-1} M^T$ denotes pseudo-inverse of matrix M. The relative change in oxygenation is consequently given as $\eta = [\text{HbR}]/[\text{HbO}_2]$. Three wavelengths, λ_1=750 nm, λ_2=800 nm, and λ_3=850 nm were used to reduce the estimation error, although two measurements could have sufficed in order to determine the concentrations. We employed the table in [152] for corresponding molar extinction coefficients. A total of seven (7) mice were scanned at several time points before and after ligation. I computed each ratio η_{jk} where j and k are indices of the time point and sample, respectively, and finally plotted the sample mean and SEM for every time point to trace the change.

4.2.7 Serial Scintigraphic Imaging

To uniformly assess the *in vivo* specificity of the ^{99m}Tc-labeled peptides, for the purpose of PAD imaging, all animals followed a routine setup. Namely, all animals were laid in a supine position with legs fully extended and immobilized on a polyacrylic board. Animals were then injected intravenously with 1.5 ± 0.2 mCi of the targeting agent on 0, 3, 7 and 14 days of hindlimb ischemia and subjected to dynamic pinhole planar imaging. Planar imaging utilized

a gamma camera (VariCam, GE Healthcare) set with a large field of view and a pinhole collimator coupled to a 1-mm aperture and 15% energy window centered at 140 keV. At 75 minutes post-injection of the radiotracer, a static 15-minute image was acquired. Immediately after the completion of static imaging, all animals were euthanized and tissue samples were collected for gamma well counting for biodistribution and processed for immunostaining.

4.2.8 Biodistribution

For biodistribution studies, a subset of animals (n=6) for ^{99m}Tc-BRU-5921 and (n=5) for ^{99m}Tc-NC100692 were euthanized and selected organ samples were collected for gamma well counting analysis. The weight and the ^{99m}Tc radioactivity of each tissue sample was measured using a gamma well counter (Cobra Packard). The activity measured was corrected for background, decay time, and sample weight.

4.2.9 Histological Validation

A subset of the animals were euthanized before (control) and at 3, 7, and 14 days after the surgical ligation of right femoral artery. Their gastrocnemius/soleus muscle complexes were excised, embedded in TissueTec (Sakura, USA) and snap frozen in -150°C methylbutane. Frozen sections (5 nm) were placed on microscope slides, fixed with pre-cooled acetone, and stored at -80°C before staining. To evaluate skeletal muscle vascularity, muscle samples were stained with either an endothelial cell-specific marker anti-mouse CD31 Antibody (BD Pharmingen) or hypoxia specific marker anti-HIF-1α (BD Pharmingen). To assess probe specificity (FITC-labeled NC100692), muscle samples were stained with both AlexaFluor647-labeled anti-α_V (Abcam, USA) antibody and FITC-labeled NC100692. All staining procedures were performed according to the product-specific protocols. The stains for HIF-1α and CD31 were quantified for extent (percentage area) of positive staining in randomly chosen high-powered (200 $\times$) fields using algorithms validated by the group previously [123]. Colocalization analysis of the histological images was performed using the Fiji image processing package.

Correlated α_V-stained and FITC-labeled NC100692-stained images were analyzed using the Coloc 2 plugin of ImageJ software package. Using this plugin, Manders' coefficients were calculated using Costes method for thresholding [153]. Three images per animal were analyzed, with four animals per experimental group.

4.3 Results

4.3.1 *In vivo* assessment of perfusion using US, LSCI, and PA

The primary goal of monitoring the circulatory system using multiple imaging techniques is to find an accurate, continuous, and non-invasive strategy that can help assess changes in tissue perfusion and the breakdown of homeostasis. Although several methods have been established for perfusion imaging in the clinical setting, none by themselves can offer the fine resolution and variable ranges of depth necessary for detecting microvascular changes. To bridge this divide I adopted three complementary imaging techniques (US, PA, and LSCI) with various penetration depth and imaging contrasts (see Table 4.2).

Imaging Modality	Depth	Contrast Source	Pixel/Voxel representation
US (24 MHz)	4-6 mm	Endogenous	Echo power in dB scale
PA	3-4 mm	Endogenous	Optical absorption
LSCI	1 mm	Endogenous	Optical power in flux scale
Scintigraphic Imaging	No limit	Exogenous	Counts per second

Table 4.2: Non-Invasive Imaging in Small Animal PAD model.

These imaging modalities enable us to "connect the dots" between changes in blood flow through microvascular networks shortly after the onset of ischemia, all the way through to large-scale changes in blood supply seen days or weeks later (Figure 4.4).

Ultrasound enables estimation of deep-tissue peripheral perfusion For each of seven experimental mice, US imaging sessions were performed before the surgical ligation, every 10 minutes after surgery (up to an hour), and at one day, two days, seven days and

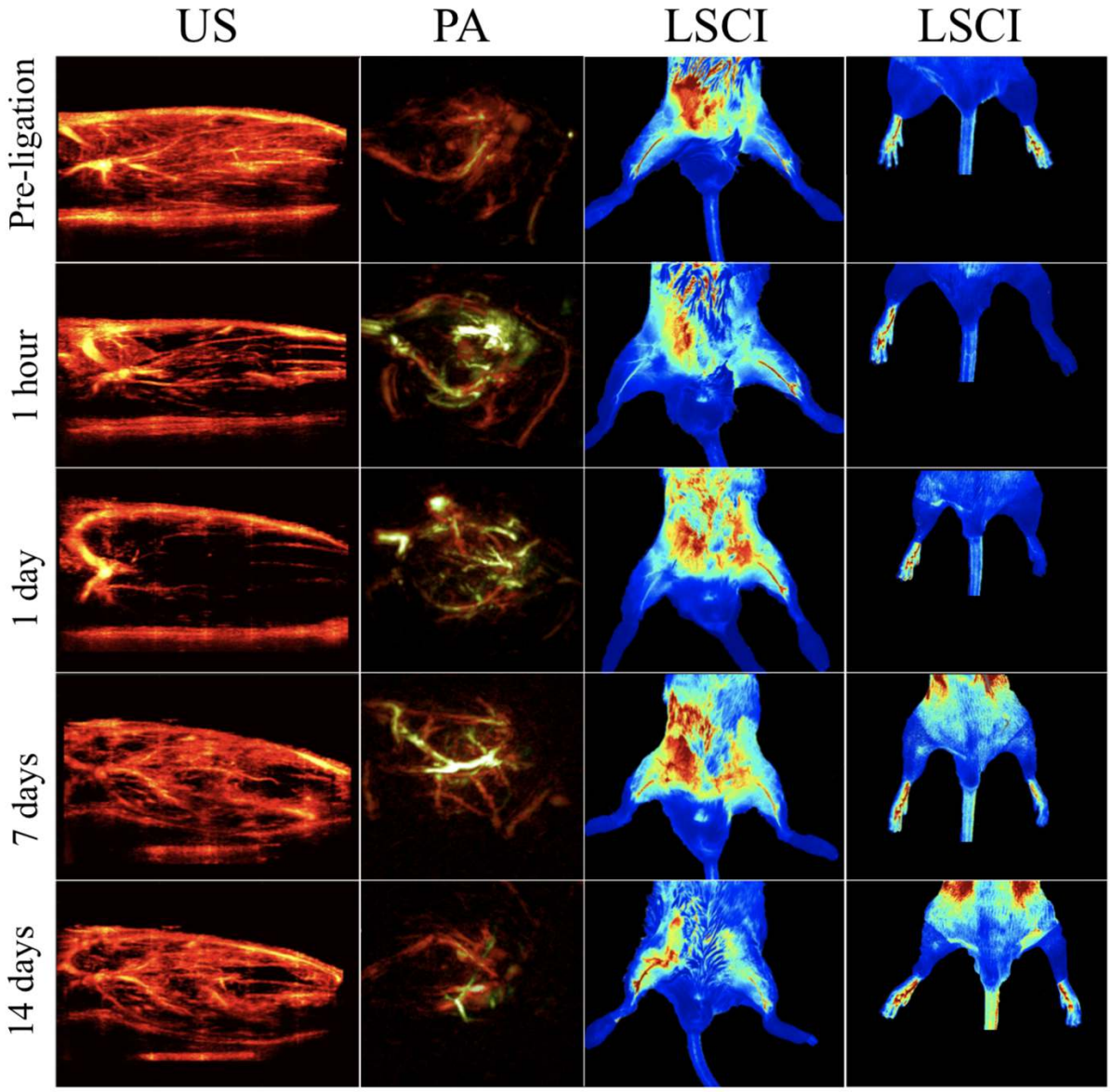

Figure 4.4: Representative multimodal imaging data presented at a series of time points (prior to and following ligation). Each column shows how a different circulatory parameter changes over time as the mice recover. The first column highlights perfusion as a series of 10 mm × 15 mm vertical cross-sections of ischemic tissue imaged using US. Prior to ligation, perfusion generally appears strong, except for the distal regions of the limb where the signal appears to be diminished primarily due to acoustic attenuation. The second columns show PA images of the ischemic tissues excited at 750 nm (for HbR detection, green color) and 850 nm (for HbO2 detection, red color). The third column represented LSCI images of the legs in a horizontal view. The right hindlimbs (appearing on the left side of the images) underwent femoral artery ligation, while the left hindlimbs were used as controls within each animal. The fourth column represents LSCI images of feet.

14 days to monitor spatiotemporal changes in blood perfusion. I found that within the first 10 minutes, a significant drop in the perfusion signal was detected (see Figure 4.5 A). The lowest perfusion levels, however, were not observed until the one or two days post surgery. By day seven perfusion was found to have recovered to near pre-ischemic level.

LSCI reveals the rapid dynamics of the subcutanous tissue perfusion While the deep tissue (imaged with US) showed a relatively slow decrease in blood perfusion after surgery, the dynamics of the surface tissue (assessed via LSCI) were considerably faster. The LSCI signal was observed to continuously decrease over the entire first hour after ligation, and by day one had already started to recover (see Figure 4.5B). Indeed, while the deep tissue showed its lowest level of perfusion at the day two timepoint, the superficial tissue measurements indicated almost complete recovery. This is likely due to the fact that surface tissue contains a higher density of collateral blood vessels, which, during vascular occlusion, can help to rapidly recover blood perfusion [154].

LSCI demonstrates a slow perfusion recovery in lower extremities The traditional approach of assessing perfusion in a laboratory setting, involves imaging the feet of animals using LSCI. As shown in Figure 4.5C I observed an immediate decrease in the ischemic-to-non-ischemic perfusion ratio followed by a slow but steady recovery that takes up to 14 days.

The dynamics of collateral blood vessels post-ischemia To illustrate the transient behavior of blood perfusion found with LSCI, I imaged the collateral blood vessels near the profundus branch before and after ligation. Following the surgery, I observed an abrupt increase in the perfusion of many collateral vessels near the ligation site (see Figure 4.6). This indicates that these smaller vessels, which under normal circumstances play a relatively minor role in blood perfusion, can rapidly increase their flow rate in order bypass a vascular occlusion and maintain downstream blood delivery.

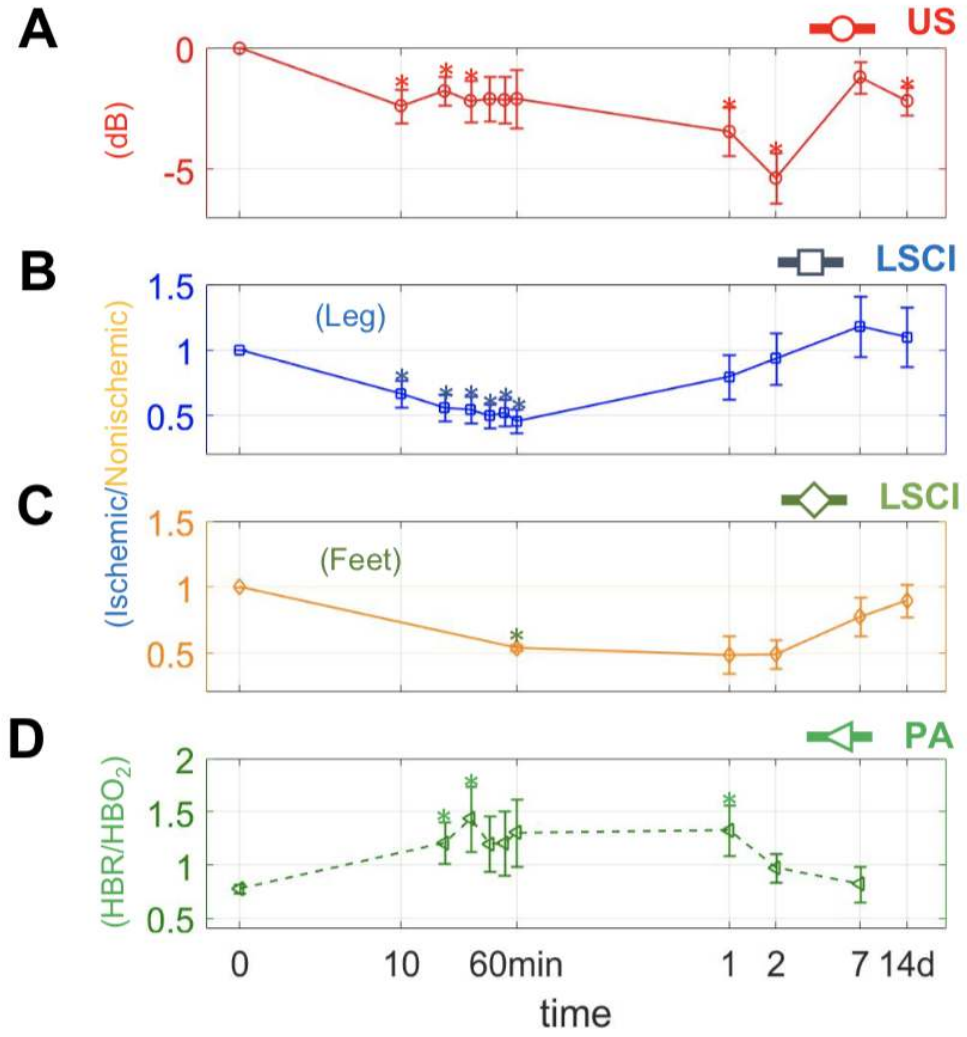

Figure 4.5: Changes in perfusion and hypoxia over a logarithmic timeline. Points marked ($\circ$) and ($\square$) are for perfusion estimates using US and LSCI, respectively. Points marked ($\triangleleft$) indicate the ratio of deoxygenated to oxygenated hemoglobin (HbR/HbO2) as measured via PA. (A)–(D), represents plots of each measure individually. The mark ($*$) above each point indicates a statistically significant ($p < 0.05$) difference from the preligation state.

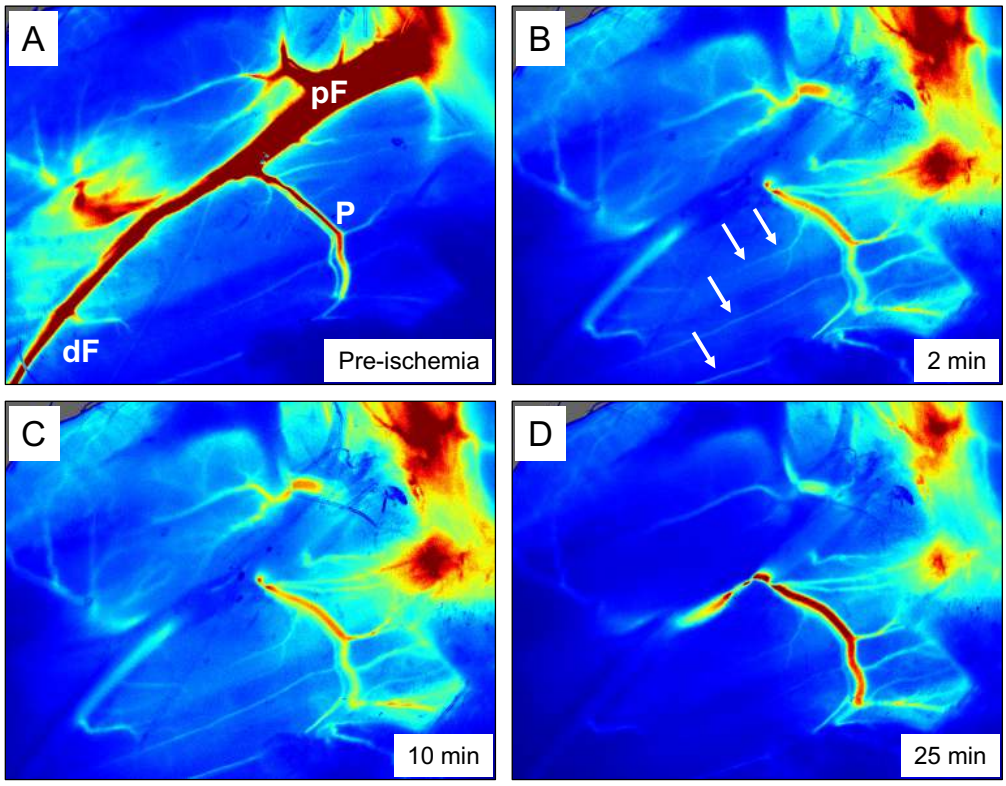

Figure 4.6: Representative LSCI collateral imaging data presented at a series of time points (prior to and following ligation). (A) An intact femoral artery and profundus branch prior to ligation. (B)-(D) The same regions two, 10, and 25 minutes after ligation. An immediate halt in blood flow via the femoral artery can be seen after two minutes. Within the first 10 minutes, a transient increase in collateral blood perfusion can be observed followed by decrease at minute 25. In the images, 'pF' indicates proximal femoral artery, 'P' indicates the profundus branch of femoral artery, and 'dF' indicates the distal femoral artery; white arrows indicate collateral blood vessels that help to maintain perfusion after ligation.

Photoacoustic imaging imparts functional microvascular parameters In constrast to ultrasonic and laser doppler imaging, photoacoustic imaging is capable of quantifying several important physiological parameters, including levels of oxygenated (HbO2, detected at 850 nm) and deoxygenated (HbR, detected at 750 nm) hemoglobin. Using light at wavelengths in the near-infrared region I found that the ratio of HbR to HbO2 increased approximately 1.2 fold after ligation (see Figure 4.5D), and maintained this high level throughout the first day. Some recovery was seen by day two, however by day seven, the ratio had reverted to its preligation value.

4.3.2 *In vivo* monitoring of hypoxia and angiogenesis using BRU-5921 and NC100692.

BRU-5921 and NC100692 exhibit favorable pharmacokinetics

To demonstrate that the radiotracers exhibit favorable organ excretion for the purposes of imaging hypoxia-induced peripheral neovascularization, I performed biodistribution studies 75 minutes after injection of ^{99m}Tc-NC100692 (for angiogenesis) and ^{99m}Tc-BRU-5921 (for hypoxia). ^{99m}Tc-BRU-5921 showed high activity in the kidneys, and substantial accumulation in both the liver and pancreas, whereas ^{99m}Tc-NC100692 demonstrated highest retention in the kidneys and little activity in other organs (Figure 4.7).

Changes in HIF-1α precede changes in $\alpha_V\beta_3$ expression To investigate the role of HIF-1α and $\alpha_V\beta_3$ in peripheral angiogenesis over time (3 days, 7 days, and 14 days), animals were injected via tail vein with either ^{99m}Tc-NC100692 or ^{99m}Tc-BRU-5921. Representative scintigraphic images are shown in Figure 4.8A. With the knowledge that the radiotracers exhibit optimal organ excretion for the purposes of imaging hypoxia-induced peripheral neovascularization (Figures S1), I found that the HIF-1α expression peaked rapidly, within about three days, before returning to normalcy around day seven (Figure 4.8B). $\alpha_V\beta_3$

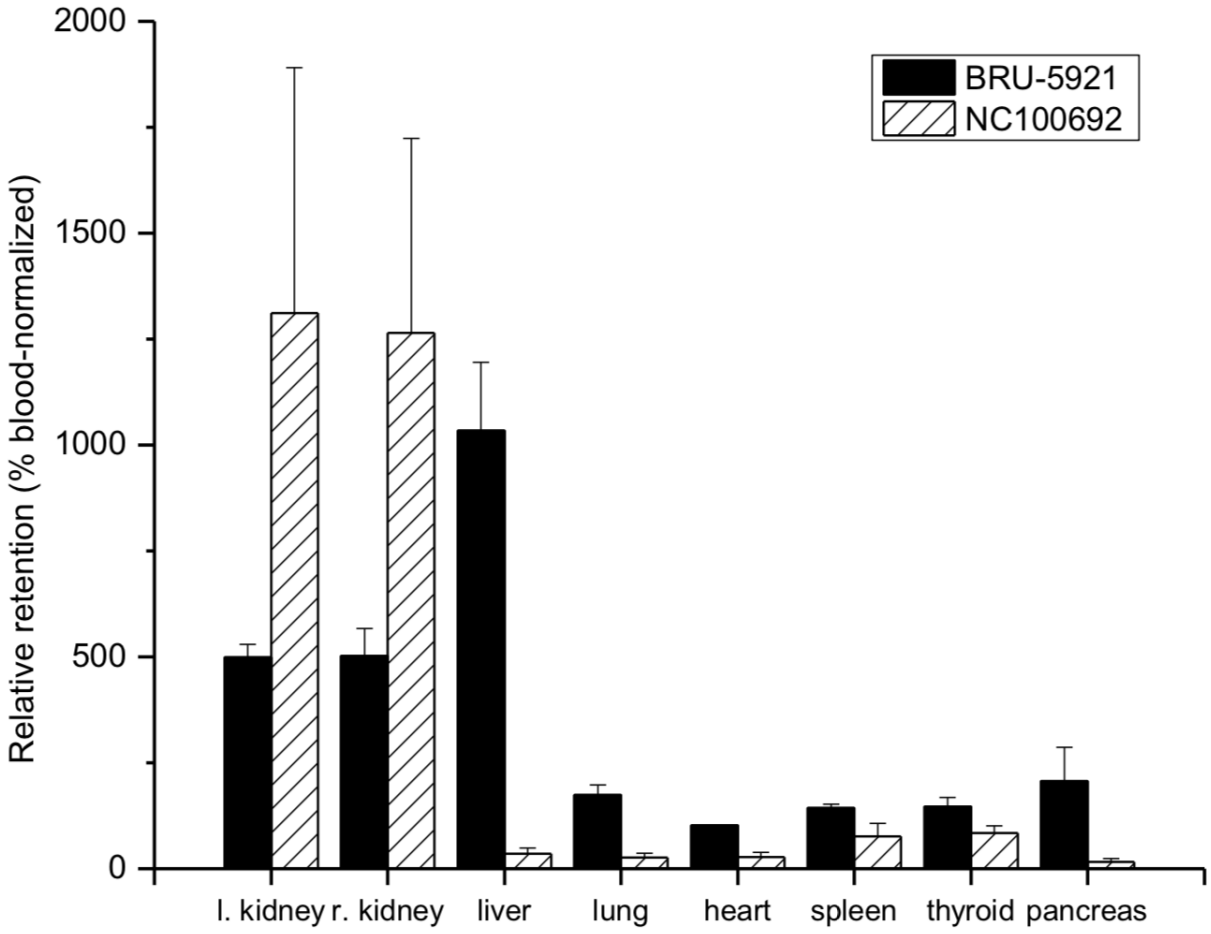

Figure 4.7: Biodistributions of ^{99m}Tc-BRU-5921 and ^{99m}Tc-NC100692 in selected organs at 75 min after intravenous injection. The principal clearance route for ^{99m}Tc-NC100692 was through urination, as evidenced by a very high radiotracer uptake in both kidneys. ^{99m}Tc-BRU-5921 was also principally excreted via urination, although it took somewhat longer, as evidenced by its greater liver retention.

expression, on the other hand, took somewhat longer to peak (approximately seven days), and was not observed at its basal expression level until day 14. These findings are consistant with the role of HIF-1α as a regulator of the angiogenic response—its early induction by hypoxic conditions sets off a cascade of downstream responses, including a significant and sustained enhancement of $\alpha_V\beta_3$ expression.

4.3.3 *In vitro* postmortem evaluation of the ischemic microenviroment

In order to investigate the physiological effects associated with HIF-1α and $\alpha_V\beta_3$ expression, I evaluated tissue samples collected from all experimental animals.

Representative immunohistochemistry are shown in Figure 4.9A, and immunofluorescence images are shown in Figure 4.10A. As shown in Figure 4.9B relative to the non-ischemic control samples, the ischemic tissues exhibited an approximately 14-fold surge in HIF-1α expression three days after ligation which then gradually returned to baseline levels over the remainder of the experiment. Nevertheless, even at the 14 day timepoint, HIF-1α expression remained significantly above its basal level.

In contrast, CD31 positive endothelial cells within the capillaries and small arterioles increased gradually over the course of the experiment, peaking at day 14.

Additional staining, using both AlexaFluor647-labeled anti-α_V antibody and FITC-labeled NC100692, demonstrated not only a strong colocalization, indicating that NC100692 selectively targets cells engaged in angiogenesis, but also a rapid rise coupled with a slow decrease in the angiogenic response (see Figure 4.10B).

4.4 Discussion

PAD, a condition closely associated with coronary artery disease, is a powerful predictor of future cardiovascular pathologies. Despite this, PAD remains largely underdiagnosed and

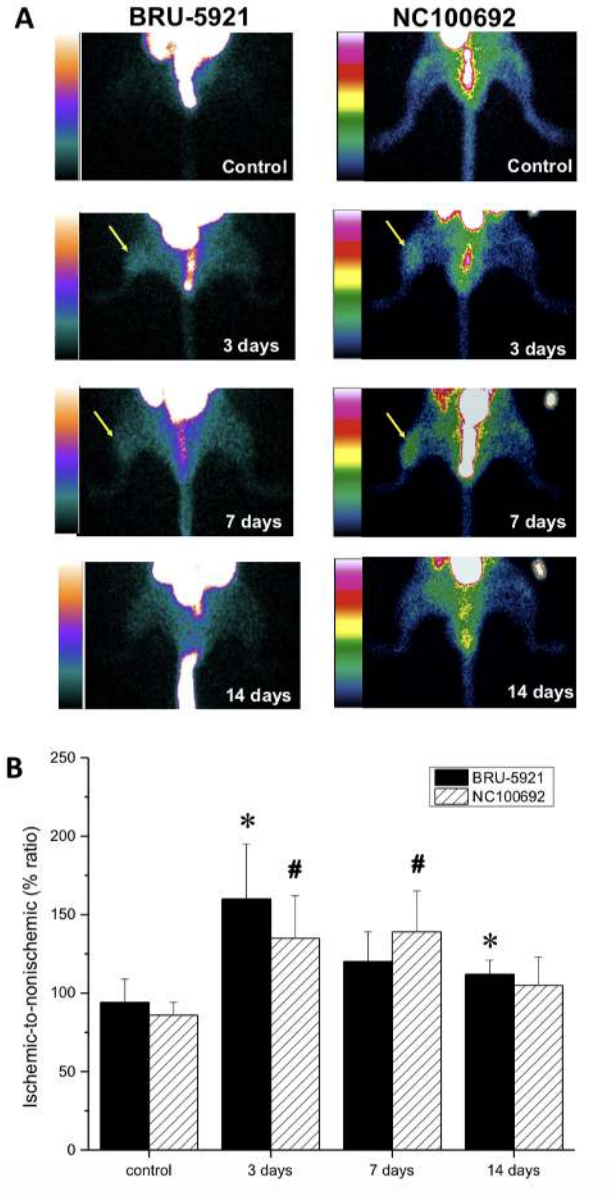

Figure 4.8: (A) Representative planar scintigraphic images of murine hindlimbs acquired at 75 min after injection of HIF-1α-targeted ^{99m}Tc-BRU-5921 (left) or $\alpha_V\beta_3$-targeted ^{99m}Tc-NC100692 (right) prior to, as well as three, seven, and 14 days after surgical ligation. Arrows mark focal uptake of both radiotracers within the ischemic hindlimb. (B)Results from the image analysis using two-dimensional regions-of-interest (ROIs) drawn on planar scintigraphic images of ^{99m}Tc-BRU-5921 (solid bars) and ^{99m}Tc-NC100692 (dashed bars) prior to, as well as three, seven, and 14 days after ligation. Values were expressed as % ratio (ischemic to non-ischemic). Asterisks (*) indicate significant differences ($p < 0.05$) in measured ^{99m}Tc-BRU-5921 activity values relative to the pre-ligation state, while number signs (**) indicate significant differences in ^{99m}Tc-NC100692 activity.

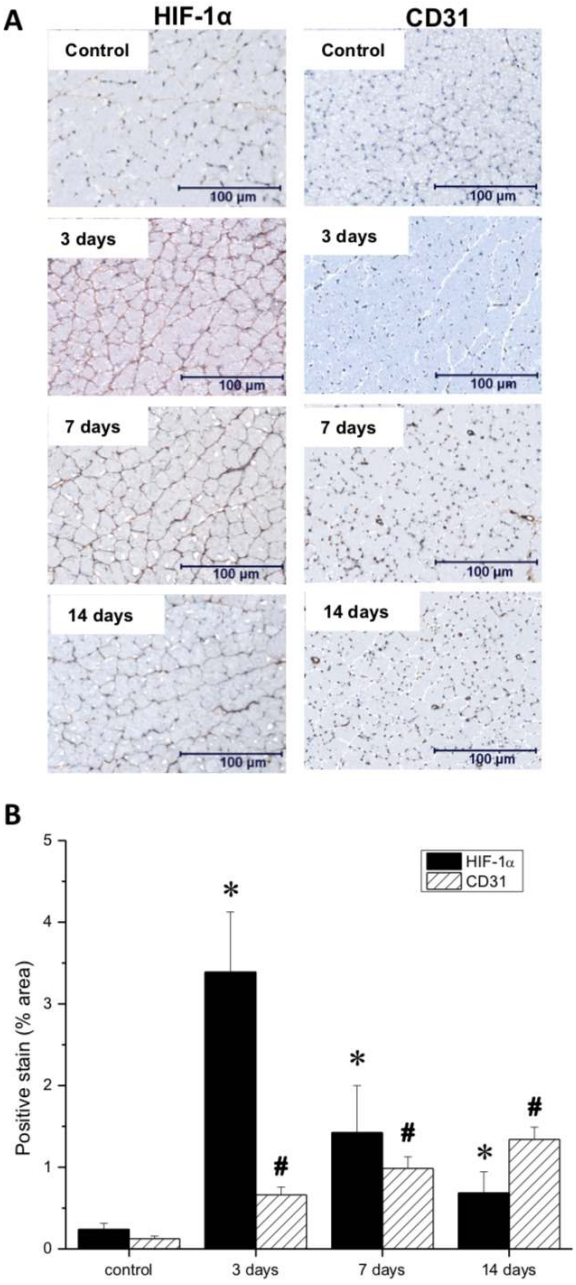

Figure 4.9: (A) Representative immunohistochemical microscopic images of gastronemius muscle collected from the ischemic hindlimb prior to (control), and at three, seven, and 14 days after ligation. Tissue samples were stained with primary antibodies against hypoxia-inducible factor-1 (HIF-1α, left) and platelet endothelial cell adhesion molecule, or PECAM (CD31, right).(B) Quantitative analysis of immunohistochemical microscopic images. Values were expressed as % area of positively stained tissue (HIF-1α shown in black, CD31 shown with diagonal lines). Asterisks (*) indicate significant differences ($p < 0.05$) in measured HIF-1α expression relative to the pre-ligation state, while number signs (#) indicate significant differences in CD31 activity.

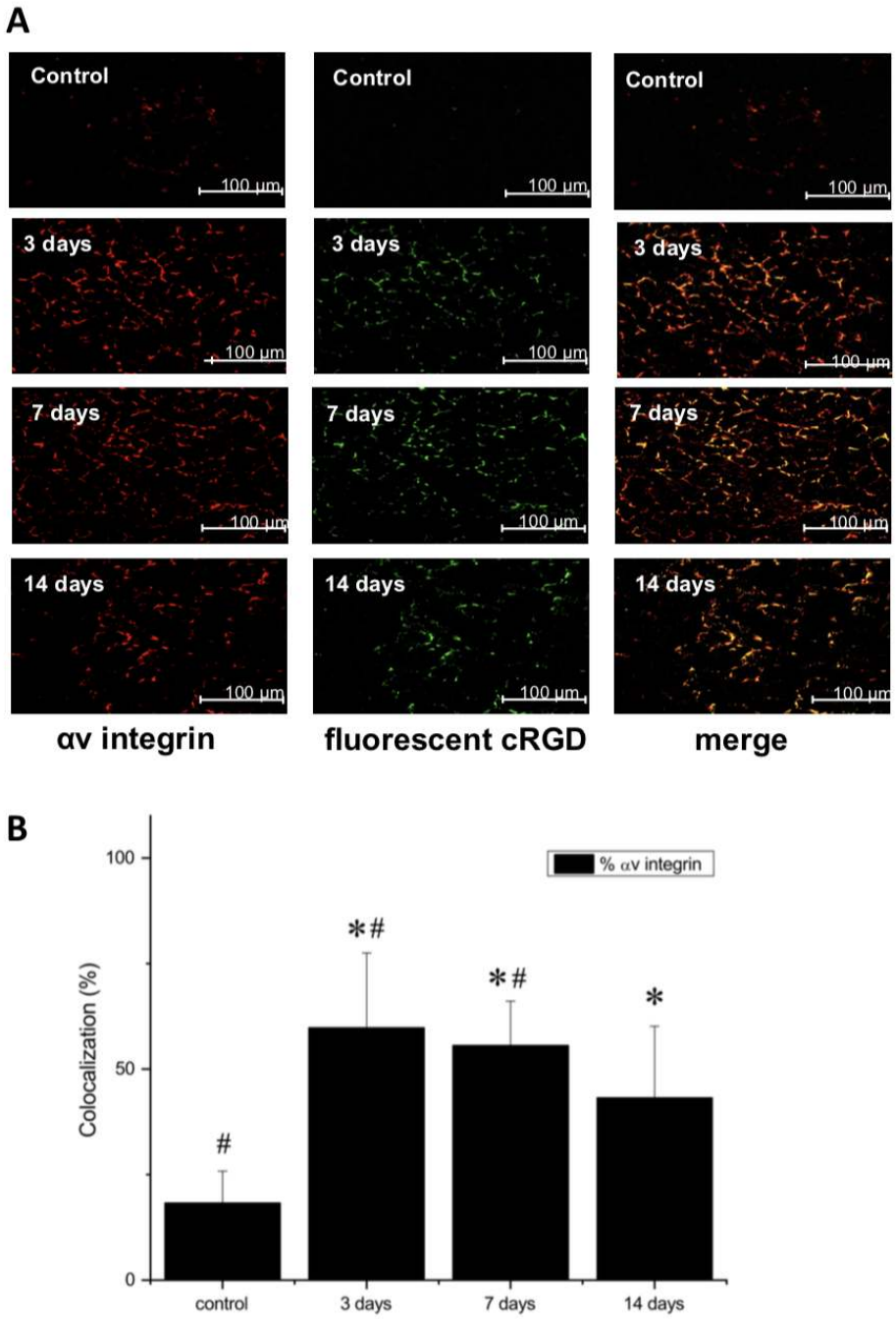

Figure 4.10: (A) Representative microscopic images of gastrocnemius muscle collected from ischemic hindlimb before (control), and at 3, 7, and 14 days after the surgical ligation of right femoral artery simultaneously incubated with an antibody against α_V integrin (left) and fluorescent FITC-labeled analogue of NC100692 (middle). Right column represents a result of merging of two color channels (α_V integrin and fluorescent analogue of NC100692).(B) Quantitative analysis of co-localization between α_V integrin and fluorescent analogue of NC100692 in ischemic gastrocnemius muscle samples collected before (control) and at 3, 7, and 14 days after the surgical ligation of right femoral artery. Values are presented as percentage of cells expressing α_V integrin co-localized with fluorescent FITC-labeled NC100692 analogue (solid bars). $*P < 0.05$ vs. control. $\#P < 0.05$ vs. 14 days after ligation.

undertreated [141].

One of the primary drivers of this investigation was to explore applications of a new Power Doppler US technology sensitive enough to not require exogenous contrast enhancement when detecting spatiotemporal changes in muscle perfusion. Although US imaging has been a mainstay in the healthcare industry for over sixty years, and it is widely used for the detection of blood circulation, its limited sensitivity in low-flow conditions has rendered it unsuitable for imaging the peripheral microvasculature until now [155]. The Power Doppler US methodology I employed in this study can detect relative perfusion changes within capillary beds using conventional instrumentation that samples and filter echos signals in new ways. Using this method, I monitored the 14 day ischemia-reperfusion time course in healthy mice throughout the hindlimb (Figure 4.5A). I used 24MHz (about 3 times the frequency of clinical imaging) because of the small size of the hindlimb. This method offers a safe and low cost approach to serially assess tissue perfusion.

We used this Power Doppler method, along with several other imaging techniques, to construct a comprehensive timeline of the bodily response to peripheral vascular occlusion at both the molecular and physiological levels (Figure 4.11).

In the deep tissue, I found a slow decrease in the perfusion feature that manifested over the course of approximately 48 hours (although the shallower tissue showed a considerably faster drop-off). Shortly thereafter (approximately 72 hours after ligation), molecular markers for hypoxia and angiogenesis (HIF-1α, CD31, and $\alpha_V\beta_3$) were then found to be up-regulated. In the case of HIF-1α specifically, this up-regulation persisted until approximately day seven, before falling off as the tissue oxygenation returned to normalcy.

The ability to perform fast serial assessments also proved critical to the possible detection of a reactive hyperemia response shortly after ligation. Although modest in size, I note an increase in tissue perfusion at the 20 min time point relative to the 10 and 30 minute values (a similar uptick in oxygenation was noted at the 30 min time point (Figure 4.5A&D). One possible explanation may lie in a surge of endothelial nitric oxide (NO) production

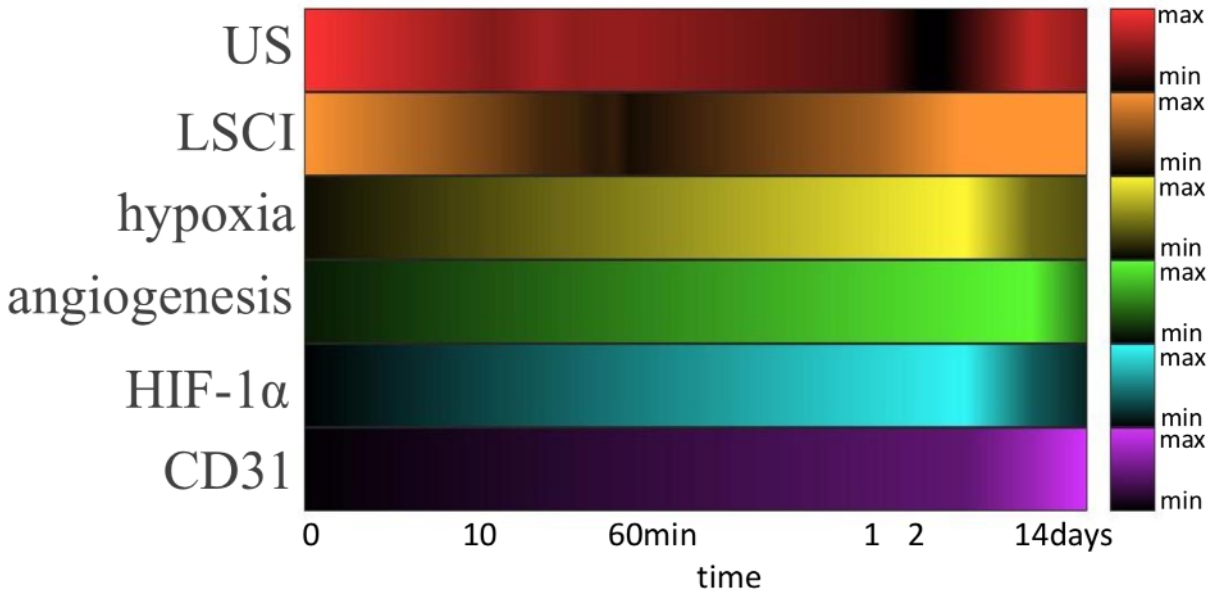

Figure 4.11: Heatmaps depicting measured circulatory parameters over a log-time axis. In each case, darker colors represent lower relative measurements, and the 0 timepoint indicates pre-ligation. While US (red) measures perfusion of the deep tissue ($\sim$ 6 mm), LSCI (orange) measures perfusion within 1mm of the tissue surface. Hypoxia (yellow) and $\alpha_V\beta_3$ (green) expression were both measured using SPECT imaging with the targeted probes ^{99m}Tc-BRU-5921 and ^{99m}Tc-NC100692, respectively. HIF-1α (blue) and CD31 (purple) expression in ischemic tissue were quantified from immunohistochemistry images.

stimulated by the hypoxia conditions as shown by see Figure 4.6. A complete understanding of the role of NO in vascular remodeling and angiogenesis remains elusive, and the available research can be somewhat contradictory [156]. Nevertheless, previous studies have shown that: 1) NO modulates the consumption of oxygen when blood flow is restricted by competitive inhibition of cytochrome oxidase [157], 2) hypoxic tissue expression increased levels of vascular endothelium growth factor (VEGF), which in turn gives rise to endogenous release of NO. Other pathways have also been implicated in the reactive hyperemia response, including endothelium-derived relaxing factor (EDRF), a vasodilator with similar biological function as NO [158–161]. Additional studies will be required to establish the role of NO in short-term perfusion the nature of the enhancement in perfusion I see at the 20 minute time point, and to investigate possible therapeutic effects of NO on the ischemic microenvironment.

With the utility of the new ultrasonic Power Doppler technology established, I next sought

to use it as part of a broader multimodal imaging strategy to study the onset of and recovery from PAD. To that end, I employed LSCI and PA over the study time course to non-invasively inspect superficial blood perfusion and oxygenation, respectively.

Within the surface tissue, the LSCI data showed that hindlimb recovery from ischemia occurs considerably faster than in deeper tissue. While the US imaging revealed that it took approximately 7 days to show signs of vascular recovery within the muscle mass, the surface tissue was clearly recovering as early as 48 hours post ligation. The simplest explanation for this observation lies in the differences in vascular physiology of the surface and deep tissues. In addition to angiogenesis, there exists a secondary type of vascular remodeling which involves the growth of preexisting collateral arterioles into functional collateral arteries. Dubbed arteriogenesis, this type of blood vessel growth is not regulated by hypoxia, but by the changes in sheer stress that accompany the decrease in blood pressure associated with ligation [162, 163]. Because the vascular density in the surface tissue is generally quite high (presumably due to selection pressure favoring fast wound healing), arteriogenesis in these tissues might lead to the recovery of blood flow much faster than would otherwise be possible relying on angiogenesis alone.

For patients with PAD, amputation of the extremities may become necessary in situations where there is extensive tissue death due to prolonged ischemia. Indeed, the clinical presentation of severe ischemic ulcers or frank gangrene are recognized as the sixth stage of PAD manifestation according to Rutherford's classification [155]. I therefore investigated perfusion within the feet of the animals using LSCI and found that blood flow recovered more slowly in the feet than in the distal muscle mass, taking approximately 14 days on average (in close agreement with reports by other authors) [148]. This slow recovery highlights the necessity of developing new screening methods capable of detecting PAD early on, before irreperable damage is done.

PA with a penetration depth of 5 mm enables label free imaging of microvascular flow with high signal-to-noise ratio. This allows users to easily differentiate superficial capillaries

and deep tissue vessels [164], but it can also be used to characterize functional microvascular parameters including HbO2 and HbR concentrations [164, 165]. I found that 20 min after ligation, the ratio of HbR/HbO2 increased (suggesting hypoxia condition), and this enhancement continued until approximately two days after ligation, when the blood oxygenation began to rise (Figure 4.5D). Because the US measurements indicated that perfusion did not show signs of recovery until day seven, these results seem to indicate that blood oxygen levels can recover early in the angiogenic response.

While US, LSCI, and PA give valuable information on the anatomical and functional changes that occur during the body's response to vascular occlusion, they offer little information on the biomolecular cascades that underpin this response. To that end, I added nuclear imaging techniques to investigate two different aspects of angiogenic signalling at the molecular level.

There are two known pathways capable of activating the quiescent angiogenic process: HIF-1α activation by hypoxia; and alterations in oncogene activity. Either way, once started, the angiogenic process depends on $\alpha_V\beta_3$ to regulate the migration of vascular endothelial cells. I concluded the inquiry by non-invasively monitoring tissue hypoxia and $\alpha_V\beta_3$ expression in the ischemic mouse hindlimb. The animals were injected via tail vein with either peptide based probe ^{99m}Tc-NC100692 or small molecule ^{99m}Tc-BRU-5921—to target $\alpha_V\beta_3$ and hypoxia, respectively. Over the course of two weeks, I monitored both targets' expression levels in the ischemic tissue and determined that the highest hypoxia level occurred three days after ligation (confirmed by HIF-1α expression using immunohistochemistry) and that this was followed by a steady decline over the next few imaging sessions. $\alpha_V\beta_3$, on the other hand, did not achieve its highest signal intensity until day seven (also confirmed by immunofluorescence experiments, and coinciding with the first indications of perfusion recovery in the US data). Taken together, these results are in agreement with the known *in vitro* model of hypoxia-induced angiogenesis [166]. The ischemic environment upregulates HIF-1α activity, which in turn sets off a signaling cascade that eventually leads to vascular remodeling and enhanced

$\alpha_V\beta_3$ expression. As the vasculature is repaired, the hypoxia that originally upregulated HIF-1α begins to diminish, and by day seven I observe a decline in HIF-1α expression followed by a corresponding decline in $\alpha_V\beta_3$ expression a few days later.

Although HIF-1α and $\alpha_V\beta_3$ have been the subjects of intense scientific scrutiny over the years, to the knowledge no other group has monitored their expression dynamics simultaneously in an *in vivo* animal model. Both ^{99m}Tc-NC100692 and ^{99m}Tc-BRU-5921 showed favorable biodistributions and pharmacokinetics, and their potential for translation is high, with obvious applications in the diagnostics and monitoring of various pathologies including vascular diseases and cancer.

When viewed together, multimodal imaging approach paints a holistic picture of peripheral limb responses to vascular occlusion at the anatomical, functional, and molecular levels. I observe that the effects of ligation are almost immediate, with perfusion and oxygenation levels dropping substantially just minutes after the operation. From there, I noticed that in the deep tissue, the angiogenic response can take approximately three days or more to be fully elicited, beginning with a rapid rise in HIF-1α expression followed by a slower rise in $\alpha_V\beta_3$ expression. The effects of angiogenesis, *viv-a-vis* blood perfusion, do not manifest until approximately a week after ligation. I also see that the surface tissue undergoes a very different mode of recovery than does the deep tissue, beginning to reestablish normal blood perfusion within just two days, likely through arteriogenesis rather than angiogenesis. I believe that medicine is already shifting toward the type of multimodal imaging assessment employed in this study. And while several challenges remain, the insights gained through this multifaceted approach is considerably greater than would be possible using any of its constituent imaging methods alone. The unique platform constructed by the different imaging techniques will allow to develop new therapeutic strategies for PAD and non-invasively monitor their effects.

4.5 Conclusions

Although significant advances in non-invasive vascular imaging have been made, arteriography, a relatively invasive technique which requires injection of the vascular contrast, remains the standard method for evaluating PAD in the clinical setting. Meanwhile, the prevalence of PAD in Europe and North America is currently estimated at 27 million people and growing.

Fifteen years ago, a commentary by Belch *et al.* called for new diagnosis and treatment options for PAD [141]. In this study, I employ a new Power Doppler US methodology that I believe has the potential to answer that call. It enables the detection of PAD in its early stages without exogenous contrast agents using low cost instrumentation commercially available today. This will allow general practitioners, who are usually the first point of contact with a patient, to recognize and diagnose the disease early and often at a lower cost, ultimately leading to more effective treatment and better patient outcomes.

We also present an integrated, non-invasive, multimodal study to image the bodily response to vascular occlusion. In many respects, these results show a great deal of promise. The molecular probes, ^{99m}Tc-NC100692 and ^{99m}Tc-BRU-5921, demonstrated favorable biodistributions and pharmacokinetics, and their resulting images are readily quantifiable. They clearly show the dynamics of hypoxic condition and stimulation of $\alpha_V\beta_3$ expression within the ischemic microenvionment, and their potential for translation appears high. Just as exciting, the US, LSCI, and PA—all fast, relatively inexpensive, and label-free non-invasive techniques—gave rise to a very detailed picture of spatiotemporal changes in blood perfusion and oxygenation. It's through these methods, for example, that the divergent responses to ischemia of superficial and deep tissues can be detected and understood. Overall, I believe that this work represents an important step in the development of multimodal imaging strategies, with applications in both the research and clinical settings.

Chapter 5

Non-invasive Monitoring of Therapeutic Intervention in PAD †

5.1 Introduction

The main cause of the poor clinical outcome of diabetes mellitus (DM) patients suffering from PAD is their reduced capacity for neovascularization, an important bodily response to vascular occlusion [136]. Despite considerable technological advancement, mortality and both morbidity resulting from PAD remain high, even before diagnosis or treatment thresholds are met. Lifestyle changes and increased exercise are regarded as the most effective treatment for complications associated with PAD. In more critical PAD cases, therapies generally rely on mechanical revascularization through either percutaneous or surgical approaches. Unfortunately, these approaches are frequently unsuccessful in the long term. More recently, novel therapies involving the delivery of proangiogenic factors, either directly or through gene transfer, have been introduced, with some now in clinical trials [128, 167, 168]. The majority of these new therapies target only a single biomarker associated with PAD, such as vascular endothelial (VEGF) or fibroblast growth factors (FGF). Due to the complexities of the biochemical networks involved, however, such oversimplified approaches often fail to give rise to demonstrable improvements in actual patients. More holistic interventions capable of altering the microenviroment of endothelial cells and rendering them suitable for angiogenesis could be more effective. As a result, interest has shifted toward cell-based approaches utilizing

†Work includes previously published material incorporating contributions from Hedhli Jamila, Konopka Christian J, Schuh Sarah, Bouvin Hannah, Cole John A, Huntsman Heather D, Kilian Kristopher A, Dobrucki Iwona, Boppart Marni D, and Dobrucki, Lawrence W [2].

the potential of progenitor and stem cells as agents of tissue repair and neovascularization.

Targeted stem cell-based therapies appear to provide clinical improvement for PAD patients by enhancing vascular density (angiogenesis), initiating large vessel remodeling (arteriogenesis), and ultimately improving blood perfusion [169]. Of the various potential candidate cells that might be used in treating PAD patients, mesenchymal stem cells (MSCs) are being pursued the most actively at both preclinical and clinical levels [169]. Several properties of MSCs make them well suited to the task. Most importantly, through their paracrine-related effects, MSCs have been shown to promote angiogenesis, arteriogenesis, and terminally differentiate into vascular cells and myocytes [170]. They have also been shown to release anti-apoptotic, anti-fibrotic, immunomodulating, and chemoattractant factors, and their inherent metabolic flexibility and resistance to ischemic stress has been shown to fascilitate their survival in ischemic environments [171]. Muscle-derived MSCs (mMSCs) are particularly attractive due to their abundance and the ease with which they can be extracted. The surgical excisement of skeletal muscle tissue carries little risk, and the subsequent isolation and culturing of mMSCs is extremely straightforward. Moreover, their long-term passaging capacity and immunomodulatory properties could allow for allogeneic transplantation into many different tissues with little risk of rejection.

Previous studies involving diabetic mice have shown that angiogenesis is directly impaired by the high endothelial glucose levels associated with diabetes [172]. As a result, the longterm effects of uncontrolled diabetic hyperglycemia include ischemia, especially in the extremities, and subsequent debilitating injury. In this article, I investigate the use of mMSCs to treat surgically-induced hindlimb ischemia in a diabetic mouse model of PAD. I employ several minimally invasive *in vivo* imaging and diagnostic approaches (nuclear, laser doppler perfusion, muscle function and microarray transcriptomics) in order to construct an accurate picture of the effects of the transplanted mMSCs, as well as the response of the mice to treatment, and their long-term prognosis. I find that mMSCs lead to greatly enhanced neovascularization roughly one week after treatment. I also find that at the two-week

timepoint, the transcriptional profile of the stem-cell treated mice resembles that of healthy mice while a control group treated with saline continue to express anti-angiogenic factors, indicating a relative lack of healing. The translational nature and timeliness of this work is significant, and the results have potentially important clinical implications for the evaluation and management of diabetic patients with PAD. Also, noteworthy is the impressive specificity and favorable biodistribution of the molecular probe used in the nuclear imaging studies. The clinical implications of using targeted molecular imaging in PAD are substantial, as they can help to detect diseases earlier, evaluate treatment effectiveness over time, and ultimately help to tailor therapy regimens to individual patients.

5.2 Methods

The research plan is outlined in Figure 5.1. Briefly, type 1 diabetes was chemically induced in 4 to 6 week old mice; their right femoral arteries were ligated to mimic PAD, and they were treated with either sterile saline (control) or transplanted with mMSCs isolated from a different group of animals of similar age and genotype. After treatment, the ischemic DM animals were assessed for angiogenesis (PET-CT), blood perfusion (LDF), and muscle function (FUNC) at different timepoints after surgery.

5.2.1 Isolation of muscle-derived mesenchymal stem cells (mMSCs) from skeletal muscle

Five-week old C57BL/6 mice gastrocnemius-soleus complexes were excised, mechanically and enzymatically digested, filtered, and incubated with anti-mouse CD16/CD32 (Ebioscience, USA) in order to block non-specific Fc-mediated interactions. Cells were then stained with both monoclonal anti-mouse Sca-1^{+}PE (Ebioscience, USA) and $CD45^{-}$APC (Ebioscience, USA) antibodies and isolated with FACS. Sca-$1^{+}CD45^{-}$ cells were then collected in media for culture.

5.2.2 Cell Culture

mMSCs were grown to confluence in Dulbecco's Modification of Eagle's medium (DMEM, Fisher Scientific, USA), containing 10% heat-inactivated FBS (Invitrogen), 100 U/mL penicillin G, and 100 μg/mL gentamicin, and were maintained in a humidified incubator at 37°C with 5% CO_2.

5.2.3 Western blotting

mMSCs and human umbilical vein endothelial cells (HUVEC, known to express $\alpha_V\beta_3$) were washed three times in sterile phosphate-buffered saline (PBS). Cell pellets were collected by centrifugation and incubated in a solution of RIPA buffer (Sigma-Aldrich, USA) and Protease Inhibitor (Sigma-Aldrich, USA). The cocktail was sonicated 3 times for a length of 20 seconds with a 10 second incubation on ice. The lysed cells were centrifuged for 15 min and the supernatant (protein) was collected. The concentration of protein was determined using Gen5 Microplate Reader and Imager Software (BioTek Instruments, USA). A total of 20-10 ng of proteins were resolved on 10% SDS-polyacrylamide gel electrophoresis and transferred onto PVDF membranes (Immobilon, Millipore). Membranes were blocked in Tris-buffered saline (TBS) containing 10% non-fat dry milk and 0.1% Tween 20, prior to incubation with 80 μCi of ^{64}Cu-NOTA-PEG$_4$-cRGD$_2$ targeted to $\alpha_V\beta_3$ (a well characterized marker of angiogenesis) for 1 hour at room temperature. After washing the membrane with PBS, they were transfered on the multisensitive phosphor screen (Perkin-Elmer, USA) and imaged with Cyclone Plus Storage Phosphor System (Perkin-Elmer, USA).

5.2.4 Angiogenic cytokines array

For cytokine analysis of protein extracted from ischemic tissue of stem cell and saline animals, I used mouse antibody angiogenesis array membrane (Abcam – ab139697, 24 target proteins) as per manufacturer instructions. Protein samples were incubated with blocked

membranes overnight with the membranes at 4°C. Prepared membranes were exposed for the protein detection. The membranes were scanned and analyzed using Biorad Image Lab 5.2 software. The signal was normalized to the positive control signal intensity as proposed by the manufacturer.

5.2.5 *In vivo* evaluation

Animal preparation All *in vivo* imaging experiments were performed with the approval of the Institutional Animal Care and Use Committee of the University of Illinois at Urbana-Champaign, following the principles outlined by the American Physiological Society on research animal use.

Permanent hindlimb ischemia in DM mice Type-1 DM was induced by streptozotocin (STZ) administration (50 mg/kg, i.p. daily for 5 consecutive days) in two months old male wild-type mice (C57BL/6). Previous studies have documented that STZ induces moderate diabetes in 85% male mice with survival up to 4 months after treatment without receiving insulin administration. Mice with fasting glycemia (>200 mg/dL) at 14 days after the first STZ treatment were considered diabetic. Mice were anesthetized with isofluorane and unilateral hindlimb ischemia was surgically induced by femoral artery ligation following previously published approaches [132]. Animals were matched for age and sex, and divided into two groups: a control group (n=10) which was subjected to saline i.m. injections, and an experimental group (n=10) that recieved mMSC i.m. injections. Before the ligation, and at 1, 2, 3 and 4 weeks after the ligation, all animals were delivered to the microPET/SPECT/CT facility for molecular imaging, assessment of perfusion and muscular function.

mMSCs transplantation into hindlimb muscle Cultured muscle-derived Sca-$1^{+}$$CD45^{-}$ cells were collected and suspended in Hank's Balanced Saline Solution (HBSS). Immediately after ligation of the femoral artery (see Section 5.2.5), the experimental group received intramuscular injections of $\sim 4 \times 10^4$ cells in 50 μL of sterile HBSS into three sites in the

gastrocnemius muscle of right hindlimb, while the control group recieved injections of sterile HBSS only. The group has established the optimal number of cells for injection from a previously [171].

In vivo **molecular imaging of angiogenesis and perfusion** One week prior to surgical induction of hindlimb ischemia, as well as 1, 2, 3, and 4 weeks after, all animals were anesthesized with 1-3% isoflurane, the neck area was shaved, and the left jugular vein was isolated for placement of a PE-10 polyurethane catheter (Fisher Scientific, USA) to facilitate administration of the radiotracer. The animals were injected with ∼30 MBq of ^{64}Cu-NOTA-PEG$_4$-cRGD$_2$ targeted at $\alpha_V\beta_3$, a well characterized marker of angiogenesis [5]. Imaging was performed using a dedicated small animal microPET-CT scanner (Inveon, Siemens Healthcare, USA). The animals were placed on the animal bed and ∼60 min after radiotracer injection, a 15 min microPET imaging session was performed. PET imaging was followed by a high-resolution anatomical microCT imaging (360 projections, 80 keV/500 μA energy).

The microPET and microCT images were reconstructed using OSEM/3D algorithm (Siemens Healthcare USA) and cone-beam technique (Cobra Exim), respectively. MicroPET were fused with microCT images and quantified using semiautomated approach developed and evaluated by the group previously [132]. Briefly, complex irregular volumes of interest (VOIs) were generated from the microCT images and applied on the co-registered microPET images to calculate absolute ^{64}Cu activities using Inveon Research Workplace (Siemens Healthcare USA). These complex VOIs included only soft tissue (skeletal muscles) after the removal of bone structures during the image segmentation process.

At the same timepoints (one week prior, and 1, 2, and 4 weeks after surgery) all animals were measured with a needle-like laser Doppler probe (Biopac systems, USA) to asses peripheral perfusion as described in [173]. Succinctly after the probe was calibrated to a known motility standard, the needle was inserted into the gastrocnemius muscle to output a signal that was proportional to the red blood cell perfusion in that area and expressed in

blood perfusion units. Peripheral perfusion was reported as a ratio of ischemic to non-ischemic limb of the same animal.

Measurement of the muscular function To assess the muscular recovery of the animals, an invasive contractile force measurement technique was employed. After the final imaging session at four weeks after surgery animal's maximal isometric hindlimb plantar flexor force was measured using a dual-lever system described previously [174]. Briefly, under anesthesia the animal's sciatic nerve was electrically stimulated, and the resulting muscle forces were measured with a servomotor and control unit (Aurora Scientific, USA). Stimulation was repeated 9 times with 5 s recovery periods for a total of 10 measurements. For each animal, the value of the maximal force output (g) was normalized to the muscle mass (g), and expressed as a ratio of ischemic to non-ischemic limb of the same animal.

Statistical analysis The Student t test was used to compare 2 groups. One-way ANOVA was used to compare multiple parameters. A value of $P < 0.05$ was considered significant.

5.2.6 Post mortem Analysis

Biodistrubution For biodistribution studies, all animals were euthanized at 90 min post-injection and selected organ samples were collected for gamma well counting analysis. All collected sections were weighed and the tissue radioactivity was measured with Wizard^2 gamma well counter (Perkin-Elmer, USA). Measured ^{64}Cu activity was corrected for background, decay time, and tissue weight, and expressed as percent of injected dose per tissue weight (%I.D./g).

Histology and immunohistofluorescence A subset of the animals were euthanized at 2 weeks post surgery and their gastrocnemius/soleus muscle complexes were excised, embedded in TissueTec (Sakura, USA) and snap frozen in -150°C methylbutane. Frozen sections (5 nm) were placed on microscope slides, fixed with pre-cooled acetone, and stored at -80°C

before staining. To assess skeletal muscle vascularity, muscle samples were stained with an endothelial cell-specific marker PE anti-mouse CD31 Antibody (Abcam, USA). All staining procedures were performed according to the product-specific protocols (four for each slide). The stains were quantified for extent (percentage area) of positive staining in randomly chosen high-powered (200 $\times$) fields using algorithms validated by the group previously [123].

5.2.7 Transcriptomics

RNA extraction protocol Total gastrocnemius/soleus muscle RNAs (ligated and non-ligated) from the saline and mMSCs treated mice were isolated using an RNeasy tissue mini-kit (QIAGEN). RNA quality was measured using an Agilent Bioanalyzer and quantified using a Qubit Fluorometer (Life Technologies) before microarray analysis.

Hybridization protocol Saline- or mMSCs- treated skeletal muscle (n = 4 each) were paired with a non-ischemic sample on an array; samples came from the same mouse. I employed a dye-balance design such that of the four replicates of each treated group, two were in red (Cy5) and two were in green (Cy3). A total RNA of 200 ng was labeled using the Agilent 2-color Low Input Quickamp Labeling kit (Agilent Technologies, Santa Clara, CA) according to the manufacturer's protocols. Labeled samples were hybridized to an Agilent mouse 4x44K array and scanned on an Axon 4000B microarray scanner (Molecular Devices, Sunnyvale, CA) at 5 μm resolution. Spotfinding was carried out using GenePix 6.1 image analysis software (Molecular Devices, Sunnyvale, CA).

Microarray analysis description Microarray data pre-processing and statistical analyses were done in R (v 3.3.2) [175] using the limma package (v3.30.6) [176]. Median foreground and median background values from the eight arrays were read into R; no spots were manually flagged as bad. The background was low and even across the arrays, and as such, it was ignored. M-values ($ln(2)$(Cy5/Cy3)) for each array were normalized first with the traditional loess within-array normalization, and then the scale between-array normalization [177].

Agilent's Mouse Gene Expression v2 4x44K Microarray interogates 23,254 genes using 39,030 probes spotted one time (1X), and 399 probes spotted ten times (10X) each based on current annotation information. Correlations between the replicate spots for each probe were high, and so the M-values for replicate spots were simply averaged for each sample. The positive and negative control probes were used to assess what minimum expression level could be considered "detectable above background noise" (5.75 on the $ln(2)$ scale) and then the control probes were discarded. Further quality control investigations were done on individual Cy5 and Cy3 values that were quantile normalized to assess variation among individual samples [177]. Because of the high correlations associated with the mouse/array pairings, and no observable difference between the non-ischemic samples, all statistical analyses were done on the M-values rather than the single-channel values. This is prefereable because the M-values implicitly control for mouse/array pairings using limma's empirical Bayes model that includes a term for the dyes [178]. The equivalent of a one-way ANOVA test was pulled from the model to detect any differences across the three groups (non-ischemic, ischemic saline-treated, and ischemic mMSC-treated). These ANOVA values were used along with updated mappings of probes to Entrez Gene IDs from Bioconductor's MmAgilentDesign026655.db (v 3.4.0) [179] to reduce the 39,429 unique probes down to a set of 11,885 representing expressed, unique genes: first, probes without quantile-normalized expression values > 5.75 in at least 3 of the 16 samples (21,752 probes) were removed; second, probes that did not map to any Entrez Gene ID (2,712 probes) were removed; and lastly for the 2,566 genes with more than one remaining probe, a single probe based on the lowest ANOVA raw p-value was selected. Prior to the statistical analysis, a literature search resulted in 149 genes known to be involved with angiogenesis or peripheral arterial disease. An additional 234 genes (for a total of 383) were identified by finding genes annotated to any of the 26 Gene Ontology terms with "angiogenesis" in the name based on Bioconductor's org.Mm.eg.db package (v 3.4.0). In addition to a one-way ANOVA, three pairwise comparisons were also pulled from the model: saline vs. control, stem cell vs. control and stem cell vs. saline. The False Discovery Rate (FDR) correction

was performed separately for the 383 "a priori" gene set and for the 11,522 additional genes detected above background by the microarray, as well as globally for the one-way ANOVA + 3 pairwise comparisons. Heatmaps for specific genes were made from the quantile-normalized separate channel values, after removing array and dye effects, then scaling each gene to have a mean of zero and a standard deviation of one.

5.3 Results

5.3.1 mMSCs enhance angiogenic activity, perfusion, and muscle function in DM mice

To non-invasively assess the angiogenic activity of mMSC-treated DM mice, I injected and imaged the $\alpha_V\beta_3$-targeted PET-CT probe, ^{64}Cu-NOTA-PEG$_4$-cRGD$_2$, at a series of timepoints after the onset of hindlimb ischemia (see Figure 5.2).

During image analysis, I determined the mean signal within volumes of interest corresponding to both the ischemic and non-ischemic legs of each animal. Their ratio (mean ischemic to non-ischemic) represents a measure of each animal's response to mMSC (or saline) treatment. I determined that angiogenic activity one week after mMSC treatment was enhanced by approximately 80% relative to the saline control group (see Figure 5.3A). This enhancement carried forward to week two in which I found a 40% relative increase. Weeks 3 and 4 were comparable in both groups.

Neovascularization is the first stage of angiogenic recovery. I investigated whether enhanced $\alpha_V\beta_3$ expression translated into blood perfusion recovery. A needle-like laser Doppler probe was used to noninvasively determine the degree of blood perfusion in both the ischemic nonischemic limbs of each animal in the immediate pre and postoperative periods as well as one, two, and three weeks later. I did not find a significant difference between the mMSC- and saline-treated animals one week after femoral artery ligation, however in weeks two and four, blood perfusion increased in the mMSC group by almost 60% relative to the saline

group (see Figure 5.4A).

The next step of this study was to determine if the enhanced angiogenesis and perfusion impacted the muscle function of the diabetic ischemic hindlimb. The study was conducted four weeks after surgery. I found a 1.7-fold increase in muscle strength in the mMSC group relative to the saline group (see Figure 5.4B).

Finally, to assess organ specific uptake of ^{64}Cu-NOTA-PEG$_4$-cRGD$_2$ probe *in vivo*, I performed a biodistribution study at 90 minutes after intravascular injection into saline and mMSC treated mice. As expected, the highest uptake was observed in the kidneys due to renal filtration being the dominate excretion route (11.08 ± 0.98, 3.65 ± 0.44 %I.D./g for cortex and medulla, respectively). Relatively high uptake was also observed in the intestines (4.61 ± 0.30), lungs (2.95 ± 0.19), and the spleen (2.24 ± 0.19) (see Figure 5.3B).

5.3.2 *In vitro* Post mortem evaluation of mMSCs effect on the ischemic microenviroment of PAD

To investigate the impact of mMSC treatment at the cellular level, at two weeks post transplantation, a subset of animals was euthanized (n=4 for both the mMSC- and saline-treated groups), sections of hindlimb muscle tissue were excised, and stained with a commercially available PE-labeled anti-CD31 (endothelial marker). Subsequent fluorescence imaging showed a 3.3-fold increase in the angiogenic activity of the ischemic stem cell treated hindlimb in comparison to the ischemic saline treated hindlimb (see Figure 5.5A). Whereas, the non-ischemic saline and non-ischemic stem cell had no significant change in CD31 expression (see Figure 5.5B-D).

Additional sections of muscle tissue were used to investigate the mRNA expression of several genes involved in the angiogenic process. Globally, I found that gene expression state of the ischemic skeletal muscle of the mMSC-treated group was comparable with that of non-ischemic control muscle, but it differed significantly from the saline treated animals. As expected, samples from the same mouse/array were highly correlated and samples in the

same dye had lower levels of correlation. However, after removing the effects of array and dye, principal components analysis clustering showed that the non-ischemic samples from mice administered with saline were not different from non-ischemic samples treated with mMSCs, and there were no outlier samples (see Figure 5.6A,B).

Moreover, I found almost 2-fold increase in expression of the angiogenenic markers HIF1-α, β_3, and β_5 in the mMSC-treated group relative to the saline-treated group (see Figure 5.7). I also found that TNF-α and CD68 (both markers of inflammation) demonstrated a significant ($p < 0.05$) 1.2-fold enhancement in the saline group, indicating an up-regulation of the inflammatory response. I also noted a 1.2-fold increase in 2,6-phosphofructo-2-kinase, a key enzyme involved in glycolysis, within the mMSC treated tissue.

Sections of ischemic saline- and mMSC-treated muscle tissues were also used to extract and quantify protein expression levels. In accordance with the transcriptomics results, I found an increase in expression of the pro-angiogenic proteins and a decrease in the pro-inflammatory proteins in the stem cell-treated animals relative to the saline-treated animals (see Figure 5.6C)).

5.4 Discussion

Peripheral arterial disease (PAD) involves a broad range of vascular pathologies extending from the cerebral vasculature to lower limb arteries. PAD patients experience insufficient blood flow at rest and during the exercise, which can result in intermittent claudication. Imaging techniques focused on PAD progression have the capability to improve the *status quo* by facilitating earlier detection, guiding patient management decisions, and enabling disease prevention and individualized therapies. The studies presented here utilize novel imaging approaches developed to non-invasively assess the potency of muscle-derived MSCs (mMSCs) as a regenerative therapy to repair and reverse diabetic vascular complications in an established animal model of PAD. A variety of techniques and imaging strategies were

applied to quantify angiogenesis, blood flow recovery, muscular function, and gene expression profiles in mMSC-treated ischemic tissue.

I began the investigation by non-invasively assessing the expression of $\alpha_V\beta_3$ in the two experimental (mMSC) and control (saline) groups utilizing a cRGD-based PET tracer, ^{64}Cu-NOTA-PEG$_4$-cRGD$_2$. I observed an increase in the uptake of the probe in the ischemic hindlimb as early as one week after femoral artery ligation and treatment with mMSC. This was confirmed by an ischemic muscle co-stain of CD31 (a key marker for endothelium cell proliferation). Importantly, as mMSCs do not express $\alpha_V\beta_3$ (data not shown),the increased signal I observed was attributable to the physiological effects of the mMSCs' interactions within the ischemic tissue, *to wit* the enhancement of angiogenic activity. Unfortunately, many of the biochemical details of these interactions are complex, poorly understood, and largely beyond the scope of this manuscript. By week four of the study, the enhancement I observed had largely disappeared, indicating either a return to normalcy for the tissue or a diminishment in the therapeutic effect of the mMSCs. Based on the results of the blood perfusion, transcriptomics, and muscle recovery assays (see below), I believe it is more likely the former rather than the later.

I next tested the hypothesis that the observed differences in $\alpha_V\beta_3$ expression between mMSC-treated and saline mice would translate into perfusion recovery. I evaluated blood perfusion using a needle-like laser Doppler probe inserted at the gastrocnemius-soleus muscle at one, two, and three weeks after surgery. I saw an increase in perfusion at weeks two and three in mMSC-treated group where there was little or no change in the saline-treated group. This indicates that the enhanced $\alpha_V\beta_3$ activity was indeed associated with neovascularization within the mMSC-treated ischemic tissue. The results are in agreement with several other published studies that have found that stimulation of angiogenesis promotes the recovery of tissue perfusion [180]. Moreover, these studies investigated the impact of several factors such as age, sex, and genotype, and found an average time of approximately two weeks for perfusion recovery (provided, of course, no essential genes are knocked out)—a timeframe in

close agreement with the results.

After establishing non-invasively the therapeutic effects of mMSC transplantation into ischemic limb, I wanted to confirm that the observed changes in peripheral angiogenesis and perfusion were associated with a recovery in muscle function. After the four week imaging session, an invasive contractile force measurement technique was employed to measure muscle strength in the ischemic and nonischemic hindlimbs of a subset of the animals. I found a 1.7-fold increase in muscle strength in the mMSC-treated group relative to the saline-treated control group. The mean ratio of ischemic to nonischemic muscle strength of mMSCs-treated animals was approximately 0.89, indicating almost full recovery of muscle function. Due to the invasive nature of the measurements, they were performed on only a small subset of animals (n=2 for both the mMSC and saline groups). As such, statistical significance could not be achieved. Instead, I investigated the expression levels of genes in the MyoD family of muscle regulatory factors, which are known to be expressed on satellite cells (located between the basal lamina and sarcolemma of myofibers) and stimulated by damage to the muscle [181]. The mMSC-treated ischemic muscle showed a significant upregulation of the key regulatory genes such as myogenic differentiation 1 (MYOD), and myogeneic factor 6 (MYF6) in comparison to the saline-treated ischemic muscle tissue, indicating increased muscle regeneration and healing in mMSC-treated animals (see Figure 5.4C).

So far, this study has focused on the physiological effects of mMSC treatment at the animal and tissue levels (neovascularizaton, blood flow recovery, muscle strength). Nevertheless, both PAD and angiogenesis involve a number of cellular-level processes that are orchestrated by a range of microenvironmental cues including those associated with ischemia and hypoxia [182], nitric oxide [183], and inflammation [184]. Investigating how these factors influence the behavior and gene expression state of the cells that make up skeletal muscle tissue, represents an important final part of the study. I performed microarray transcriptomics experiments on excised tissue samples, and attempted to quantify the differential expression of 5 important categories of genes, namely those associated with hypoxia, inflammation, pro-angiogensis,

anti-angiogensis, and metabolism (see Figure 5.7).

Several genes associated with the pro-angiogenic response (such as HIF-1α, β_3 and β_5, Fgfr1, Tgfbr1, Vegfa, Flt1, and Itgav) were found to be enhanced in mMSC-treated muscles. HIF-1α, a transcription factor that mediates the adaptive response to hypoxia and ischemia by promoting angiogenesis, showed a significant increase in mMSC-treated mice compared to the saline group. This confirms that the treatment with mMSCs upregulates the expression of genes involved in initiation of the angiogenic pathway. Interestingly, the ischemic saline treated group actually showed a down-regulation in HIF-1α compared to the nonischemic tissues of the mice. This finding is consitent with other published data, and is attributed to the hyperglycemic environment of the endothelium cells, which is unfavorable for induction of angiogenesis [180].

Expression of these pro-angiogenic genes was found to correlate with metabolic genes such as, fructose-2,6-biphosphatase 2 (Pfkfb2) and the solute carrier family 2 (Slc2a4) genes. It is possible that the vascular remodeling itself may present energy or metabolite requirement, or that the increase in blood flow and subsequent recovery of muscle function associated with vascular repair may lead to increased metabolic activity.

In contrast, I found the expression of several genes associated with inflammation tended to correlate with others known to inhibit angiogenesis. As examples, saline-treated ischemic tissues demonstrated strong upregulation of the pro-inflammatory genes TNF-α and CD44 [185, 186] as well as the anti-angiogenic genes interleukin 18 (Il18), arrestin (Arrb1), and the tissue inhibitor of metalloproteinase 2 (Timp2) [187–189] (among others). The mMSC-treated mice showed no such upregulation. These results are in line with a pilot transcriptome study of human patients with type-1 diabetes, in which a clear upregulation of TNF-α was observed in functionally impared endothelial progenitor cells [190]. These results highlight the importance of the tissue microenviroment in establishing the angiogenic response; inflamed tissue inhibits angiogenesis and slows recovery from vascular occlusion. Additional proteomics studies confirmed the up-regulation of the pro-angiogenic genes and relative down-regulation

of the pro-inflammatory genes in the stem cell-treated ischemic tissue.

DM causes changes in the endothelial microenviroment that can make a single biomarker therapy challenging to target PAD. Connective tissue growth factor expression (CTGF, an inhibitor of angiogenesis), cysteine-rich protein 61 (Cyr61), metallothionein 1 (Mt1) and 2 (Mt2), and CD68 (expressed on monocytes/macrophages), as examples, have been shown to be markedly increased in diabetic animals [191] (see Figure 5.6B). In general all animals showed enhanced expression of these genes, however the ischemic mMSC-treated tissues displayed a significant down regulation confirming, at the cellular level, the ability of mMSCs to alter the tissue microenvironment in complex ways. Intriguingly, the same set of genes was found to change after acute hindlimb ischemia within healthy mice in as soon as 6 hours and return to homeostasis between 7 to 14 days later, again in accordance with these results [192].

Other DM-associated genes that have been shown to increase the risk of thrombosis and vascular disease include Coagulation Factor III (F3) [193], which I found to be significanntly ($p = 0.05$) downregulated in the mMSC-treated group (see Figure 5.6B). Matrix metalloproteinase-2 (Mmp2), which is implicated in angiogenesis, was upregulated in mMSC group relative to saline animals, however other studies have found no change in its expression [194].

This study pieces together the changes that occur in diabetic mice after femoral artery ligation and theraputic intervention with mMSCs. All told, This study paints a compelling picture, in which mMSCs exert far-reaching effects, countering the anti-angiogenic effects of DM and inflamation, and enhancing themprocess of neovascularization and healing. More targeted experiments are needed to elucidate the biochemistry that underpin these responses, but this work represents an important step to widen the knowledge on multifaceted actions of mMSCs in the recovery of vascular complication associated with DM.

5.5 Conclusion

Angiogenic tissue microenviroment is tightly controlled by multifactorial processes involving both pro- and anti-angiogenic factors interacting with endothelial cells, smooth muscle cells, and the extracellular matrix (ECM). The signalling pathways are complex, with many details remaining unclear. To date, only a few studies have investigated the effects of diabetes on angiogenesis within the skeletal muscle, and most of them focused almost entirely on a single biomarker (VEGF-A) with ambiguous results [136, 195, 196].

Here I present findings that validate the potential for mMSCs to be used as a holistic therapy for diabetes-associated PAD. Rather than targeting a single facet of the body's response to ischemia, mMSCs appear to exert far reaching effects on the ischemic tissue microenvironment by enhancing angiogenesis, decreasing inflammation, and promoting muscle recovery. This work focuses on the response to treatment at both the cellular and tissue levels. To my knowledge this is the first study to utilize non-invasive targeted imaging strategies to measure angiogenesis and blood flow in ischemic diabetic limbs after muscle-derived mesenchymal stem cells therapy in combination with transcriptomics analysis. The translational nature of this work is difficult to overstate; not only I find that mMSC-based therapy can largely reverse vascular occlusion associated with PAD, but I also provide effective molecular imaging approaches that one day may be used to help diagnose vascular complications, as well as monitor their progression and treatment.

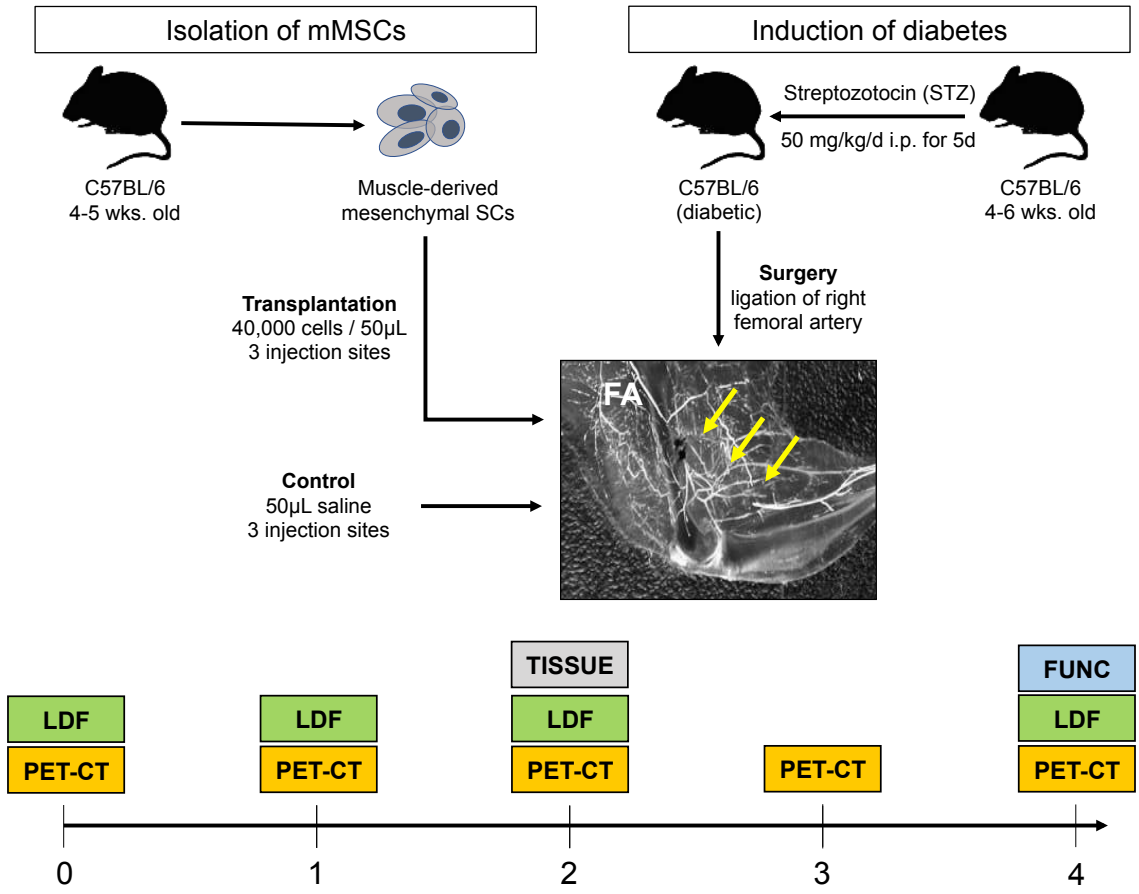

Figure 5.1: Study overview. Streptozotocin was used to induce DM in 4 to 6 week old C57BL/6 mice. The right femoral artery of the DM mice were then ligated to mimic PAD. mMSCs were isolated from another group of mice and then injected into three different sites in the ischemic gastrocnemius-soleus of DM group. A control group received saline injections. Both experimental and control groups were serially evaluated for $\alpha_V\beta_3$ expression (using PET-CT), blood perfusion (using laser Doppler flow, LDF), and muscle function (denoted FUNC). At week two, skeletal muscle tissue was extracted for immunohistochemistry and microarray transcriptomics experiments (denoted TISSUE).

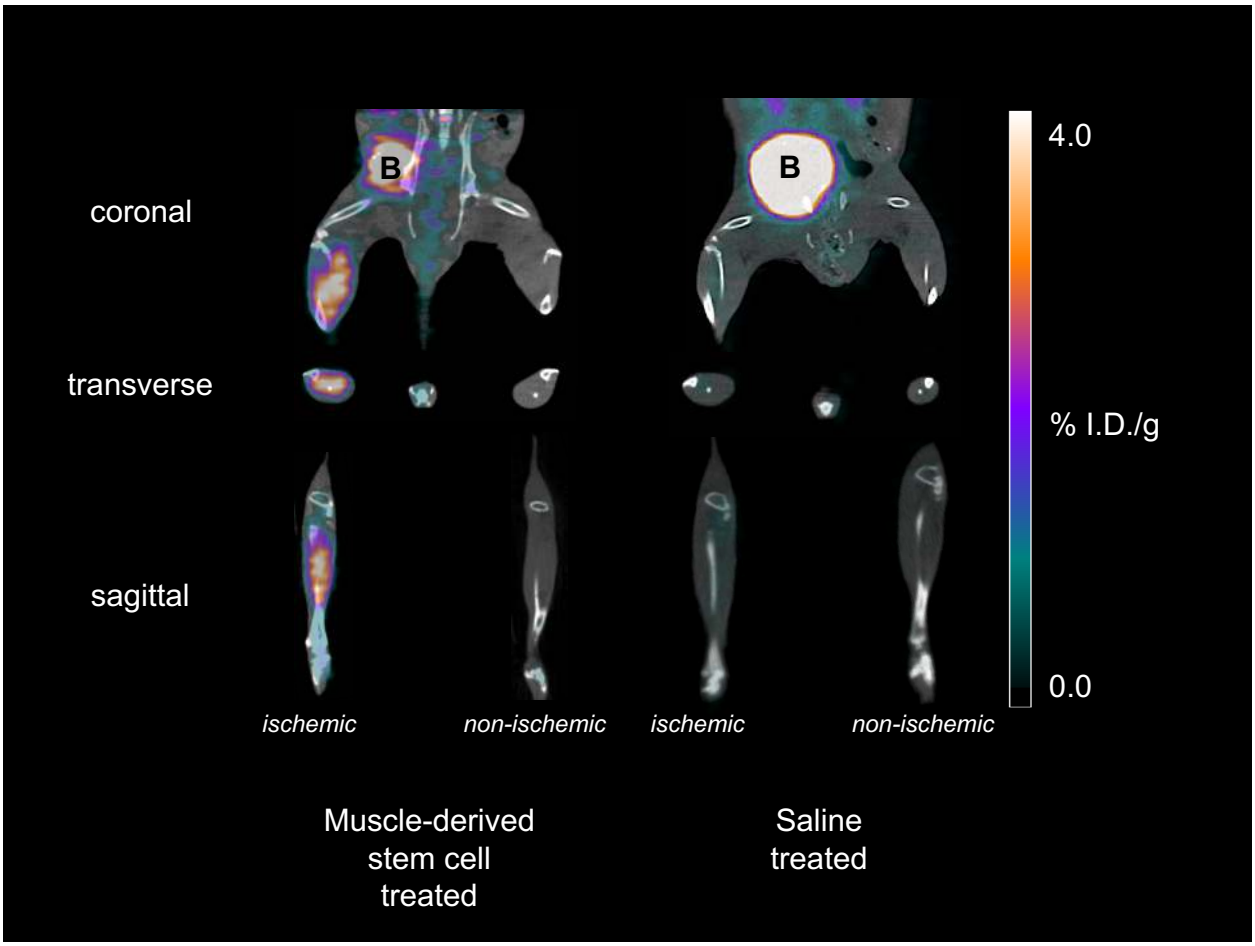

Figure 5.2: Representative PET-CT images. Coronal, transverse, and sagittal views are shown for both mMSC- and saline-treated mice at 1 week post surgery and implantation. The mMSC-treated mice show significant $\alpha_V\beta_3$-targeted probe accumulation in the ischemic limb.

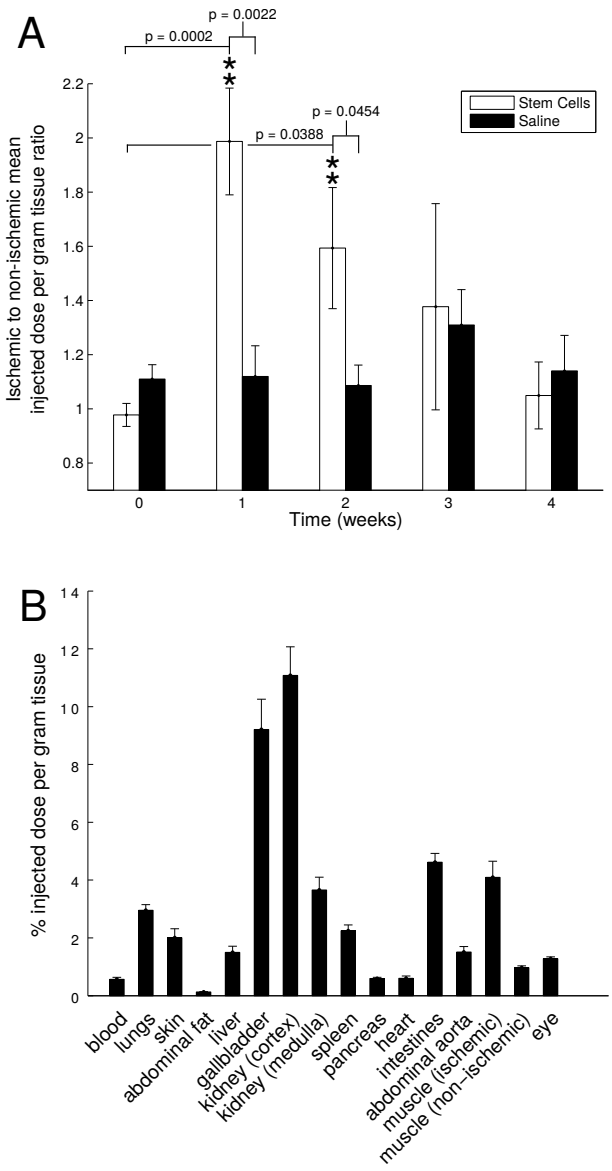

Figure 5.3: Image based analysis of $\alpha_V\beta_3$ expression and biodistribution. A) ^{64}Cu-NOTA-PEG$_4$-cRGD$_2$ was used to noninvasively assess $\alpha_V\beta_3$ expression before femoral artery ligation (week zero, baseline) and one, two, three, and four weeks after. mMSC-treated mice showed significant enhancement relative to both the baseline and the saline-treated group at the one and two week timepoints. B) The biodistribution assessed with gamma well counting of radiolabeled ^{64}Cu-NOTA-PEG$_4$-cRGD$_2$ targeted at $\alpha_V\beta_3$ integrin demonstrated a favorable biodistribution and optimal retention for targeted *in vivo* imaging of peripheral angiogenesis in n=4 animals treated with mMSCs.

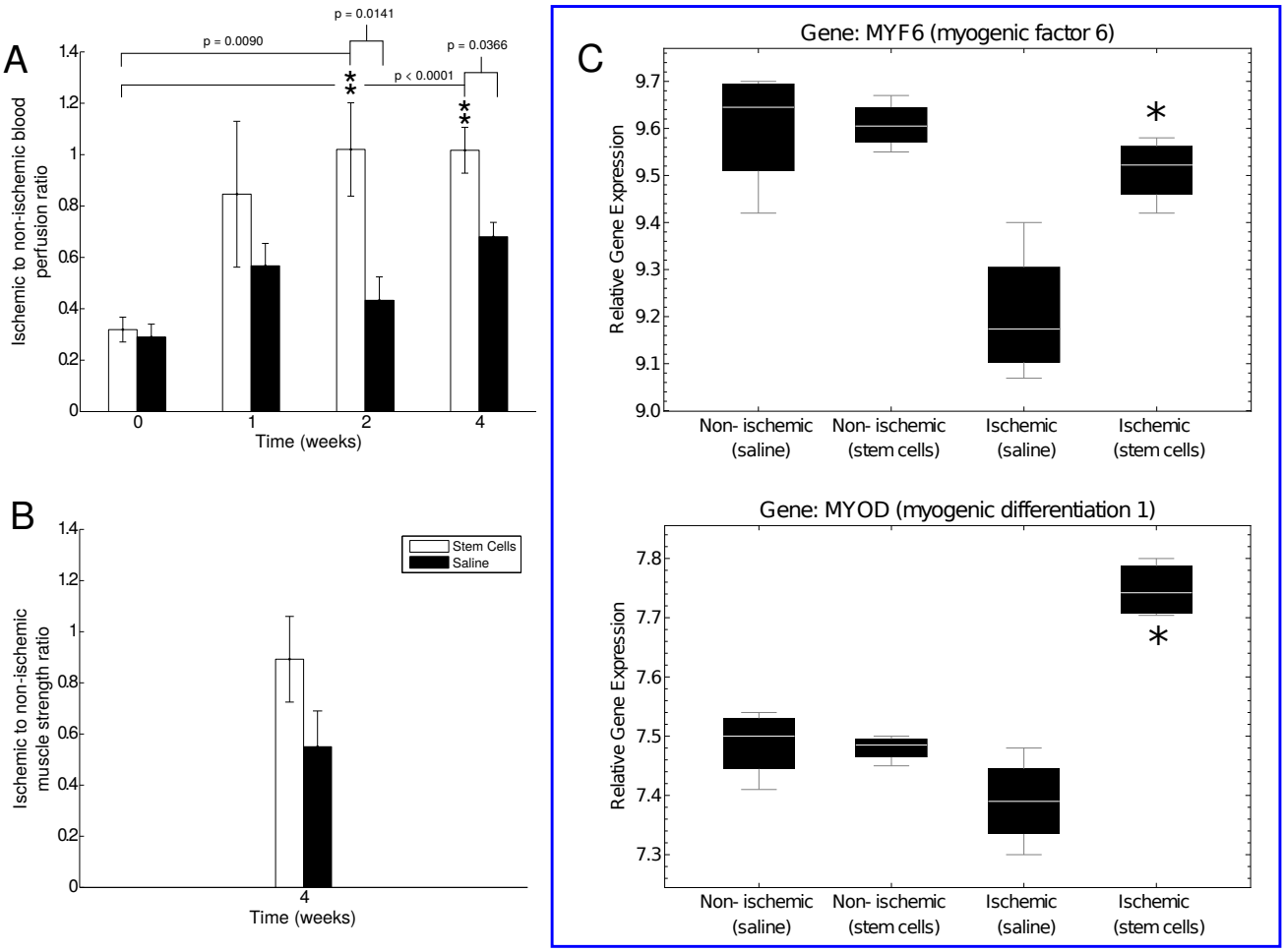

Figure 5.4: Analysis of blood perfusion, muscle strength, and muscle function related gene expression. A) Laser Doppler flow measurements were performed to assess blood perfusion in the ischemic and non-ischemic tissue of the mMSC- and saline-treated mice. Perfusion was significantly enhanced relative to baseline and saline-treated mice at the two and four week timepoints. B) Muscle function was assessed using an invasive technique at the four week timepoint. The mMSC-treated group showed a 1.7-fold increase over the saline-treated mice. C) Key muscle function genes determined by microarray n=4 for each group show a significant up-regulation in ischemic mMSCs treated mice in comparison to the saline and the non-ischemic skeletal muscle. The asterisks indicates a p value of < 0.01 comparing ischemic stem cell vs. ischemic saline treated mice.

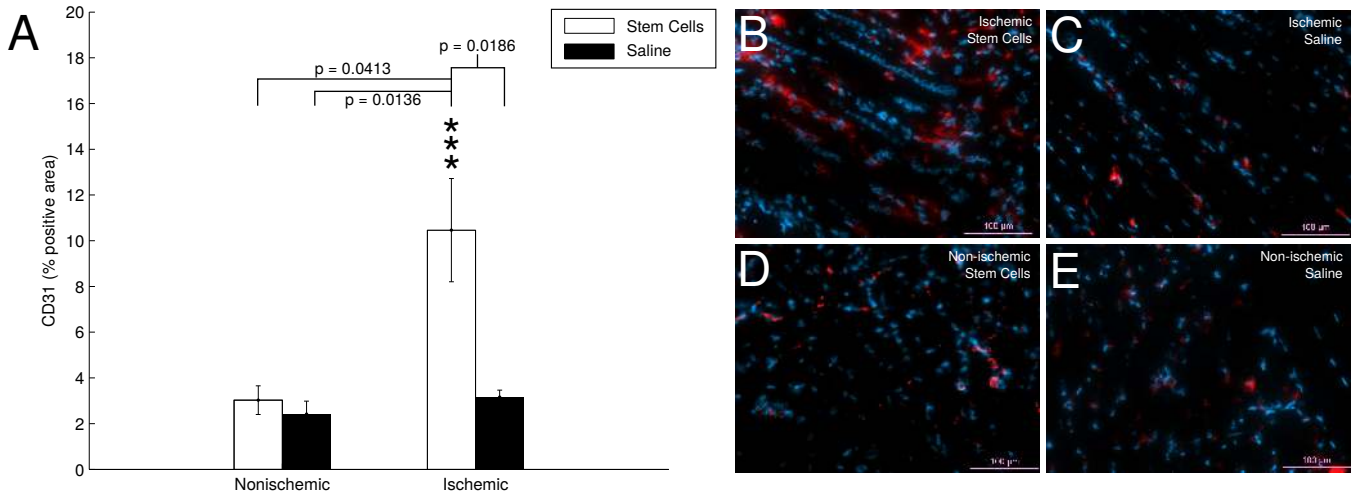

Figure 5.5: CD31 immunohistofluorescence. A) Quantification of CD31-positive area in stained skeletal muscle tissue. The mMSC-treated ischemic tissue showed significant enhancement relative to non-ischemic tissue, and saline-treated tissues. B-E) representative immunohistochemistry images with CD31 (red) and DAPI (blue).

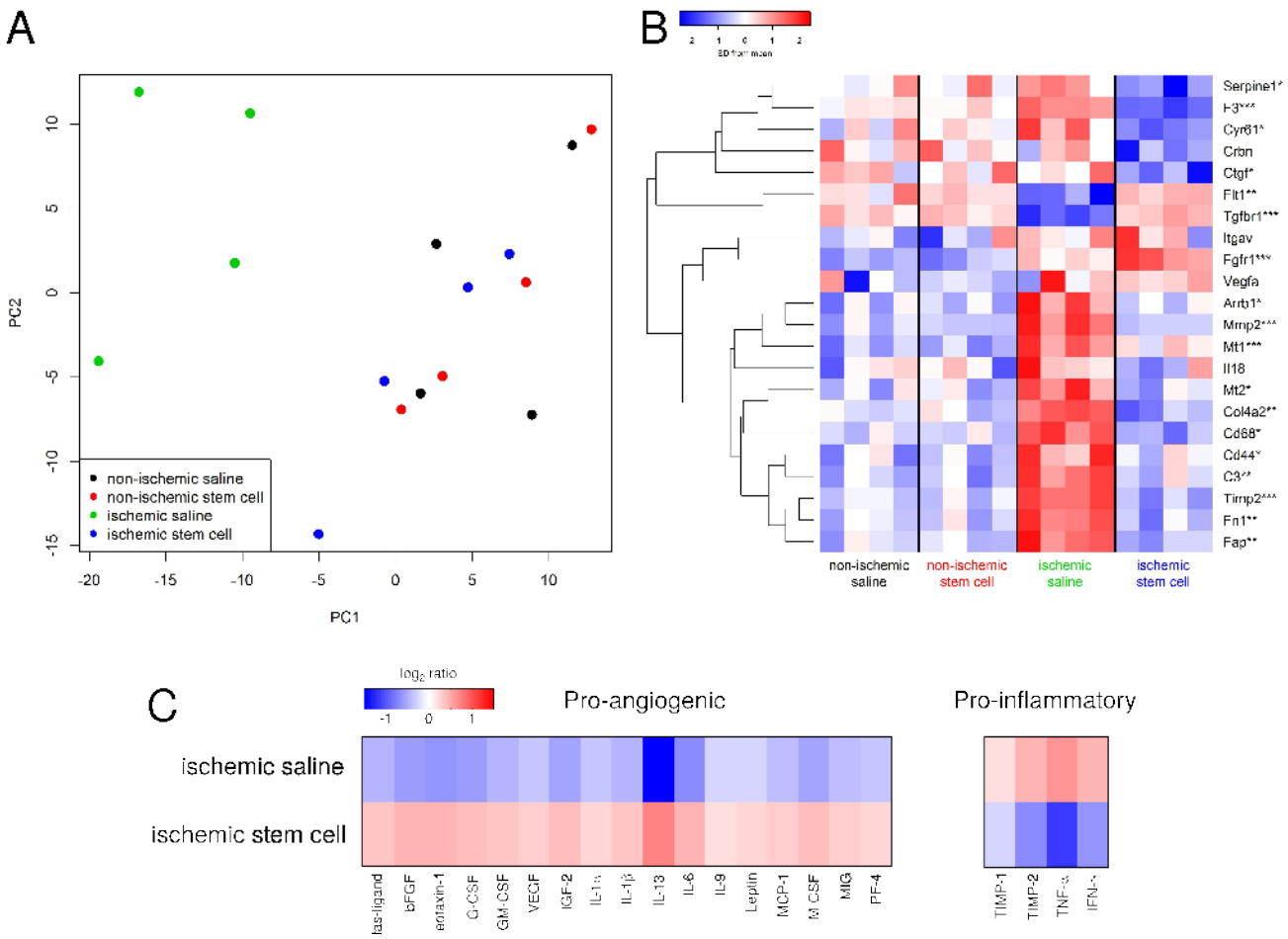

Figure 5.6: Analysis of transcriptomics and proteomics data. A) The gene expression states of excised tissues projected onto the first two principal components. The mMSC-treated ischemic tissue (blue) clusters with the non-ischemic tissues (red and black), indicating similar gene expression profiles, while the saline-treated ischemic samples cluster separately (green). B) Heatmap of the expression of several pro- and anti-angiogenic genes in the saline- and mMSC-treated mice (n=4 in each group). Asterisks indicate the smallest FDR p-value across the four comparisons (ischemic saline vs. non-ischemic saline, ischemic stem cell vs. non-ischemic stem cell, ischemic stem cell vs. ischemic saline, overall ANOVA)). * FDR p < 0.2, ** FDR $p < 0.1$, *** FDR $p < 0.05$. C) Heat map of cytokine expression (21 proteins) comparing mMSC- and saline-treated ischemic tissue. For each protein on the cytokine membrane, expression levels for both mMSC- and saline-treated tissues were averaged, and the $\log_2$ ratio of each value relative to its respective average is shown.

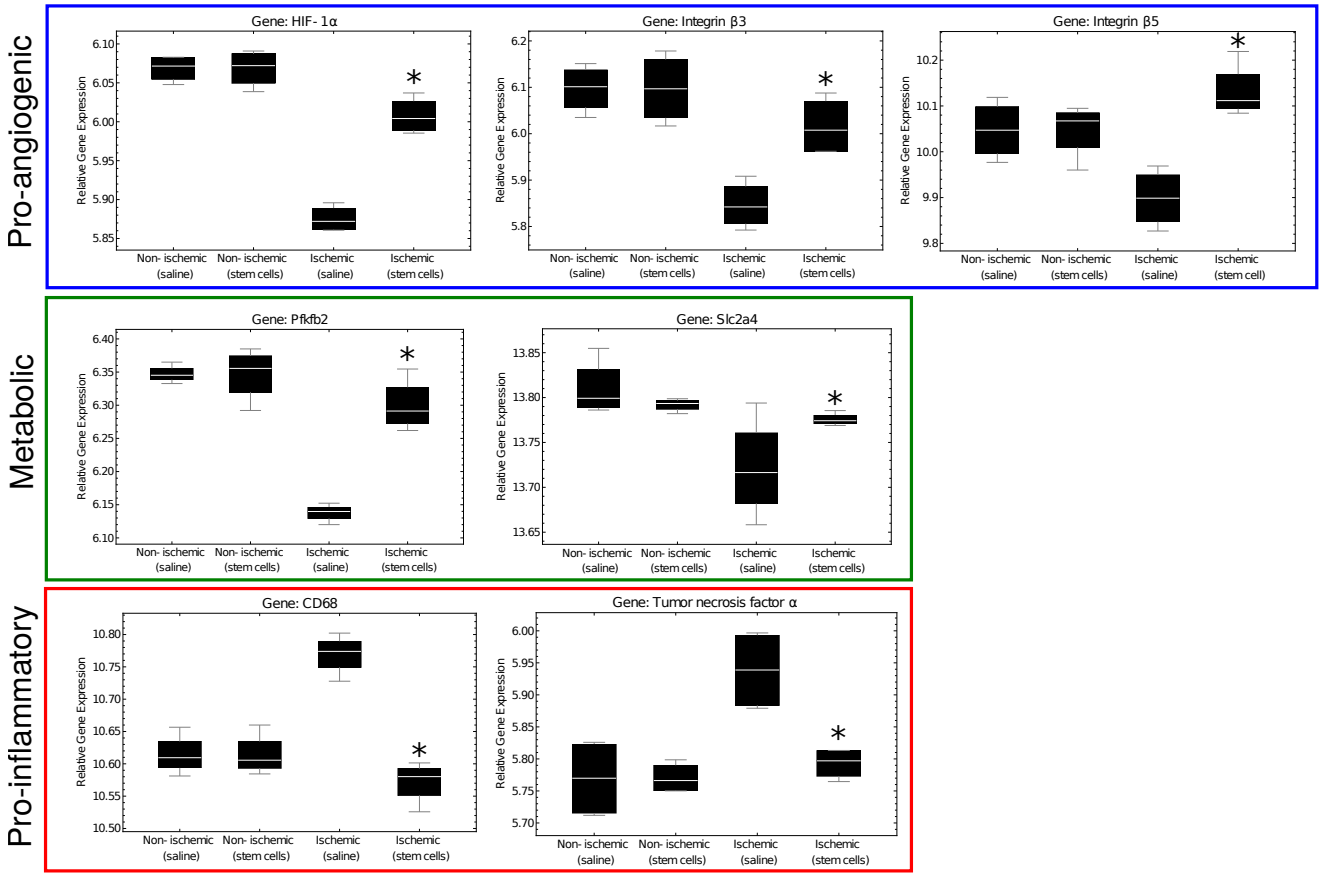

Figure 5.7: A representation of key regulatory genes. Pro-angiogenic and metabolic genes are significantly increased in mMSC-treated ischemic tissue, where pro-inflammatory genes are up-regulated in ischemic saline muscle tissue. There was no difference between the non-ischemic saline vs non-ischemic stem cell treated samples. The asterisks indicates a p value of < 0.05 comparing ischemic stem cell vs. ischemic saline treated mice.

Chapter 6

Conclusions

Throughout this document I have attempted to walk the reader through the development and application of a number of emerging imaging strategies designed to aid in the detection and treatment of peripheral vascular complications. We began with the development of two non-invasive molecular probes targeted at hypoxia and $\alpha_V\beta_3$—important molecular components involved in the angiogenic response. To investigate the physiological changes associated with PAD we employed a sensitive new ultrasound technology that allows us to detect slow-moving blood. This method is inexpensive, and can be performed using standard ultrasound machines, which could help doctors diagnose PAD earlier and treat the disease more effectively. After describing the imaging technologies we will use, our attention then shifted to developing an appropriate animal model of diabetes-associated PAD. By evaluating several markers associated with diabetes, we optimized an experimental protocols by which the manifestation of DM in the animal model resembles that of human DM patients.

To date, a number of agents have shown promise inducing angiogenesis and arteriogenesis in pre-clinical animal models of PAD, but none have proven successful in human randomized control trials. One possible reason for this difficulty in translation could revolve around the type of pre-clinical animal models used, and the functional outcomes being assessed. Currently available animal models for PAD vary considerably in both the strains of rodents used, and in the surgical procedures adopted in order to induce limb ischaemia. Moreover, the ways in which the effectiveness of a given treatment is measured varies from study to study, ranging from any one of a number of biomarkers (*e.g.* CD31, or VEGFR), to muscle function or grip strength tests.

In order to address these issues, I next pulled our imaging and animal model work together into an unprecedentedly complete multimodal study of tissue neovascularization following ischemia. This effort enables us to simultaneously track the dynamics of a number of molecular and physiological changes as the animals recover from vascular occlusion. The multimodal approach implemented in our study allows us to observe the immediate effects of ligation, with perfusion and oxygenation levels dropping substantially just minutes after the operation. From there, we note that in the deep tissue, the angiogenic response can take approximately three days or more to be fully elicited, beginning with a rapid rise in HIF-1α expression followed by a slower rise in $\alpha_V\beta_3$ expression. The effects of angiogenesis, *viv-a-vis* blood perfusion, do not manifest until approximately a week after ligation. We also find that the surface tissue undergoes a very different mode of recovery than does the deep tissue, beginning to reestablish normal blood perfusion within just two days, likely through arteriogenesis rather than angiogenesis.

Finally, I begin to move from detection and diagnostics to treatment by developing a stem cell-based therapy for PAD. I show that mMSCs mitigated several PAD-related complications by countering the anti-angiogenic effects of DM and inflammation, and enhancing the process of neovascularization and healing. This marks a milestone in the development of the next generation of translatable treatment options for people suffering from the disease.

Looking toward the future, much work remains before us. Most of it is translational; our multimodal imaging platform should be applied to large animals and eventually humans in order to study PAD in actual patients. Clinical translation should also be the goal for our stem cell work. While a number of additional experiments are needed to elucidate the biochemistry, location, and survival of our therapeutic mMSCs, the existing results are very promising, and I look forward to pursuing the approach in larger animals.

References

[1] Hedhli, J, Slania, SL, Płoska, A, Czerwinski, A, Konopka, CJ, Wozniak, M, Banach, M, Dobrucki, IT, Kalinowski, L, Dobrucki, LW (2018) Evaluation of a dimeric-crgd peptide for targeted pet-ct imaging of peripheral angiogenesis in diabetic mice. *Scientific reports* 8:5401.

[2] Hedhli, J, Konopka, CJ, Schuh, S, Bouvin, H, Cole, JA, Huntsman, HD, Kilian, KA, Dobrucki, IT, Boppart, MD, Dobrucki, LW (2017) Multimodal assessment of mesenchymal stem cell therapy for diabetic vascular complications. *Theranostics* 7:3876.

[3] Kim, M, Abbey, CK, Hedhli, J, Dobrucki, LW, Insana, MF (2017) Expanding acquisition and clutter filter dimensions for improved perfusion sensitivity. *IEEE Transactions on Ultrasonics, Ferroelectrics, and Frequency Control* 64:1429–1438.

[4] Knox, HJ, Hedhli, J, Kim, TW, Khalili, K, Dobrucki, LW, Chan, J (2017) A bioreducible n-oxide-based probe for photoacoustic imaging of hypoxia. *Nature Communications* 8:1794.

[5] Hedhli, J et al. (2017) Synthesis, chemical characterization and multiscale biological evaluation of a dimeric-cRGD peptide for targeted imaging of $\alpha v\beta 3$ integrin activity. *Scientific Reports* 7:3185.

[6] Cole, JA, Kohler, L, Hedhli, J, Luthey-Schulten, Z (2015) Spatially-resolved metabolic cooperativity within dense bacterial colonies. *BMC systems biology* 9:15.

[7] Lee, J, Abdeen, AA, Hedhli, J, Wycislo, KL, Dobrucki, IT, Fan, TM, Dobrucki, LW, Kilian, KA (2017) Melanoma topology reveals a stem-like phenotype that promotes angiogenesis. *Science advances* 3:e1701350.

[8] Huang, ES, Basu, A, O'grady, M, Capretta, JC (2009) Projecting the future diabetes population size and related costs for the us. *Diabetes care* 32:2225–2229.

[9] for Disease Control, C, Prevention et al. (2014) National diabetes statistics report: estimates of diabetes and its burden in the united states, 2014. *Atlanta, GA: US Department of Health and Human Services* 2014.

[10] Boon, B (2009) Leonardo da vinci on atherosclerosis and the function of the sinuses of valsalva. *Netherlands Heart Journal* 17:496–499.

[11] Aird, WC (2011) Discovery of the cardiovascular system: from galen to william harvey. *Journal of Thrombosis and Haemostasis* 9:118–129.

[12] Barold, SS (2003) Willem einthoven and the birth of clinical electrocardiography a hundred years ago. *Cardiac electrophysiology review* 7:99–104.

[13] Röntgen, WK (1928) (Press Cliche).

[14] Beck, CS, Pritchard, WH, Feil, HS (1947) Ventricular fibrillation of long duration abolished by electric shock. *Journal of the American Medical Association* 135:985–986.

[15] Aquilina, O (2006) A brief history of cardiac pacing. *Images in paediatric cardiology* 8:17.

[16] Cheatle, TR, Coleridge-Smith, PD, Scurr, JH (1991) The investigation of peripheral vascular disease-a historical perspective. *Vascular Medicine Review* pp 101–109.

[17] Ejrup, B (1948) Tonoscillography after exercise in peripheral vascular disease and coarctation of the aorta. *American Heart Journal* 35:41–57.

[18] KETY, SS (1948) Quantitative measurement of regional circulation by the clearance of radioactive sodium. *The American journal of the medical sciences* 215:352.

[19] dos Santos, R, Lamas, A, Caldas, JP et al. (1929) L'artériographie des membres de l'aorte et de ses branches abdominales. *Bull Mem Soc Natl Chir* 55:587.

[20] Satomura, S (1959) Study of the flow patterns in peripheral arteries by ultrasonics. *J. Acoust. Soc, Japan* 15:151–155.

[21] Baumann, K (2013) Growing a blood vessel network. *Nature Reviews Molecular Cell Biology* 14.

[22] Tennant, M, McGeachie, JK (1990) Blood vessel structure and function: a brief update on recent advances. *ANZ Journal of Surgery* 60:747–753.

[23] Otrock, ZK, Mahfouz, RA, Makarem, JA, Shamseddine, AI (2007) Understanding the biology of angiogenesis: review of the most important molecular mechanisms. *Blood Cells Mol Dis* 39:212–20.

[24] Carmeliet, P, Jain, RK (2000) Angiogenesis in cancer and other diseases. *Nature* 407:249.

[25] Folkman, J (1995) Angiogenesis in cancer, vascular, rheumatoid and other disease. *Nat Med* 1:27–31.

[26] Catrina, SB, Okamoto, K, Pereira, T, Brismar, K, Poellinger, L (2004) Hyperglycemia regulates hypoxia-inducible factor-1α protein stability and function. *Diabetes* 53:3226–3232.

[27] Osmundson, PJ, O'Fallon, WM, Clements, IP, Kazmier, FJ, Zimmerman, BR, Palumbo, P (1985) Reproducibility of noninvasive tests of peripheral occlusive arterial disease. *Journal of Vascular Surgery* 2:678–683.

[28] Joyce, W, Walsh, K, Gough, D, Gorey, T, Fitzpatrick, J (1990) Pulse oximetry: A new non-invasive assessment of peripheral arterial occlusive disease. *British Journal of Surgery* 77:1115–1117.

[29] Kasapis, C, Gurm, HS (2009) Current approach to the diagnosis and treatment of femoral-popliteal arterial disease. a systematic review. *Current cardiology reviews* 5:296–311.

[30] Balduf, LM, Langsfeld, M, Marek, JM, Tullis, MJ, Kasirajan, K, Matteson, B (2002) Complication rates of diagnostic angiography performed by vascular surgeons. *Vascular and endovascular surgery* 36:439–445.

[31] Lu, JT, Creager, MA (2004) The relationship of cigarette smoking to peripheral arterial disease. *Progress in Biochemistry and Biophysics* 31:189–193.

[32] Krishna, SM, Omer, SM, Golledge, J (2016) Evaluation of the clinical relevance and limitations of current pre-clinical models of peripheral artery disease. *Clinical Science* 130:127–150.

[33] Nath, B, Szabo, G (2012) Hypoxia and hypoxia inducible factors: diverse roles in liver diseases. *Hepatology* 55:622–633.

[34] Weitz, JI, Byrne, J, Clagett, GP, Farkouh, ME, Porter, JM, Sackett, DL, Strandness, DE, Taylor, LM (1996) Diagnosis and treatment of chronic arterial insufficiency of the lower extremities: a critical review. *Circulation* 94:3026–3049.

[35] Taylor, CT, Colgan, SP (2007) Hypoxia and gastrointestinal disease. *Journal of molecular medicine* 85:1295–1300.

[36] Brown, JM, Wilson, WR (2004) Exploiting tumour hypoxia in cancer treatment. *Nature Reviews Cancer* 4:437.

[37] Koch, CJ, Evans, SM (2015) Optimizing hypoxia detection and treatment strategies. *Seminars in nuclear medicine* (Elsevier), Vol. 45, pp 163–176.

[38] Sun, X, Niu, G, Chan, N, Shen, B, Chen, X (2011) Tumor hypoxia imaging. *Molecular Imaging and Biology* 13:399–410.

[39] Luker, GD, Luker, KE (2008) Optical imaging: current applications and future directions. *The Journal of Nuclear Medicine* 49:1.

[40] Fleming, IN, Manavaki, R, Blower, PJ, West, C, Williams, KJ, Harris, AL, Domarkas, J, Lord, S, Baldry, C, Gilbert, FJ (2015) Imaging tumour hypoxia with positron emission tomography. *British journal of cancer* 112:238.

[41] Filonov, GS, Krumholz, A, Xia, J, Yao, J, Wang, LV, Verkhusha, VV (2012) Deep-tissue photoacoustic tomography of a genetically encoded near-infrared fluorescent probe. *Angewandte Chemie International Edition* 51:1448–1451.

[42] Bell, AG (1880) Upon the production and reproduction of sound by light. *Journal of the Society of Telegraph Engineers* 9:404–426.

[43] Zackrisson, S, Van De Ven, S, Gambhir, S (2014) Light in and sound out: emerging translational strategies for photoacoustic imaging. *Cancer research* 74:979–1004.

[44] Hirayama, T, Okuda, K, Nagasawa, H (2013) A highly selective turn-on fluorescent probe for iron (ii) to visualize labile iron in living cells. *Chemical Science* 4:1250–1256.

[45] Ledoux, LAF, Brands, PJ, Hoeks, APG (1997) Reduction of the clutter component in Doppler ultrasound signals based on singular value decomposition: A simulation study. *Ultrasonic Imaging* 19:1 – 18.

[46] Mauldin, FW, Lin, D, Hossack, JA (2011) The singular value filter: A general filter design strategy for PCA-based signal separation in medical ultrasound imaging. *IEEE Transactions on Medical Imaging* 30:1951 – 1964.

[47] Demené, C et al. (2015) Spatiotemporal clutter filtering of ultrafast ultrasound data highly increases Doppler and fUltrasound sensitivity. *IEEE Trans Med Imag* 34:2271–2285.

[48] Cantisani, V et al. (2015) Growing indications for CEUS: The kidney, testis, lymph nodes, thyroid, prostate, and small bowel. *European Journal of Radiology* 84:1675 – 1684.

[49] Yang, W, Dempsey, P (2007) Diagnostic breast ultrasound: current status and future directions. *Radiol Clin North Am* 45:845–861.

[50] Oebisu, N, Hoshi, M, Ieguchi, M, Takada, J, Iwai, T, Ohsawa, M, Nakamura, H (2014) Contrast-enhanced color Doppler ultrasonography increases diagnostic accuracy for soft tissue tumors. *Oncol Rep* 32:1654–1660.

[51] Bjærum, S, Torp, H, Kristoffersen, K (2002) Clutter filter design for ultrasound color flow imaging. *IEEE Trans Ultrason Ferroelectr Freq Control* 49:204–216.

[52] Løvstakken, L, Bjærum, S, Kristoffersen, K, Haaverstad, R, Torp, H (2006) Real-time adaptive clutter rejection filtering in color flow imaging using power method iterations. *IEEE Trans Ultrason Ferroelectr Freq Control* 53:1597–1608.

[53] Yu, A, Løvstakken, L (2010) Eigen-based clutter filter design for ultrasound color flow imaging: a review. *IEEE Trans Ultrason Ferroelectr Freq Control* 57:1096–1111.

[54] Lathauwer, LD, Moor, BD, Vandewalle, J (2000) A multilinear singular value decomposition. *SIAM Journal on Matrix Analysis and Applications* 21:1253 – 1278.

[55] Bergqvist, G, Larsson, E (2010) The higher-order singular value decomposition: Theory and an application [lecture notes]. *IEEE Signal Processing Magazine* 27:151 – 154.

[56] Niiyama, H, Huang, N, Rollins, M, Cooke, J (2009) Murine model of hindlimb ischemia. *Journal of Visualized Experiments* 23.

[57] Vannieuwenhoven, N, Vandebril, R, Meerbergen, K (2012) A new truncation strategy for the higher-order singular value decomposition. *SIAM Journal on Scientific Computing* 34:A1027 – A1052.

[58] Hua, J, Dobrucki, L, Sadeghi, M, Zhang, J, Bourke, B, Cavaliere, P, Song, J, et al. (2005) Noninvasive imaging of angiogenesis with a ^{99m}Tc-labeled peptide targeted at $\alpha_v\beta_3$ integrin after murine hindlimb ischemia. *Circulation* 111:3255 – 3260.

[59] Bertoldi, D, de Sousa, PL, Fromes, Y, Wary, C, Carlier, P (2008) Quantitative, dynamic and noninvasive determination of skeletal muscle perfusion in mouse leg by NMR arterial spin-labeled imaging. *Magn Reson Imaging* 26:1259 – 1265.

[60] Dobrucki, LW, de Muinck, ED, Lindner, JR, Sinusas, AJ (2010) Approaches to multimodality imaging of angiogenesis. *J Nucl Med* 51 Suppl 1:66S–79S.

[61] Yamada, M (1997) Molecular interactions in cell adhesion complexes. *Curr Opin Cell Biol* 9:76–85.

[62] Shattil, SJ, Kim, C, Ginsberg, MH (2010) The final steps of integrin activation: the end game. *Nat Rev Mol Cell Biol* 11:288–300.

[63] Xiong, JP, Stehle, T, Diefenbach, B, Zhang, R, Dunker, R, Scott, DL, Joachimiak, A, Goodman, SL, Arnaout, MA (2001) Crystal structure of the extracellular segment of integrin αvβ3. *Science* 294:339–345.

[64] Niu, G, Chen, X (2011) Why integrin as a primary target for imaging and therapy. *Theranostics* 1:30–47.

[65] Goswami, M (2013) Importance of integrin receptors in the field of pharmaceutical and medical science. *Chemistry and Material Science* 3:224–252.

[66] Cai, W, Niu, G, Chen, X (2008) Imaging of integrins as biomarkers for tumor angiogenesis. *Curr Pharm Des* 14:2943–73.

[67] Zhang, Y, Yang, Y, Cai, W (2011) Multimodality imaging of integrin $\alpha_V\beta_3$ expression. *Theranostics* 1:135–148.

[68] Iagaru, A, Gambhir, SS (2013) Imaging tumor angiogenesis: the road to clinical utility. *AJR Am J Roentgenol* 201:W183–91.

[69] Liu, Z, Wang, F (2013) Development of rgd-based radiotracers for tumor imaging and therapy: translating from bench to bedside. *Curr Mol Med* 13:1487–505.

[70] Haubner, R, Decristoforo, C (2009) Radiolabelled rgd peptides and peptidomimetics for tumour targeting. *Front Biosci (Landmark Ed)* 14:872–86.

[71] Schottelius, M, Laufer, B, Kessler, H, Wester, HJ (2009) Ligands for mapping alphavbeta3-integrin expression in vivo. *Acc Chem Res* 42:969–80.

[72] Liu, S (2009) Radiolabeled cyclic rgd peptides as integrin alpha(v)beta(3)-targeted radiotracers: maximizing binding affinity via bivalency. *Bioconjug Chem* 20:2199–213.

[73] Zhou, Y, Chakraborty, S, Liu, S (2011) Radiolabeled cyclic rgd peptides as radiotracers for imaging tumors and thrombosis by spect. *Theranostics* 1:58–82.

[74] Danhier, F, Le Breton, A, Preat, V (2012) Rgd-based strategies to target alpha(v) beta(3) integrin in cancer therapy and diagnosis. *Mol Pharm* 9:2961–73.

[75] Tateishi, U, Oka, T, Inoue, T (2012) Radiolabeled rgd peptides as integrin alpha(v)beta3-targeted pet tracers. *Curr Med Chem* 19:3301–9.

[76] Cai, H, Conti, PS (2013) Rgd-based pet tracers for imaging receptor integrin alphav beta3 expression. *J Labelled Comp Radiopharm* 56:264–79.

[77] Haubner, R, Maschauer, S, Prante, O (2014) Pet radiopharmaceuticals for imaging integrin expression: tracers in clinical studies and recent developments. *Biomed Res Int* 2014:871609.

[78] Gaertner, FC, Kessler, H, Wester, HJ, Schwaiger, M, Beer, AJ (2012) Radiolabelled rgd peptides for imaging and therapy. *Eur J Nucl Med Mol Imaging* 39 Suppl 1:S126–38.

[79] Beer, AJ, Kessler, H, Wester, HJ, Schwaiger, M (2011) PET Imaging of Integrin $\alpha_V\beta_3$ Expression. *Theranostics* 1:48–57.

[80] Liu, S (2015) Radiolabeled cyclic rgd peptide bioconjugates as radiotracers targeting multiple integrins. *Bioconjug Chem* 26:1413–38.

[81] Gao, H, Lang, L, Guo, N, Cao, F, Quan, Q, Hu, S, Kiesewetter, DO, Niu, G, Chen, X (2012) Pet imaging of angiogenesis after myocardial infarction/reperfusion using a one-step labeled integrin-targeted tracer 18f-alf-nota-prgd2. *Eur J Nucl Med Mol Imaging* 39:683–92.

[82] Eo, JS, Paeng, JC, Lee, S, Lee, YS, Jeong, JM, Kang, KW, Chung, JK, Lee, DS (2013) Angiogenesis imaging in myocardial infarction using 68ga-nota-rgd pet: characterization and application to therapeutic efficacy monitoring in rats. *Coron Artery Dis* 24:303–11.

[83] Kiugel, M et al. (2014) Dimeric [(68)ga]dota-rgd peptide targeting alphavbeta 3 integrin reveals extracellular matrix alterations after myocardial infarction. *Mol Imaging Biol* 16:793–801.

[84] Reyes, E (2015) A novel pet tracer for targeted imaging of atherosclerosis. *J Nucl Cardiol* 22:1191–4.

[85] Mammen, M, Choi, SK, Whitesides, GM (1998) Polyvalent interactions in biological systems: Implications for design and use of multivalent ligands and inhibitors. *Angewandte Chemie* 37:2754–2794.

[86] Chen, X, Tohme, M, Park, R, Hou, Y, Bading, JR, Conti, PS (2004) Micro-pet imaging of alphav-beta3-integrin expression with 18f-labeled dimeric rgd peptide. *Mol Imaging* 3:96–104.

[87] Chen, X, Liu, S, Hou, Y, Tohme, M, Park, R, Bading, JR, Conti, PS (2004) Micropet imaging of breast cancer αv-integrin expression with 64cu-labeled dimeric rgd peptides. *Molecular Imaging & Biology* 6:350–359.

[88] Li, ZB, Cai, W, Cao, Q, Chen, K, Wu, Z, He, L, Chen, X (2007) (64)cu-labeled tetrameric and octameric rgd peptides for small-animal pet of tumor alpha(v)beta(3) integrin expression. *J Nucl Med* 48:1162–71.

[89] Li, ZB, Chen, K, Chen, X (2008) (68)Ga-labeled multimeric RGD peptides for micropet imaging of integrin $\alpha_V\beta_3$ expression. *Eur J Nucl Med Mol Imaging* 35:1100–8.

[90] Liu, S, Hsieh, WY, Jiang, Y, Kim, YS, Sreerama, SG, Chen, X (2007) Evaluation of a ^{99m}Tc-Labeled Cyclic RGD Tetramer for Noninvasive Imaging Integrin $\alpha_V\beta_3$-Positive Breast Cancer. *Bioconjug Chem* 18:438–446.

[91] Wang, L, Shi, J, Kim, YS, Zhai, S, Jia, B, Zhao, H, Liu, Z, Wang, F, Chen, X, Liu, S (2009) Improving tumor-targeting capability and pharmacokinetics of (99m)tc-labeled cyclic rgd dimers with peg(4) linkers. *Mol Pharm* 6:231–45.

[92] Shi, J, Kim, YS, Zhai, S, Liu, Z, Chen, X, Liu, S (2009) Improving tumor uptake and pharmacokinetics of (64)cu-labeled cyclic rgd peptide dimers with gly(3) and peg(4) linkers. *Bioconjug Chem* 20:750–9.

[93] Kubas, H, Schafer, M, Bauder-Wust, U, Eder, M, Oltmanns, D, Haberkorn, U, Mier, W, Eisenhut, M (2010) Multivalent cyclic rgd ligands: influence of linker lengths on receptor binding. *Nucl Med Biol* 37:885–91.

[94] Shi, J, Zhou, Y, Chakraborty, S, Kim, YS, Jia, B, Wang, F, Liu, S (2011) Evaluation of in-labeled cyclic rgd peptides: Effects of peptide and linker multiplicity on their tumor uptake, excretion kinetics and metabolic stability. *Theranostics* 1:322–40.

[95] Ji, S, Czerwinski, A, Zhou, Y, Shao, G, Valenzuela, F, Sowinski, P, Chauhan, S, Pennington, M, Liu, S (2013) (99m)tc-galacto-rgd2: a novel 99mtc-labeled cyclic rgd peptide dimer useful for tumor imaging. *Mol Pharm* 10:3304–14.

[96] Goodman, SL, Picard, M (2012) Integrins as therapeutic targets. *Trends Pharmacol Sci* 33:405–12.

[97] Ma, Q, Ji, B, Jia, B, Gao, S, Ji, T, Wang, X, Han, Z, Zhao, G (2011) Differential diagnosis of solitary pulmonary nodules using (9)(9)mtc-3p(4)-rgd(2) scintigraphy. *Eur J Nucl Med Mol Imaging* 38:2145–52.

[98] (2012) ^{99m}tc-3prgd$_2$ for integrin receptor imaging of lung cancer: a multicenter study. *J Nucl Med* 53:716–722.

[99] Miao, W, Zheng, S, Dai, H, Wang, F, Jin, X, Zhu, Z, Jia, B (2014) Comparison of 99mtc-3prgd2 integrin receptor imaging with 99mtc-mdp bone scan in diagnosis of bone metastasis in patients with lung cancer: a multicenter study. *PLoS One* 9:e111221.

[100] Liu, L et al. (2014) (99)mtc-3prgd2 scintimammography in palpable and nonpalpable breast lesions. *Mol Imaging* 13.

[101] Mittra, ES et al. (2011) Pilot pharmacokinetic and dosimetric studies of (18)f-fpprgd2: a pet radiopharmaceutical agent for imaging alpha(v)beta(3) integrin levels. *Radiology* 260:182–91.

[102] Iagaru, A, Mosci, C, Shen, B, Chin, FT, Mittra, E, Telli, ML, Gambhir, SS (2014) (18)F-FPPRGD2 PET/CT: pilot phase evaluation of breast cancer patients. *Radiology* 273:549–59.

[103] Minamimoto, R, Jamali, M, Barkhodari, A, Mosci, C, Mittra, E, Shen, B, Chin, F, Gambhir, SS, Iagaru, A (2015) Biodistribution of the (1)(8)f-fpprgd(2) pet radiopharmaceutical in cancer patients: an atlas of suv measurements. *Eur J Nucl Med Mol Imaging* 42:1850–8.

[104] Iagaru, A, Mosci, C, Mittra, E, Zaharchuk, G, Fischbein, N, Harsh, G, Li, G, Nagpal, S, Recht, L, Gambhir, SS (2015) Glioblastoma multiforme recurrence: An exploratory study of (18)f fpprgd2 pet/ct. *Radiology* 277:497–506.

[105] Withofs, N et al. (2015) 18f-fprgd2 pet/ct imaging of integrin alphavbeta3 in renal carcinomas: correlation with histopathology. *J Nucl Med* 56:361–4.

[106] Walsh, JC, Kolb, HC (2010) Applications of click chemistry in radiopharmaceutical development. *Chimia (Aarau)* 64:29–33.

[107] Haubner, R, Kuhnast, B, Mang, C, Weber, WA, Kessler, H, Wester, HJ, Schwaiger, M (2004) [18F]galacto-RGD: synthesis, radiolabeling, metabolic stability, and radiation dose estimates. *Bioconjug Chem* 15:61–9.

[108] Biacore, A (1997).

[109] Karlsson, R (1999) Affinity analysis of non-steady-state data obtained under mass transport limited conditions using biacore technology. *J Mol Recognit* 12:285–92.

[110] Murphy, M, Jason-Moller, L, Bruno, J (2006) Using biacore to measure the binding kinetics of an antibody-antigen interaction. *Curr Protoc Protein Sci* Chapter 19:Unit 19 14.

[111] Myszka, DG (1997) Kinetic analysis of macromolecular interactions using surface plasmon resonance biosensors. *Current opinion in biotechnology* 8:50–57.

[112] Karlsson, R (1999) Affinity analysis of non-steady-state data obtained under mass transport limited conditions using biacore technology. *J Mol Recognit* 12:285–292.

[113] Schindelin, J et al. (2012) Fiji: an open-source platform for biological-image analysis. *Nat Methods* 9:676–82.

[114] Dobrucki, LW, Tsutsumi, Y, Kalinowski, L, Dean, J, Gavin, M, Sen, S, Mendizabal, M, Sinusas, AJ, Aikawa, R (2010) Analysis of angiogenesis induced by local IGF-1 expression after myocardial infarction using microSPECT-CT imaging. *J Mol Cell Cardiol* 48:1071–1079.

[115] Chen, K, Ma, W, Li, G, Wang, J, Yang, W, Yap, LP, Hughes, LD, Park, R, Conti, PS (2012) Synthesis and evaluation of 64cu-labeled monomeric and dimeric ngr peptides for micropet imaging of cd13 receptor expression. *Molecular pharmaceutics* 10:417–427.

[116] Wu, Y, Zhang, X, Xiong, Z, Cheng, Z, Fisher, DR, Liu, S, Gambhir, SS, Chen, X (2005) micropet imaging of glioma integrin alphavbeta3 expression using (64)cu-labeled tetrameric rgd peptide. *J Nucl Med* 46:1707–18.

[117] Bentz, J et al. (2013) Variability in p-glycoprotein inhibitory potency (ic(5)(0)) using various in vitro experimental systems: implications for universal digoxin drug-drug interaction risk assessment decision criteria. *Drug Metab Dispos* 41:1347–66.

[118] Urbinati, C, Bugatti, A, Giacca, M, Schlaepfer, D, Presta, M, Rusnati, M (2005) αvβ3-integrin-dependent activation of focal adhesion kinase mediates nf-κb activation and motogenic activity by hiv-1 tat in endothelial cells. *Journal of cell science* 118:3949–3958.

[119] Haubner, R, Wester, HJ, Weber, WA, Mang, C, Ziegler, SI, Goodman, SL, Senekowitsch-Schmidtke, R, Kessler, H, Schwaiger, M (2001) Noninvasive imaging of alpha(v)beta3 integrin expression using 18f-labeled rgd-containing glycopeptide and positron emission tomography. *Cancer Res* 61:1781–5.

[120] Takagi, J, Petre, BM, Walz, T, Springer, TA (2002) Global conformational rearrangements in integrin extracellular domains in outside-in and inside-out signaling. *Cell* 110:599–11.

[121] Higuchi, T, Bengel, FM, Seidl, S, Watzlowik, P, Kessler, H, Hegenloh, R, Reder, S, Nekolla, SG, Wester, HJ, Schwaiger, M (2008) Assessment of alphavbeta3 integrin expression after myocardial infarction by positron emission tomography. *Cardiovasc Res* 78:395–403.

[122] Meoli, DF et al. (2004) Noninvasive imaging of myocardial angiogenesis following experimental myocardial infarction. *J Clin Invest* 113:1684–91.

[123] Hua, J et al. (2005) Noninvasive imaging of angiogenesis with a 99m-Tc-labeled peptide targeted at $\alpha_V\beta_3$ integrin after murine hindlimb ischemia. *Circulation* 111:3255–60.

[124] Dimastromatteo, J et al. (2010) In vivo molecular imaging of myocardial angiogenesis using the $\alpha v\beta 3$ integrin-targeted tracer ^{99m}tc-raft-rgd. *Journal of Nuclear Cardiology* 17:435–443.

[125] Laitinen, I et al. (2013) Comparison of cyclic rgd peptides for alphavbeta3 integrin detection in a rat model of myocardial infarction. *EJNMMI Res* 3:38.

[126] Garrison, JC, Rold, TL, Sieckman, GL, Figueroa, SD, Volkert, WA, Jurisson, SS, Hoffman, TJ (2007) In vivo evaluation and small-animal pet/ct of a prostate cancer mouse model using 64cu bombesin analogs: side-by-side comparison of the cb-te2a and dota chelation systems. *J Nucl Med* 48:1327–37.

[127] Dobrucki, LW, Tsutsumi, Y, Kalinowski, L, Dean, J, Gavin, M, Sen, S, Mendizabal, M, Sinusas, AJ, Aikawa, R (2010) Analysis of angiogenesis induced by local IGF-1 expression after myocardial infarction using microspect-ct imaging. *J Mol Cell Cardiol* 48:1071–9.

[128] Fam, NP, Verma, S, Kutryk, M, Stewart, DJ (2003) Clinician guide to angiogenesis. *Circulation* 108:2613–2618.

[129] Cai, W, Chen, X (2008) Multimodality molecular imaging of tumor angiogenesis. *Journal of Nuclear Medicine* 49:113S–128S.

[130] Chen, X, Plasencia, C, Hou, Y, Neamati, N (2005) Synthesis and biological evaluation of dimeric rgd peptide- paclitaxel conjugate as a model for integrin-targeted drug delivery. *Journal of medicinal chemistry* 48:1098–1106.

[131] Enis, DR, Shepherd, BR, Wang, Y, Qasim, A, Shanahan, CM, Weissberg, PL, Kashgarian, M, Pober, JS, Schechner, JS (2005) Induction, differentiation, and remodeling of blood vessels after transplantation of bcl-2-transduced endothelial cells. *Proceedings of the National Academy of Sciences of the United States of America* 102:425–430.

[132] Dobrucki, LW, Dione, DP, Kalinowski, L, Dione, D, Mendizabal, M, Yu, J, Papademetris, X, Sessa, WC, Sinusas, AJ (2009) Serial noninvasive targeted imaging of peripheral angiogenesis: validation and application of a semiautomated quantitative approach. *J Nucl Med* 50:1356–1363.

[133] Zernecke, A, Bernhagen, J, Weber, C (2008) Macrophage migration inhibitory factor in cardiovascular disease. *Circulation* 117:1594–1602.

[134] Beisswenger, PJ, Healy, JC, Shultz, EK (1993) Glycosylated serum proteins and glycosylated hemoglobin in the assessment of glycemic control in insulin-dependent and non-insulin-dependent diabetes mellitus. *Metabolism* 42:989–992.

[135] Rodriguez-Capote, K, Tovell, K, Holmes, D, Dayton, J, Higgins, TN (2015) Analytical evaluation of the diazyme glycated serum protein assay on the siemens advia 1800: comparison of results against hba1c for diagnosis and management of diabetes. *Journal of Diabetes Science and Technology* 9:192–199.

[136] Rivard, A, Silver, M, Chen, D, Kearney, M, Magner, M, Annex, B, Peters, K, Isner, JM (1999) Rescue of diabetes-related impairment of angiogenesis by intramuscular gene therapy with adeno-vegf. *The American journal of pathology* 154:355–363.

[137] Martin, A, Komada, MR, Sane, DC (2003) Abnormal angiogenesis in diabetes mellitus. *Medicinal Research Reviews* 23:117–145.

[138] Hu, S, Wang, LV (2010) Photoacoustic imaging and characterization of the microvasculature. *Journal of Biomedical Optics* 15:011101–011101.

[139] Ferrari, AU, Radaelli, A, Centola, M (2003) Invited review: aging and the cardiovascular system. *Journal of Applied Physiology* 95:2591–2597.

[140] Demircioglu, F, Hodivala-Dilke, K (2016) $\alpha v\beta 3$ integrin and tumour blood vessels—learning from the past to shape the future. *Current Opinion in Cell Biology* 42:121–127.

[141] Belch, JJ et al. (2003) Critical issues in peripheral arterial disease detection and management: a call to action. *Archives of Internal Medicine* 163:884–892.

[142] Shibuya, M (2011) Vascular endothelial growth factor VEGF and its receptor VEGFR signaling in angiogenesis: a crucial target for anti-and pro-angiogenic therapies. *Genes & Cancer* 2:1097–1105.

[143] Ferrara, N, Gerber, HP, LeCouter, J (2003) The biology of VEGF and its receptors. *Nature Medicine* 9:669–676.

[144] Fukumura, D, Jain, RK (2008) Imaging angiogenesis and the microenvironment. *Apmis* 116:695–715.

[145] Matsumoto, S, Yasui, H, Mitchell, JB, Krishna, MC (2010) Imaging cycling tumor hypoxia. *Cancer Research* 70:10019–10023.

[146] Cantisani, V et al. (2015) Growing indications for ceus: The kidney, testis, lymph nodes, thyroid, prostate, and small bowel. *European Journal of Radiology* 84:1675–1684.

[147] Lin, JB et al. (2015) Imaging of small animal peripheral artery disease models: recent advancements and translational potential. *International journal of molecular sciences* 16:11131–11177.

[148] Jayanthy, A, Sujatha, N, Reddy, MR, Narayanamoorthy, V (2014) Non invasive blood flow assessment in diabetic foot ulcer using laser speckle contrast imaging technique. *Biomedical Applications of Light Scattering VIII* (International Society for Optics and Photonics), Vol. 8952, p 89521D.

[149] Villanueva, FS, Wagner, WR (2008) Ultrasound molecular imaging of cardiovascular disease. *Nature Clinical Practice Cardiovascular Medicine* 5:S26–S32.

[150] McDonald, DM, Choyke, PL (2003) Imaging of angiogenesis: from microscope to clinic. *Nature Medicine* 9:713–725.

[151] Cao, F, Qiu, Z, Li, H, Lai, P (2017) Photoacoustic imaging in oxygen detection. *Applied Sciences* 7:1262.

[152] Prahl, S (1999) Tabulated molar extinction coefficient for hemoglobin in water. *Wellman Laboratories, Harvard Medical School, Boston* 5.

[153] Manders, E, Verbeek, F, Aten, J (1993) Measurement of co-localization of objects in dual-colour confocal images. *Journal of Microscopy* 169:375–382.

[154] Yang, Y, Tang, G, Yan, J, Park, B, Hoffman, A, Tie, G, Wang, R, Messina, LM (2008) Cellular and molecular mechanism regulating blood flow recovery in acute versus gradual femoral artery occlusion are distinct in the mouse. *Journal of Vascular Surgery* 48:1546–1558.

[155] Abdulhannan, P, Russell, D, Homer-Vanniasinkam, S (2012) Peripheral arterial disease: a literature review. *British Medical Bulletin* 104.

[156] Hopkins, SP, Bulgrin, JP, Sims, RL, Bowman, B, Donovan, DL, Schmidt, SP (1998) Controlled delivery of vascular endothelial growth factor promotes neovascularization and maintains limb function in a rabbit model of ischemia. *Journal of Vascular Surgery* 27:886–895.

[157] Cleeter, M, Cooper, J, Darley-Usmar, V, Moncada, S, , Schapira, A (1994) Reversible inhibition of cytochrome c oxidase, the terminal enzyme of the mitochondrial respiratory chain, by nitric oxide: implications for neurodegenerative diseases. *FEBS Letters* 345:50–54.

[158] Ho, TK, Rajkumar, V, Ponticos, M, Leoni, P, Black, DCM, Abraham, DJ, Baker, DM (2006) Increased endogenous angiogenic response and hypoxia-inducible factor-1α in human critical limb ischemia. *Journal of Vascular Surgery* 43:125–133.

[159] Shen, W, Xu, X, Ochoa, M, Zhao, G, Bernstein, R, Forfia, P, Hintze, T (2000) Endogenous nitric oxide in the control of skeletal muscle oxygen extraction during exercise. *Acta Physiologica* 168:675–686.

[160] Huang, AL et al. (2007) Predictive value of reactive hyperemia for cardiovascular events in patients with peripheral arterial disease undergoing vascular surgery. *Arteriosclerosis, Thrombosis, and Vascular Biology* 27:2113–2119.

[161] Loscalzo, J, Vita, JA (1994) Ischemia, hyperemia, exercise, and nitric oxide. *Circulation* 90:2556–2559.

[162] Heil, M, Schaper, W (2007) Insights into pathways of arteriogenesis. *Current Pharmaceutical Biotechnology* 8:35–42.

[163] Van Royen, N, Piek, JJ, Buschmann, I, Hoefer, I, Voskuil, M, Schaper, W (2001) Stimulation of arteriogenesis; a new concept for the treatment of arterial occlusive disease. *Cardiovascular Research* 49:543–553.

[164] Maslov, K, Zhang, HF, Hu, S, Wang, LV (2008) Optical-resolution photoacoustic microscopy for in vivo imaging of single capillaries. *Optics Letters* 33:929–931.

[165] Wilson, JR, Mancini, DM, McCully, K, Ferraro, N, Lanoce, V, Chance, B (1989) Noninvasive detection of skeletal muscle underperfusion with near-infrared spectroscopy in patients with heart failure. *Circulation* 80:1668–1674.

[166] Walton, HL, Corjay, MH, Mohamed, SN, Mousa, SA, Santomenna, LD, Reilly, TM (2000) Hypoxia induces differential expression of the integrin receptors αvβ3 and αvβ5 in cultured human endothelial cells. *Journal of Cellular Biochemistry* 78:674–680.

[167] Simons, M et al. (2000) Clinical trials in coronary angiogenesis: issues, problems, consensus. *Circulation* 102:e73–e86.

[168] Sneider, EB, Nowicki, PT, Messina, LM (2009) Regenerative medicine in the treatment of peripheral arterial disease. *Journal of cellular biochemistry* 108:753–761.

[169] Raval, Z, Losordo, DW (2013) Cell therapy of peripheral arterial disease. *Circulation research* 112:1288–1302.

[170] Burlacu, A (2013) Tracking the mesenchymal stem cell fate after transplantation into the infarcted myocardium. *Current stem cell research & therapy* 8:284–291.

[171] Huntsman, HD, Zachwieja, N, Zou, K, Ripchik, P, Valero, MC, De Lisio, M, Boppart, MD (2013) Mesenchymal stem cells contribute to vascular growth in skeletal muscle in response to eccentric exercise. *American Journal of Physiology-Heart and Circulatory Physiology* 304:H72–H81.

[172] Tahergorabi, Z, Khazaei, M (2012) Imbalance of angiogenesis in diabetic complications: the mechanisms. *International journal of preventive medicine* 3:827.

[173] Clark, AD, Youd, JM, Rattigan, S, Barrett, EJ, Clark, MG (2001) Heterogeneity of laser doppler flowmetry in perfused muscle indicative of nutritive and nonnutritive flow. *American Journal of Physiology-Heart and Circulatory Physiology* 280:H1324–H1333.

[174] Lueders, TN, Zou, K, Huntsman, HD, Meador, B, Mahmassani, Z, Abel, M, Valero, MC, Huey, KA, Boppart, MD (2011) The α7β1-integrin accelerates fiber hypertrophy and myogenesis following a single bout of eccentric exercise. *American Journal of Physiology-Cell Physiology* 301:C938–C946.

[175] Denwood, MJ (2016) runjags: An r package providing interface utilities, model templates, parallel computing methods and additional distributions for mcmc models in jags. *Journal of Statistical Software* 71:1–25.

[176] Ritchie, ME, Phipson, B, Wu, D, Hu, Y, Law, CW, Shi, W, Smyth, GK (2015) limma powers differential expression analyses for rna-sequencing and microarray studies. *Nucleic acids research* p gkv007.

[177] Smyth, GK, Speed, T (2003) Normalization of cdna microarray data. *Methods* 31:265–273.

[178] Phipson, B, Lee, S, Majewski, IJ, Alexander, WS, Smyth, GK et al. (2016) Robust hyperparameter estimation protects against hypervariable genes and improves power to detect differential expression. *The Annals of Applied Statistics* 10:946–963.

[179] Huber, W et al. (2015) Orchestrating high-throughput genomic analysis with bioconductor. *Nature methods* 12:115–121.

[180] Bosch-Marce, M et al. (2007) Effects of aging and hypoxia-inducible factor-1 activity on angiogenic cell mobilization and recovery of perfusion after limb ischemia. *Circulation research* 101:1310–1318.

[181] Cornelison, D, Wold, BJ (1997) Single-cell analysis of regulatory gene expression in quiescent and activated mouse skeletal muscle satellite cells. *Developmental biology* 191:270–283.

[182] von Degenfeld, G, Banfi, A, Springer, ML, Wagner, RA, Jacobi, J, Ozawa, CR, Merchant, MJ, Cooke, JP, Blau, HM (2006) Microenvironmental vegf distribution is critical for stable and functional vessel growth in ischemia. *The FASEB journal* 20:2657–2659.

[183] Bissell, MJ, Hines, WC (2011) Why don't we get more cancer? a proposed role of the microenvironment in restraining cancer progression. *Nature medicine* 17:320–329.

[184] Dehne, N, Brüne, B (2009) Hif-1 in the inflammatory microenvironment. *Experimental cell research* 315:1791–1797.

[185] Tandle, A, Blazer, DG, Libutti, SK (2004) Antiangiogenic gene therapy of cancer: recent developments. *Journal of translational medicine* 2:22.

[186] Harrison, C (2012) Obesity and diabetes: Cd44 immune receptor linked to diabetes. *Nature Reviews Drug Discovery* 11:442–442.

[187] Fan, TPD, Jagger, R, Bicknell, R (1995) Controlling the vasculature: angiogenesis, anti-angiogenesis and vascular targeting of gene therapy. *Trends in pharmacological sciences* 16:57–66.

[188] D'Amato, RJ, Loughnan, MS, Flynn, E, Folkman, J (1994) Thalidomide is an inhibitor of angiogenesis. *Proceedings of the National Academy of Sciences* 91:4082–4085.

[189] Malecki, M, Kolsut, P, Proczka, R (2005) Angiogenic and antiangiogenic gene therapy. *Gene therapy* 12:S159–S169.

[190] van Oostrom, O, de Kleijn, DP, Fledderus, JO, Pescatori, M, Stubbs, A, Tuinenburg, A, Lim, SK, Verhaar, MC (2009) Folic acid supplementation normalizes the endothelial progenitor cell transcriptome of patients with type 1 diabetes: a case-control pilot study. *Cardiovascular diabetology* 8:47.

[191] Kivelä, R, Silvennoinen, M, Touvra, AM, Lehti, TM, Kainulainen, H, Vihko, V (2006) Effects of experimental type 1 diabetes and exercise training on angiogenic gene expression and capillarization in skeletal muscle. *The FASEB journal* 20:1570–1572.

[192] Lee, CW, Stabile, E, Kinnaird, T, Shou, M, Devaney, JM, Epstein, SE, Burnett, MS (2004) Temporal patterns of gene expression after acute hindlimb ischemia in mice: insights into the genomic program for collateral vessel development. *Journal of the American College of Cardiology* 43:474–482.

[193] Babić, N, Dervisević, A, Huskić, J, Musić, M (2011) Coagulation factor viii activity in diabetic patients. *Medicinski glasnik: official publication of the Medical Association of Zenica-Doboj Canton, Bosnia and Herzegovina* 8:134–139.

[194] Uemura, S, Matsushita, H, Li, W, Glassford, AJ, Asagami, T, Lee, KH, Harrison, DG, Tsao, PS (2001) Diabetes mellitus enhances vascular matrix metalloproteinase activity. *Circulation Research* 88:1291–1298.

[195] Sasso, FC et al. (2005) Increased vascular endothelial growth factor expression but impaired vascular endothelial growth factor receptor signaling in the myocardium of type 2 diabetic patients with chronic coronary heart disease. *Journal of the American College of Cardiology* 46:827–834.

[196] Chou, E et al. (2002) Decreased cardiac expression of vascular endothelial growth factor and its receptors in insulin-resistant and diabetic states. *Circulation* 105:373–379.